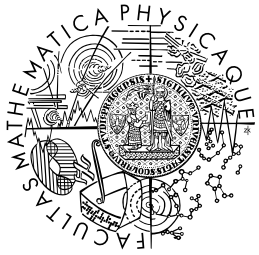

FACULTY
OF MATHEMATICS
AND PHYSICS
Charles University

DOCTORAL THESIS

Klára Bogár,
née Mitošinková

Additional plasma heating of tokamak plasma by powerful beam of deuterium atoms on the COMPASS tokamak

Department of Surface and Plasma Physics

Supervisor of the doctoral thesis:	RNDr. Jan Stöckel, CSc.
Study programme:	Physics
Study branch:	Physics of Plasmas and Ionized Media

Prague 2021

I declare that I carried out this doctoral thesis independently, and only with the cited sources, literature and other professional sources.

I understand that my work relates to the rights and obligations under the Act No. 121/2000 Sb., the Copyright Act, as amended, in particular the fact that the Charles University has the right to conclude a license agreement on the use of this work as a school work pursuant to Section 60 subsection 1 of the Copyright Act.

In Prague date 1^{st} July 2021 signature of the author

Here I would like express my gratitude to Jan Stockel, my supervisor and friend. He was trying not only to give me a knowledge about the fusion itself, but he also introduced me into the community and he showed me beauties of the scientific lifestyle.

Despite I had only one official supervisor, I would like to thank also to Jozef Varju, who guided me since my bachelor thesis up to now. He patiently taught me how to operate NBIs, he discussed particular problems and preliminary results with me, when I became stuck in my work or simply hugged me, when I needed it.

As the fusion research cannot be done alone and it is each time a work of the team, I would like to thank to all current and former COMPASS team members for their help, advice and friendly working environment. Namely, I would like to thank to Josef Havlicek, who arranged the basic NBI experiments campaign and he spent few evenings with me in the control room to realize significant part of the discharges, which became a base of this thesis.

Special thanks go to Benedikt Geiger and Philip A. Schneider, who warmly accepted me into their group during my internship at the ASDEX Upgrade tokamak.

In the end I would like to thank to my parents, my sister and my husband for their endless support and encouragement.

Title: Additional plasma heating of tokamak plasma by powerful beam of deuterium atoms on the COMPASS tokamak

Author: Klára Bogár, née Mitošinková

Department: Department of Surface and Plasma Physics

Supervisor: RNDr. Jan Stöckel, CSc., Institute of Plasma Physics of the Czech Academy of Sciences

Abstract: Two neutral beam injectors (NBIs) were installed on the COMPASS tokamak as a main upgrade after its move from the UK to Prague. The thesis deals with general experimental specifications of additionally heated plasmas by the NBI under the wide range of conditions on the COMPASS tokamak.

The geometrical parameters of the beams are determined from the spectroscopic measurements. Consequently, the NBI power passing through the narrow duct connecting NBI and tokamak chamber is investigated. The passing fraction of the NBI power is confirmed by the power balance analysis, which provides information about the delivered power into the plasma based on the plasma parameters.

Once the delivered power is well known a description of beams interaction with plasma via global parameters such as the plasma temperatures, the plasma density, the energy confinement time and neutron yield is given. It is shown, that the NBIs heat mostly ions, which can reach $\sim 1\,\mathrm{keV}$ in the plasma core.

Moreover, the impact of the fast ions presence on the commonly observed MHD activities, the sawtooth instability and the edge localized modes (ELMs), is discussed and compared with results from other tokamaks. The sawtooth period is prolonged by the influence of the NBI from 2 ms up to 4.5 ms. The knowledge of the NBI passing power into the tokamak chamber allows to determine the normed power through the separatrix, which is a key parameter for the ELMs classification.

Keywords: fusion, tokamak, neutral beam injection, power balance, neutral particle analyzer

Název: Dodatečný ohřev plazmatu výkonovým svazkem atomů deuteria na tokamaku COMPASS

Autor: Klára Bogár, roz. Mitošinková

Katedra: Katedra fyziky povrchů a plazmatu

Vedoucí: RNDr. Jan Stöckel, CSc., Ústav fyziky plazmatu Akademie věd České republiky v.v.i.

Abstract: Dva injektory svazku energetických atomů byly instalovány na tokamaku COMPASS po jeho přesunu na Ústav fyziky plazmatu v.v.i. AV ČR z Velké Británie. Tato práce se zabývá základní charakteristikou vlivu dodatečného ohřevu svazky vysokoenergetických neutrálních atomů na parametry plazmatu během experimentů na tokamaku COMPASS. Geometrické parametry svazků jsou měřeny spektroskopicky a slouží jako vstupní informace pro výpočet skutečného výkonu svazku, který prochází úzkým portem mezi svazkem a vakuouvou komorou tokamaku. Tyto výpočty jsou potvrzeny výkonovou bilancí, která je založena na měřených parametrech plazmatu.

Se znalostí skutečného dodávaného příkonu svazků je možné zkoumat vliv svazků na globální parametry plazmatu, jako je iontová a elektronová teplota, hustota, doba udržení energie a množství produkovaných neutronů. Měření ukazují, že svazky ohřívají převážně ionty, které mohou dosáhnout teploty $\sim 1\,\mathrm{keV}$.

Kromě toho je ukázán i vliv přítomnosti rychlých iontů na nejběžnější MHD nestability v plazmatu, konkrétně pilové nestability (tzv. sawtooth instability) a okrajové módy (tzv. edge localized modes, ELMs). Tento vliv je porovnán s výsledky z jiných tokamaků. Perioda pilové nestability je vlivem svazku prodloužena z 2 ms na 4.5 ms. Díky znalosti skutečného dodávaného příkonu svazků do plazmatu je možné určit normovaný výkon překračující hranici udrženého plazmatu, který je základním parametrem pro klasifikaci typů okrajových módů.

Klíčová slova: fúze, tokamak, injekce neutrálního svazku, výkonová bilance, analyzátor neutrálních částic

Contents

Introduction

The tokamak is a promising concept of the future fusion power plant. The rate of the fusion reactions in the tokamak is sufficient if the tokamak fuel is on the high temperatures, around tens of keV in case of the fusion reaction of deuterium and tritium nucleus. To reach such temperatures the fuel has to be in the plasma form. The plasma heating is secured by a current driven in the plasma. However, the ohmic heating efficiency degradates as the plasma temperature increases. Therefore the additional heating systems are needed.

Neutral beam injector (NBI) is one of the options for an additional plasma heating. NBI produces fast neutrals, which propagate freely across the tokamak magnetic field into a plasma. Injected neutral beam particles collide with the plasma particles and the collisions results into formation of the fast ions, which are trapped by the tokamak magnetic field. As the fast ions are well confined, they transfer their energy to the plasma particles via Coulomb collisions.

Two identical injectors have been installed on the COMPASS tokamak as an upgrade after the COMPASS tokamak relocation on the IPP CAS. As the COMPASS tokamak had never been operated with the neutral beam injection before, the request for the basic NBI-plasma interaction specification arised.

The main purpose of the work presented in this thesis is to study parameters of the NBI system itself and its impact on the COMPASS plasmas. The thesis is structured as follows. Chapter 1 gives an introduction into the fusion research in respect to the additional plasma heating. It is followed by a general overview of the possible additional heating systems for the tokamaks and it includes a more specific description of the neutral beam attenuation in the plasma and the neutral beam formation in chapter 2. A description of the NBI fast ions interaction with bulk plasma particles is discussed in chapter 3. Chapter 4 describes the COMPASS tokamak, its NBI systems including their measured characteristics and the COMPASS diagnostics used for this work.

Remaining chapters are dedicated to the experimental results based on the measurements realized on the COMPASS tokamak. Chapter 5 introduces experimental campaigns dedicated for the NBI characterization. The impacts of the neutral beam injection on the global plasma parameters such as the delivered additional power registered by the plasma diagnostics, the energy confinement time, the plasma density and temperatures and the neutron yield, are shown in the chapter 6. Chapter 7 discusses how the neutral beams affect two common MHD instabilities, the sawtooth instability and the edge localized modes. The last chapter 8 includes short discussion about the role of background neutrals in respect to the neutral beam injection heating efficiency. It focuses on the work dedicated to the development of the new method to determine the background neutral density profiles from the neutral particle analyzers data. The work presented in the chapter 8 is based on the data measured on the ASDEX Upgrade tokamak, located in the Max-Planck-Institut für Plasmaphysik, Garching DE.

In the conclusion, the particular observations are summed up and the most important results are stressed.

1. Tokamaks

As the world energy consumption is increasing each year [1], the time and location independent sources of power are an urgent necessity. These requirements can be fulfilled by the power plants based on the fusion reaction. The easiest fusion reaction to initiate is a fusion of two different hydrogen isotopes, deuterium (D) and tritium (T), which is introduced in the equation (1.1). The required fuel for the fusion power plant will be heavy water containing deuterium and lithium as a source of tritium after a reaction with energetic neutrons [2], p. 26–28.

$$\mathrm{D} + \mathrm{T} \rightarrow \alpha(3.5\,\mathrm{MeV}) + \mathrm{n}(14.1\,\mathrm{MeV}) \tag{1.1}$$

More detailed information about the fusion reactions and reasons why the DT reaction was chosen as the best for the first generation of the fusion power plants is given in [2, 3, 4].

The DT reaction requires to bring nuclei of deuterium and tritium close enough to get the attractive nuclear force stronger than the repulsive electrostatic force. In addition the reaction rate has to be high enough to produce constantly more energy than the power plant operation requires. The optimal fuel temperature for the fusion power plant operation is estimated to be $\sim$ 15 keV [2], p. 67. The fuel on such high temperatures is in the form of the plasma. Simultaneously, there is no material, which can sustain such high temperatures and therefore the plasma has to be confined to prevent a direct contact with the reactor chamber surface.

The currently most promising fusion power plant concept is the tokamak, where the high-temperature plasmas are confined by magnetic fields inside a vacuum chamber. Tokamak consists of the vacuum chamber containing plasma in the shape of the torus, the central solenoid, which drives a current in a plasma, the toroidal and the poloidal magnetic field coils. The magnetic field formed by the coils together with the plasma current driven in the plasma form a twisted helical magnetic field inside the vacuum chamber. The resulting magnetic field secures a charged particles confinement and it balances the kinetic pressure of a hot plasma. The plasma pressure is constant on the magnetic surfaces. Figure 1.1 shows a scheme of the main tokamak plasma components and a formed magnetic field.

The toroidal magnetic field drops with the radial distance from the tokamak center. Therefore there are introduced terms a high field side (HFS), which corresponds to the region closer to the central solenoid, and a low field side (LFS), which represents the outer side of the tokamak chamber. The helicity of the resulting magnetic field lines is mostly influenced by the plasma current profile and by the toroidal magnetic field. The average value of the magnetic field helicity for each magnetic flux surface is represented by the *safety factor* q, given by the equation (1.2) [3], p. 112.

$$q(r) = \frac{r B_\Phi(r)}{R_0 B_\Theta(r)}\,, \tag{1.2}$$

where r is a major radius of the magnetic flux surface, $B_\Phi(r)$ is the poloidal magnetic field, caused by the driven plasma current and the poloidal field coils,

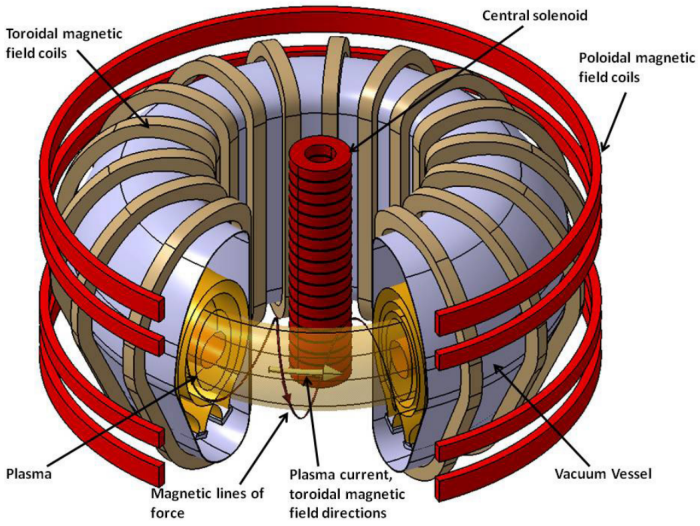

Figure 1.1: A basic tokamak scheme. The toroidal magnetic field coils form a magnetic field in the pure toroidal direction. The plasma current, which is a secondary winding of the central solenoid, creates a poloidal magnetic field together with the poloidal magnetic field coils. A magnetic field compensates plasma outward forces. The surfaces, where the plasma pressure is constant are magnetic surfaces and their shape is represented by the yellow surfaces. The resulting magnetic field lines have a shape of helix, which are wound around the torus [4], p. 28.

R_0 is the tokamak major radius and $B_\Theta(r)$ is the toroidal magnetic field. The lower q is the more twisted field lines are.

The plasma energy is not perfectly confined and there are various channels of the energy losses from the plasma such as the radiation losses or the thermal conduction losses. The quality of the plasma energy confinement by the formed magnetic field is represented by the *energy confinement time* τ_E, defined by the following equation [4], p. 18:

$$\tau_E = \frac{W}{P_{\text{in}} - \frac{\mathrm{d}W}{\mathrm{d}t}}\,, \tag{1.3}$$

where W is a stored kinetic plasma energy and P_{in} is an input net heating power income. Databases of the measured energy confinement times were created based on the experiments realized on various tokamaks, which allows a formulation of the energy confinement scaling laws in purpose to extrapolate τ_E for future devices.

The break-even condition, when fusion reactions are producing at least as much power as it is lost by various channels from the plasma, is represented by the Lawson criterion [4], p. 18:

$$n_{\text{e}} T_{\text{e}} \tau_{\text{E}} > 1.5 \times 10^{21}\ \text{keV}\,\text{s}\,\text{m}^{-3}\,, \tag{1.4}$$

where n_{e} is the electron plasma density and T_{e} is the electron plasma temperature.

1.1 Particles motion and transport

The motions of charged particles in the tokamak magnetic field are superpositions of gyro-motions and guiding center motions. Gyro-motion is represented by the Larmor radius and the cyclotron frequency. They are defined in the following equations:

$$\Omega_{\mathrm{C}} = \frac{QB}{m}\,, \tag{1.5}$$

$$r_{\mathrm{L}} = \frac{mv_{\perp}}{QB}\,, \tag{1.6}$$

where Q is the particle charge, B is a magnetic field, m is the particle mass and $v_{\perp}$ is the particle velocity component perpendicular to the magnetic field B.

There are two main types of the guiding center motion based on the plasma particle initial position and the initial ratio of the particle velocity parallel to the magnetic field so-called pitch.

- **Passing particles.** Guiding center trajectories are circle-like in the horizontal and also in the vertical plane. These particles are passing through the all tokamak poloidal positions and they do not change direction of their velocity component parallel with the magnetic field in the non-collisional conditions. They can be co-passing and counter-passing, moving in the direction of the plasma current and in the opposite direction, respectively.

- **Trapped particles.** As the toroidal magnetic field decreases from the tokamak axis, the twisted magnetic field lines pass through a different magnitudes of the magnetic field. Therefore the guiding center trajectory is a consequence of the mirror effect along the helical magnetic field lines. If the particle pitch, is not in the 'loss cone', the guiding center is oscillating between two turning points of the magnetic field lines. These trajectories are called 'banana trajectories' and some of them also 'potato trajectories' due to their typical shapes.

Besides the particles motion driven by the tokamak magnetic field, the particles undergo random collisions. The random walk process secures a plasma transport even in the perpendicular direction in respect to the magnetic field lines. Three characteristic types of the transport in the tokamaks with a different definition of the characteristic random walk step are distinguished [5], p. 75–90:

- **Classical transport** characteristic random walk step is defined by the particle Larmor radius. This transport is derived for a homogeneous magnetic field, which is not an exact case of the tokamaks. Therefore the classical diffusion coefficients predicts better confinement than it is measured by orders.

- **Neoclassical transport** considers the mirror effect of the twisted magnetic field lines, causing banana orbits. The banana width is significantly bigger than the Larmor radius, therefore the neoclassical transport is faster than the classical one. Nevertheless, the experimentally observed transport in the plasma is even faster. However, some specific modes of the operation lead to the neoclassical transport.

- **Anomalous transport** is driven by the turbulence and it is observed in the experiments. It is faster than the classical or the neoclassical transport.

The transport inside the tokamak plasma is also influenced by presence of the magneto-hydrodynamic modes (MHD), which can degrade the confinement.

1.2 Plasma current terms

The plasma current I_{P} in the tokamak is essential for formation of the poloidal magnetic field and has to be direct current (DC). The plasma current in the tokamaks consists of the inductively driven current, so-called *bootstrap current* and current driven by additional systems. The bootstrap current is a consequence of the Coulomb friction between passing and trapped particles [6] and it is proportional to the plasma pressure gradient. It can drive a significant amount of the total plasma current. The additional current drive systems are listed in the following chapter, as most of them are simultaneously used as the additional heating systems.

2. Additional plasma heating and current drive

Tokamak plasma is heated by the plasma current. This joule heating is usually referred to as ohmic heating. However, it is possible to reach maximum plasma temperatures of only $T \sim 3\,\mathrm{keV}$ by the ohmic heating due to the decrease of plasma resistivity R with plasma temperature T [2], p. 537–540.

$$R \sim T^{-\frac{3}{2}} \tag{2.1}$$

The inductively driven plasma current is generated by increasing the current of the poloidal coils, mainly the central solenoid, which cannot grow to infinity. Therefore it cannot be applied in the steady-state operation. Part of the plasma current is driven non-inductively without any additional system by the bootstrap current. However, it is impossible to drive the plasma current by the bootstrap current exclusively [7], p. 209–210. Therefore the development of additional plasma heating techniques and current drive systems was deemed necessary. The additional heating/current drive systems should manage to heat up the plasma to the desired temperatures and replace the inductive plasma current drive. There are two different principles used, neutral beam injection and radio-frequency heating.

2.1 Radio-frequency heating

Radio-frequency heating (RF) accelerates the plasma particles by a RF wave propagating through the plasma. Based on the plasma parameters, there are several natural frequencies that are adsorbed by the plasma. Based on this frequencies we describe several categories of useful RF heating implementations for the plasma heating and the current drive. All RF heating systems have similar basic scheme: a high power wave source, a transmission line with minimized power losses and an antenna effectively launching the wave into the plasma. Nowadays, there are three leading types of RF heating /current drive systems:

- electron cyclotron resonance, used effectively for both the electron cyclotron resonance heating (ECRH) and the electron cyclotron current drive (ECCD)
- lower hybrid resonance, which is mainly used for the lower hybrid current drive (LHCD)
- ion cyclotron resonance heating (ICRH)

The following subsections will give only brief overview of these methods based on [2, 3, 4].

2.1.1 Electron cyclotron resonance heating and current drive

The electron cyclotron resonance heating (ECRH) and current drive (ECCD) is based on a resonant energy transfer to the plasma electrons from the RF waves

with frequency close to the plasma electron cyclotron frequency, given by the magnetic field. Suitable frequencies for various tokamaks are listed in the table 2.1. The only kind of a source with a suitable power in the frequency ranges is a gyrotron.

tokamak name	TCV	DIII-D	AUGD	JT-60U	ITER
frequency [GHz]	82.7/110	110	105/140	110	170

Table 2.1: Overview of the used gyrotron frequencies for the electron cyclotron heating and current drive at chosen tokamaks [4], p. 727.

The advantage of ECRH and ECCD is its localization. The wave power is effectively absorbed only around the intersection of the RF wave path and the corresponding resonant magnetic surface. The localized heating is effective at controlling and suppression of formed magnetic islands and another plasma instabilities if combined with proper aiming and feedback capabilities. ECRH helps to avoid impurity accumulation in the plasma core by increasing the outward diffusion of heavy impurities. The weakness of ECRH is the fact that the RF waves cannot propagate through plasmas with densities above the cut-off density given by the RF waves frequency. This problem can be overcome by using 2^{nd} or higher harmonic RF waves for the plasma heating.

2.1.2 Ion cyclotron resonance heating

Ion cyclotron resonance heating (ICRH) uses RF waves with frequencies in range from 30 MHz to 120 MHz [4], p. 612, which are produced by vacuum tetrodes. The RF waves propagate in the plasmas with densities above a lower cut-off density. Therefore the antennas have to be placed at the edge of plasmas, in the region where the plasma density will certainly be above the lower cut-off density. If the antenna is out of the plasma or inside low plasma density region, the wave coupling is ineffective. This is an evident problem for the steady state operation, because permanent exposition of the antenna to the plasma will speed up antenna damage. The coupling between 1^{st} harmonic wave in the single ion species plasma is weak. Therefore the 2^{nd} harmonic or a resonance with other plasma species are used (so called minority heating). The minority heating efficiency increases with the minority ion concentration up to the critical value [3], p. 277.

2.1.3 Lower hybrid current drive

Lower hybrid current drive (LHCD) utilizes RF waves with frequencies in between ion and electron cyclotron frequencies, usually from 2.5 GHz to 8 GHz [4], p. 612, which can be generated by klystrons. In the past, the lower hybrid waves were tested for ion heating. But, it was found that the lower hybrid waves are the most effective additional non-inductive current drive. The LHCD power is usually absorbed in the off-axis region. However, the lower hybrid current drive have a similar problem as the ion cyclotron resonance heating, the antenna has to be placed at the edge of a plasma to avoid wave reflection back into the antenna. Successful experiments with tests of lower-hybrid antennas were performed also at IPP CAS, Prague [8, 9].

2.2 Neutral beam injection

Neutral beam injection (NBI) heating is based on injection of fast neutrals into the plasma. The injected neutrals have energies significantly higher than the plasma temperatures T. The fast neutrals injected into a plasma are ionized by various collisions and the newly formed fast ions transfer their energy to the bulk plasma particles by Coulomb collisions. The newly formed fast ions have the same velocity as the original fast neutrals. The NBI fast ions can drive an additional plasma current. This current is partially shielded by bulk plasma electrons as they collide with the fast ions [4], p. 554–560.

Beam attenuation in the plasma is discussed extensively in the subsection 2.2.1. Formation of the neutral beam itself is described in the subsection 2.2.2.

2.2.1 Interaction of fast neutrals with a plasma

The tokamak magnetic fields do not have any impact on neutral particles unlike charged particles. Therefore the fast injected neutrals, mostly deuterium or hydrogen atoms, travel in straight lines independent of magnetic field lines until they are ionized by collisions. Possible collisions leading to the ionization of fast neutrals for a case of the deuterium fast neutrals and the deuterium plasma are listed in the table 2.2.

resonant charge-exchange	$\mathrm{D}^0_{\mathrm{NBI}} + \mathrm{D}^+_{\mathrm{plasma}} \rightarrow \mathrm{D}^+_{\mathrm{NBI}} + \mathrm{D}^0_{\mathrm{plasma}}$
charge-exchange with impurities	$\mathrm{D}^0_{\mathrm{NBI}} + \mathrm{X}^+_{\mathrm{plasma}} \rightarrow \mathrm{D}^+_{\mathrm{NBI}} + \mathrm{X}^0_{\mathrm{plasma}}$
ionization by ions	$\mathrm{D}^0_{\mathrm{NBI}} + \mathrm{D}^+_{\mathrm{plasma}} \rightarrow \mathrm{D}^+_{\mathrm{NBI}} + \mathrm{D}^+_{\mathrm{plasma}} + \mathrm{e}$
ionization by impurities	$\mathrm{D}^0_{\mathrm{NBI}} + \mathrm{X}^+_{\mathrm{plasma}} \rightarrow \mathrm{D}^+_{\mathrm{NBI}} + \mathrm{X}^+_{\mathrm{plasma}} + \mathrm{e}$
ionization by electrons	$\mathrm{D}^0_{\mathrm{NBI}} + \mathrm{e} \rightarrow \mathrm{D}^+_{\mathrm{NBI}} + 2\mathrm{e}$

Table 2.2: List of possible ionization collisions between injected fast atoms, deuterium in this case, and deuterium plasma particles [4], p. 537.

The collisions between plasma particles and fast neutrals can cause also excitation of the fast neutrals. The excited fast neutrals can undergo same types of collisions as listed in the table 2.2, but usually with higher cross-sections than in the ground state. The ionization considering intermediate excitation is called a multi-step ionization and its impact increases with the kinetic energy of the NBI particles [10]. The resulting NBI beam intensity I attenuation along its trajectory x, assuming single species beam, is described by the following equation:

$$\frac{\mathrm{d}I}{\mathrm{d}x} = -n_{\mathrm{e}}\sigma_{\mathrm{tot}} I \,, \tag{2.2}$$

where n_{e} is the electron plasma density and σ_{tot} is the total stopping cross-section, which is a sum of all cross-sections of reactions mentioned in the table 2.2, including multi-step ionization. Generally, the total stopping cross-section is decreasing with the neutral energy, which means that faster neutrals have a longer mean free path through the plasma. Therefore the optimal NBI energy differs with the requested NBI trajectory length through the plasma column and the plasma density.

The neutral beams can be injected into the plasma from various directions. NBIs injection axis are mostly situated at the tokamak plasma midplane ($Z = 0$) or under small angle with respect to it in the vertical plane. There are three main orientation groups in the horizontal plane: tangential co-current, tangential counter-current and radial. By the terms co-current and the counter-current the injection direction with respect to the plasma current I_P is meant. Tangential orientation is usually used for heating NBIs and radial injection for diagnostic one. Heating NBIs are usually oriented tangentially and co-current due to the fact that fast ions originating from the injected neutrals are better confined, since their velocity is mainly parallel with the toroidal magnetic field. On the other hand the advantage of more radial beam orientation is a shorter requested mean free path of the beam particles across the plasma, which eliminates required NBI nominal energy.

When the fast neutrals are ionized and they become fast ions, they are guided by the magnetic field and they are slowed down via Coulomb collisions with plasma particles. The interaction of formed fast ions with the bulk plasma is discussed in the chapter 3.

2.2.2 Neutral beam formation

Beam of fast neutrals is formed by neutralization of accelerated ions. The ions, which are accelerated, can be positive or negative. As the NBIs on the COMPASS tokamak are based on the positive ions, a brief description of the neutral beam formation based on the positive ions, usually hydrogen isotopes, is given. A neutral beam injector consists of these main parts: an ion source, acceleration grids, a neutralizer and a bending magnet. A shorter description of the components follows below.

- **Ion source** is filled by working gas and a plasma discharge is ignited in it to produce a sufficient amount of ions. The most common working gases are hydrogen or deuterium. Helium and tritium are used in special applications. The requested ions are atomic H^+ or D^+. However the discharge in the hydrogen gas produces also molecular ions such as H_2^+, H_3^+ and H_2O^+ or D_2^+, D_3^+ and D_2O^+. The type of the plasma discharge inside the ion source has an impact on the ratio and the total amount of formed ions. Currently, the most common discharges types are the radio frequency (RF) discharge and the arc discharge. Their differences are discussed in [11] and [4], p. 575–579. NBIs installed on the COMPASS tokamak employs the RF discharge.

- **Acceleration grids** are usually systems of three or four grids. They are responsible for the extraction of sufficient number of ions from the ion source, the uniform acceleration and the properer focusing of the extracted beams. There are small holes drilled in the grids in the way to keep grids transparency as high as possible. Each hole extracts and accelerates a small beam called a *beamlet*. All beamlets are directed into the beam focus. The resulting beam is a sum of all small beamlets. The grids size, the beam focus and the beamlet divergence define a profile of the resulting beam.

- **Neutralizer** is a region, where the accelerated ions are neutralized. The neutralization is usually secured by the collisions of the accelerated ions

with the gas target in the case of the NBI based on the positive ions. The gas target is usually the same gas as the working gas in the ion source.

A part of the newly formed fast neutrals is re-ionized as they collide again with the gas inside the neutralizer. The neutralized fraction of the original accelerated ions for a collisionally thick gas target, so-called neutralization efficiency f_{neut}, depends on the change-exchange cross section σ_{CX} and the ionization cross section σ_{i}, as defined in the equation (2.3) [2], p. 548.

$$f_{\mathrm{neut}} = \frac{\sigma_{\mathrm{CX}}}{\sigma_{\mathrm{i}} + \sigma_{\mathrm{CX}}}\,, \tag{2.3}$$

This neutralization efficiency is decreasing with the nominal NBI energy E_{B} for positive ion based beams as can be seen in the figure 2.1. Therefore NBIs based on positive ions are usually used only for beam energies up to $\sim$ 100 keV. Negative ion based NBIs are used if the required NBI energy is higher than $\sim$ 100 keV, because of the better neutralization efficiency.

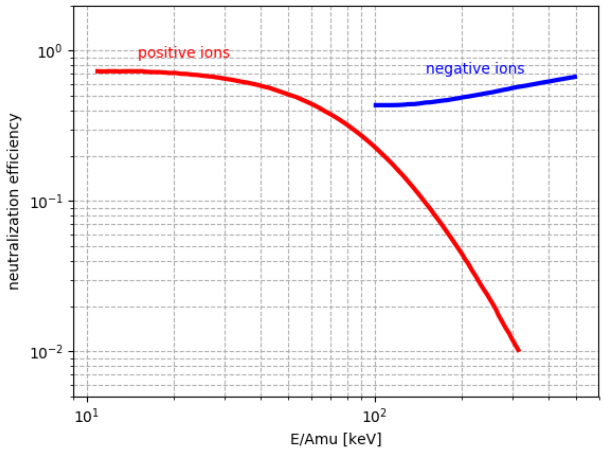

Figure 2.1: Neutralization efficiency of the positive ions and negative ions based beams in respect to the mono-energetic beam energy per Amu for hydrogen isotopes. Image reprinted from [2], p. 548.

The molecular ions are also accelerated and enter the neutralizer. As they collide with the neutralizer gas target they dissociate. The produced atomic fast ions are neutralized by the charge-exchange collisions with the neutral gas. The fast neutrals originating in molecular ions have a fraction of their original energy, $E_{\mathrm{B}}/2$, $E_{\mathrm{B}}/3$, $E_{\mathrm{B}}/10$ in case of the deuterium working gas.

The gas which propagates outside the neutralizer is pumped out at the output of neutralizer by vacuum pumps with a high pumping speed to prevent its diffusion into the connecting port and the tokamak chamber.

- **Bending magnet** deflects the remaining fast ions out of the formed beam into a positive ion dump and a negative ion dump. If the fast ions would remain in the injected beam, they would be deflected by the tokamak magnetic field on the unshielded surfaces. This can lead to the damage to the tokamak.

The connection between the NBI output and the tokamak port is so-called *beam duct*. A beam dump is installed at the opposite side of the beam duct inlet to prevent the damage to the tokamak chamber by the fast neutrals which passed through the plasma without any interaction. However the beam dump installation is not a mandatory, if there are other ways how to prevent an exposition of the tokamak surfaces to the fast neutrals.

A calorimeter is placed into the neutral beam trajectory in the case when beam conditioning is requested. A schematic diagram of NBI is depicted in the figure 2.2.

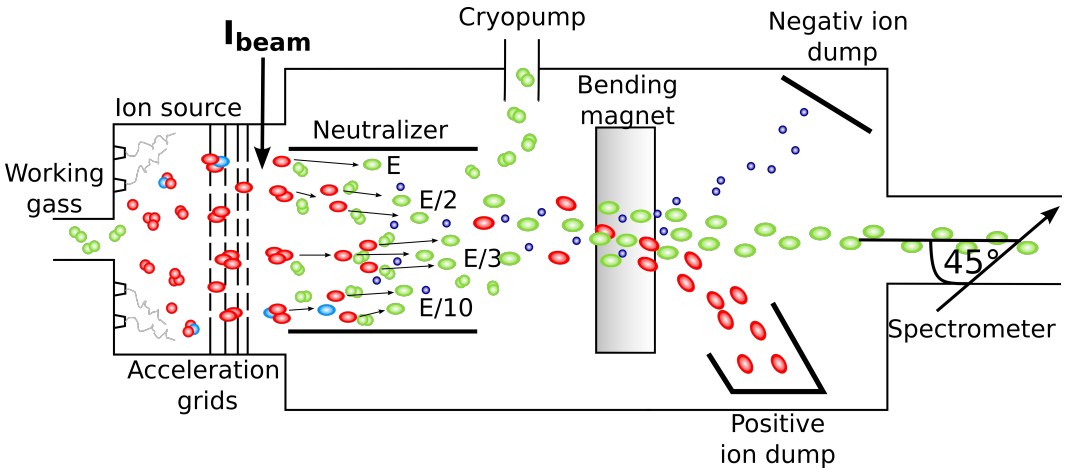

Figure 2.2: A diagram of the neutral beam injector. The working gas is ionized inside the ion source. Both atomic and molecular ions are formed. The ions are accelerated by grids and they are neutralized by collisions with the gas target inside the neutralizer. The molecular ions dissociate into atoms with a fractional energy. The remaining gas is pumped out by cryopumps in the case of the COMPASS NBIs. The bending magnet deflects remaining charged particles out of the formed beam into dumps. The spectrometer is commonly used for analysis of NBI parameters and its viewing angle is $\sim 45°$ in the case of the COMPASS NBIs. Image reprinted from [12].

The resulting beam parameters differs with the produced power. Despite the focus of the ion optical system is fixed, the divergence of beamlets varies. The beamlet divergence scales with a parameter called perveance, which depends on the NBI extracted current I_{beam} and the acceleration voltage U_{beam}.

$$\text{perveance} = \frac{I_{\mathrm{beam}}}{U_{\mathrm{beam}}^{3/2}} \tag{2.4}$$

3. Fast ions interaction with a bulk plasma

There are different sources of fast ions with energies several times higher than the plasma temperature: fusion reactions, radio-frequency heating (RF) and neutral beam injection (NBI). The fast ions are slowed down by the Coulomb collisions with the plasma and they transfer their energy in the bulk plasma particles. It leads usually to the increase of plasma temperature and rotation, which has various consequences on the plasma parameters. Moreover, high velocities of fast ions magnify some phenomena related to the shape of the ion trajectories in the tokamak magnetic field, which could be usually neglected in case of the bulk plasma ions.

Therefore this chapter firstly focuses on the description of fast ions trajectories. It is followed by the description, how the fast ions are slowed down or lost. Than the impact of the fast ions or the NBI neutrals presence inside the plasma on the global plasma parameters and particular MHD instabilities is discussed.

3.1 Fast ions trajectories

Fast ions trajectories follow general rules of the charged particles motion in a magnetic field. The fast ions motion consists from a gyro-motion, defined by the Larmor radius and the cyclotron frequency in the equations (1.5), (1.6), and a guiding center motion. The guiding center motion follows strictly the magnetic field lines in the case of straight homogeneous magnetic field without collisions. If the magnetic field lines are curved or if the magnetic field is inhomogeneous, various guiding center drifts are present. The curvature and the gradient of the tokamak magnetic fields cause a vertical drift, which leads to the particle guiding-center motion across the magnetic flux surfaces, and it is defined in the following equation:

$$\vec{v_{\mathrm{d}}} = -\frac{v^2 + v_{\parallel}^2}{2\Omega_{\mathrm{C}} R}\vec{z}\,, \tag{3.1}$$

where $\vec{v_{\mathrm{d}}}$ is the vertical drift velocity, v is the particle velocity, Ω_{C} is the cyclotron frequency and R is the major radius [7], p. 131. The vertical drift is downward for positive ions and upward for negative ions and electrons. The expected change separation by the opposite drift direction is prevented by the helical shape of the tokamak magnetic field lines. As the particle energy increases, the magnitude of the vertical drift increase. Therefore it is important especially for the fast particles guiding center motion.

Additionally, fast ions as the other plasma particles can be passing or trapped due to the mirror effect caused by the twisted magnetic field lines. Based on the shape of the fast ions guiding center trajectories, four main types of the guiding center orbits are distinguished: passing, stagnation, potato and banana orbits. Examples of poloidal/torodidal projections of such trajectories are shown in the figure 3.1.

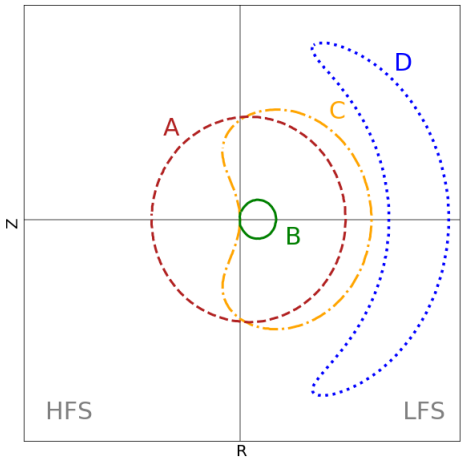

Figure 3.1: Examples of possible fast ions orbits in the tokamak magnetic field (toroidal/poloidal projection). Trajectory of the passing particle is designated by A, the stagnation particle by B, the potato orbit by C and the banana orbit by D. HFS stands for the high field side of the tokamak and LFS stands for the low field side of the tokamak. Reprinted from [7], p.134

The passing particle trajectories traverse closely adjacent magnetic surfaces and therefore they can be approximated by a single magnetic surface. Stagnation particles trajectories are a special kind of the passing trajectories. The main difference is that the stagnation particles do not move across magnetic axis despite they are circle-like in the cross section. This is caused by a significant vertical drift leading into trajectory passing through magnetic surfaces. Potato and banana orbits are trajectories of trapped particles and at least part of each of them is located at the low field side. The main difference is that potato orbits have one of the midplane ($Z = 0$) crossing point at the high field side. Fast ions banana and potato orbits are wider than for bulk plasma ions because their widths are proportional to the Larmor radius, [7] p. 130.

The trajectory type, the fast ion follows, depends on the fast ions initial velocity and direction. In case of the NBI ions, their initial velocity and direction are given by the NBI injection direction and the penetration depth of NBI neutrals, which is given by the ionization cross section of the fast neutrals along the NBI path.

If the fast ions initial velocity is in the plasma current direction (co-current), the banana orbits initially drive ions towards the high field side, deeper into the plasma. If the ions initial velocity is in the opposite direction to the plasma current (counter-current), the banana orbits initially drive ions into the low field side, closer to the tokamak wall. The same phenomena is valid also for the co-current and counter-current passing particles. This difference between co- and counter-current fast ions is a consequence of the vertical drift, defined in the equation (3.1). Therefore there are additional losses of the fast ions that are formed close to the plasma edge in case of the counter-current injection of NBI. Since getting more outward from the plasma might lead to collisions with tokamak

structures. The trajectories of the particles with the same starting position but opposite directions of the velocity in respect to the plasma current for both, banana and passing orbits, are shown in the figure 3.2.

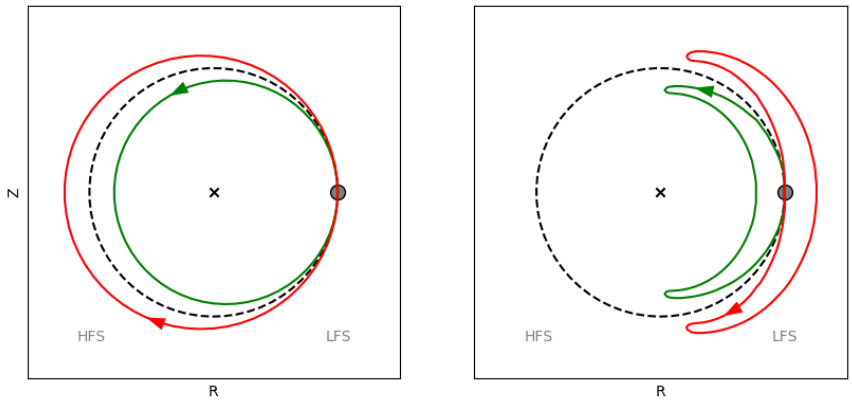

Figure 3.2: Passing (left) and banana (right) orbits of the co-current (green) and counter-current (red) ions. A dashed line represents the flux surface of the original particle position (grey marker). The co-current ions are driven inside the original flux surface and counter current vice versa. Reprinted from [2], p. 480 and 486, adjusted for the ions case.

3.2 Fast ions slowing down

NBI fast ions are slowed down by Coulomb collisions with the bulk plasma. The initial velocity of fast ions is identical to the primary NBI neutral velocity v_B. The NBI fast ions velocity v_B is between the velocity of the bulk plasma ions v_i and the velocity of the bulk plasma electrons v_e.

$$v_\mathrm{i} \ll v_\mathrm{B} \ll v_\mathrm{e} \tag{3.2}$$

Therefore the NBI fast ions can transfer their energy via Coulomb collisions into both, the bulk plasma ions and electrons. Total NBI heating power P of bulk plasma is then a sum of the power transferred to plasma electrons P_e and to ions P_i:

$$P = P_\mathrm{e} + P_\mathrm{i} = \frac{2m_\mathrm{e}^{1/2} m_\mathrm{B} A_\mathrm{D} E_\mathrm{B}}{3(2\pi)^{1/2} T_\mathrm{e}^{3/2}} + \frac{m_\mathrm{B}^{5/2} A_\mathrm{D}}{2^{2/3} m_\mathrm{i} E_\mathrm{B}}\,, \tag{3.3}$$

where

$$A_\mathrm{D} = \frac{n_\mathrm{e} e^4 \ln\Lambda}{2\pi\epsilon_0^2 m_\mathrm{B}^2} \tag{3.4}$$

and ϵ_0 is the vacuum permittivity, e is the elementary charge, m_e and m_i are electron and ion masses, m_B is a mass of NBI fast ions, n_e is an electron plasma density, T_e is a plasma electron temperature, $\ln\Lambda$ is the Coulomb logarithm and E_B is an actual energy of NBI fast ions [3], p. 246–247. The ratio of power transmitted into the electrons and into ions ($P_\mathrm{e}/P_\mathrm{i}$) increases with the energy of

the fast ions. P_e and P_i are equal if the fast ion energy reaches the critical value of E_C:

$$E_C = 14.8 \frac{A_B}{A_i^{2/3}} T_e \,, \tag{3.5}$$

where A_B and A_i are atomic masses of NBI and plasma ions.

If the energy of the NBI fast neutrals is higher than the critical energy E_C, formed fast ions are initially more likely to transfer their energy into plasma electrons than plasma ions. The deflection of fast ions from its original direction due to collisions with electrons is negligible, because their difference in masses $m_e \ll m_B$. As the fast ion energy drops towards the critical energy E_C, they start to collide more likely with plasma ions instead with electrons. The fast ions are scattered from their original direction by ion-ion collisions, because $m_i \sim m_B$. Finally, the fast ion pitch, the fraction of the parallel velocity component in respect to the local magnetic field lines, becomes purely random. The thermalization process of the fast ions is finished, when the fast ions energy is comparable with the bulk plasma ions.

The rate of fast ions slowing down is characterised by the fast ions slowing down time τ_s:

$$\tau_s = \frac{\tau_{se}}{3} \ln \left(1 + \left(\frac{E_B}{E_C} \right)^{3/2} \right) , \tag{3.6}$$

where E_B is the initial NBI fast ions energy and τ_{se} is the slowing down time of the fast ions on the plasma electrons [3], p. 246–249, defined as:

$$\tau_{se} = \frac{3\,(2\pi)^{1/2}\, T_e^{3/2}}{m_e^{1/2} m_B A_D} \sim \frac{T_e^{3/2}}{n_e} \,. \tag{3.7}$$

If we consider the deuterium beam injection with the beam energy $E_B = 40\,\mathrm{keV}$ into the deuterium plasma with the electron temperature $T_e = 1\,\mathrm{keV}$ and the electron density $n_e = 2\text{–}10 \times 10^{19}\,\mathrm{m}^{-3}$, which are typical core plasma values for the COMPASS tokamak discharges, the critical energy $E_C = 18.6\,\mathrm{keV}$ and the slowing down time $\tau_s = 10\text{–}50\,\mathrm{ms}$.

3.3 Fast ions losses

Despite optimizations of NBI energy, orientation, beam geometry and other parameters, there is always a part of the NBI injected neutrals and the NBI fast ions lost by various channels, which are listed below.

- **Shine-through losses** represent neutrals from the NBI which were not ionized. They simply pass through a plasma and end up on the a tokamak wall. The losses are considerable when the plasma is collisionally thin, which means that the beam trajectory across the plasma is shorter or comparable with the ionization mean free path of the beam neutrals.

- **Orbit losses** are caused by fast ions trajectories ending on the tokamak wall. Even guiding center trajectories passing only close to a tokamak wall can lead to the fast ions loss if their Larmor radius is wider than the distance

between the guiding center trajectory and the tokamak wall. The losses of the fast ions, which are lost via the orbit losses before the fast ions finish their first orbit, are called first orbit losses.

- **Charge-exchange losses** are a consequence of collisions between fast ions and background neutrals. They lead to the re-neutralization of fast ions, so they do not follow magnetic field anymore and can end up on the tokamak wall. A part of the re-neutralized fast ions is not lost as the fast neutrals can be ionized again by a next collision with the plasma particles before the fast neutrals escape the plasma.

- **Ripple losses** are caused by the loss cone of the magnetic mirror effect due to the finite number of toroidal coils and they are special kind of the orbit losses. The toroidal field between toroidal coils is weaker than in the close vicinity of the coils. As the ratio between the highest and the lowest magnetic field at specific position, i.e. radius R and height z, decreases, the ripple becomes negligible. The ripple losses are localized at the low field side plasma edge.

- **MHD induced losses** are a consequence of the fast ions interaction with so-called magneto-hydrodynamic (MHD) instabilities. The MHD instabilities impact fast ions by various channels, based on the MHD instability kind. They can cause direct expulsion of the fast ions from the plasma, an additional slowing down or a redistribution of fast ions.

The amount of the lost NBI power depends on the beam energy, the beam orientation with respect to the tokamak and the plasma current direction and on plasma parameters, especially the plasma density or the neutrals density, which are responsible for the charge-exchange losses. The shine through losses are negligible for collisionally thick plasmas. The orbit losses depend on the NBI ionization profile, as it defines initial conditions for fast ions. If the beam particles are mainly ionized at the plasma edge, they follow guiding center trajectories ending on or passing close to the tokamak wall more likely. The orbit losses also depend on the orientation of initial fast ions velocity with respect to the plasma current, as seen in the figure 3.2. When a fast neutral with a toroidal velocity component oriented parallel with the plasma current is ionized, the resulting fast ion is on an outer part of its banana orbit and will subsequently move deeper into the plasma. On the other hand, if a fast neutral with antiparallel direction is ionized in the same location, the resulting fast ion is on the inner part of its banana orbit, therefore it will be subsequently guided towards the tokamak wall, increasing the probability of open trajectory or fast ion loss due to its large Larmor radius. The CX losses are mainly influenced by the background neutral density, which is decreasing towards the plasma core. Therefore, fast ions born closer to a plasma edge are lost more likely.

3.4 Impact of the neutral beam injection on the global plasma parameters

The primary goal of using NBIs is to heat a plasma and drive an additional plasma current. However, NBI heating also affects other plasma parameters. The overview of the expected impacts of NBI on the global plasma parameters follows in this section.

3.4.1 Halo neutrals

NBI injection is responsible for a modification of the local thermal neutral density. NBI neutrals undergo charge-exchange collisions (CX) with plasma ions which become neutrals, but with the energy distribution of the original bulk plasma ions. As the mean-free path of the neutrals decreases with their decreasing energy, the newly formed neutrals undergo another collisions including CX with plasma ions very likely. Through consequent collisions, a cloud of thermal neutrals around NBI is formed. These neutrals are called the halo neutrals. Beam-based diagnostic such as charge-exchange recombination spectroscopy and beam emission spectroscopy [13], fast ion D_α spectroscopy [14], active neutral particle analysis [15] take advantage of the presence of these halo neutrals. On the other hand, the halo neutrals can cause local increase of the fast ions charge-exchange losses.

3.4.2 Kinetic profiles and energy confinement time

The impact of the NBI heating on the plasma kinetic profiles, such as plasma density or temperatures, and energy confinement time depends on the NBI deposition and plasma transport. However the plasma transport can be affected by the presence of the NBI fast ions. If the plasma temperature is increased, the chaotic thermal motion of the plasma particles also grows up, which leads to additional transport and consequently increase of the plasma energy and particle losses. Therefore the plasma confinement degrades with the total input plasma heating P_{in}, including additional plasma heating by NBI. This is reflected in the energy confinement time τ_{E} scalings, which predict $\tau_{\mathrm{E}} \sim P_{\mathrm{in}}^{\alpha}$ with α in range from -0.7 up to -0.3 as can be seen later for example in equations (6.10), (6.12) or (6.13).

If the NBI energy E_{B} is optimal for the plasma density, the NBI energy is deposited mainly in the plasma core. However if the NBI deposition profile is localized out of the plasma core, it can cause flattening of the kinetic profiles, such as plasma density or temperatures, between plasma core and NBI deposition location [2], p. 469–472.

3.4.3 Plasma rotation

The NBI is injected in one direction with respect to the plasma, transferring an additional momentum. The additional momentum spins up the plasma to significant rotation velocities in comparison with an intrinsic spinning plasma. Cross sections of collisions between NBI particles and plasma particles depend on their relative speed. As the plasma rotates in the same direction as the NBI

is injected, the relative collisional energy drops and consequently collisional cross sections are modified [16].

3.4.4 Neutron yield

In the future, the main source of neutrons will be the fusion reaction of the high-energy tail of Maxwellian distributed bulk plasma ions. The neutrons originating in this reaction are called the *thermonuclear neutrons*. They are significant only for the biggest tokamaks, where the ion temperature and confinement are sufficient. Nowadays, the main source of neutrons in tokamaks is a collision between bulk plasma ions and NBI fast ions, they are called *beam-target neutrons*. Another source of neutrons is a collision between NBI particles, so called *beam-beam neutrons*, which production increases with NBI's ions density. In case of the medium sized tokamaks, such as the COMPASS tokamak, we can expect, that the beam-target neutrons are dominant and their yield is given by the following formula:

$$s_{\mathrm{beam-target}} = n_{\mathrm{e}} n_{\mathrm{fi}} \langle \sigma_{\mathrm{DD}} v_{\mathrm{col}} \rangle \,, \tag{3.8}$$

where $s_{\mathrm{beam-target}}$ is the neutron yield, n_{e} is the plasma density, n_{fi} is the fast ion density, σ_{DD} is the cross section for the fusion reaction between two deuterium atoms, DD reaction, as deuterium is the mostly used working gas for the tokamak experiments nowadays, and v_{col} is the collisional velocity between the bulk plasma ions and NBI fast ions. The fusion cross-sections for DD and DT reactions are in the figure 3.3.

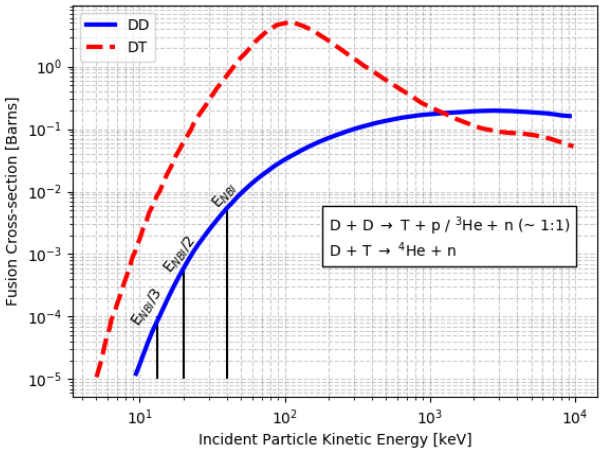

Figure 3.3: The fusion cross-section for DD and DT reaction as function of the beam energy [4], p. 22. The COMPASS specific NBI energies are highlighted by black lines.

NBIs power is partially transferred into a plasma as its additional momentum, as discussed above. The additional plasma rotation is in the same direction as the NBI injection direction. Therefore, the relative collisional velocity is reduced. If the relative collisional energy drops, the DD cross section is also reduced, as can be seen on the fusion cross section in figure 3.3. Therefore, the highest neutron yield is achieved during so-called balance injection, when NBIs are injected in both

the co- and counter-current orientation with such powers that their additional momentum delivered to the plasma cancel out [17].

3.5 Impact of NBI fast ions on the MHD instabilities

So-called MHD instabilities are derived from magneto-hydrodynamic equations (MHD), which describe plasma behaviour. They are driven by two quantities: plasma pressure and plasma current. Pressure driven instabilities are unstable due to a pressure gradient limit. Current driven instabilities are unstable as a consequence of the parallel current component limit in respect to the magnetic field. The overview of MHD instabilities is given in [18]. NBI heating affects most of them, because it drives an additional plasma current and increases plasma pressure as a consequence of plasma temperature increase. There are also instabilities directly driven by fast ions inside plasmas. Following subsections discuss more into detail only the sawtooth instability and edge localized modes, because their experimental observations on the COMPASS tokamak are analyzed in chapter 7.

3.5.1 Sawtooth instability

The so-called sawtooth crash is connected with a destabilized internal kink mode (mode numbers $m, n = 1$), which is a current driven core localized mode, defined with the safety factor $q = 1$ [18]. As central heating is applied, the core plasma is hotter, which leads into peaking of the plasma current ($R \sim T_e^{-3/2}$) and increase of the pressure gradient. When the plasma current is peaked enough, q becomes < 1 and the kink mode can become unstable and the sawtooth crash occurs. During the crash, a part of the hotter plasma is ejected from the central part delimited by an inverse radius r_{inv}, where $q < 1$. This causes the flattening of the peaked temperature and density profiles, which means a drop inside r_{inv} and an increase outside. This sudden redistribution is well visible on temporal evolution of the temperature and density localized signals with a typical sawtooth shape. After the crash, the plasma current profile is also flattened, which means that the shear of the magnetic field lines is abruptly changed, as reconnection happens. An overview of the sawtooth behavior is given in [19].

The presence of fast ions inside and around the kink mode can have both stabilizing and destabilizing effect. There are two phenomena affecting the sawtooth stability, which are driven by the NBI fast ions. The first is the plasma rotation, which generally stabilizes the sawtooth instability. If the plasma velocity increases as the NBI heating is applied, the sawtooth instability is more stable. However, the resulting impact of the NBI heating on the plasma velocity and consequently on the sawtooth instability depends on the NBI injection direction and the direction of the intrinsic plasma rotation, as the resulting plasma velocity can be lower than the intrinsic one. The stabilizing effect by the plasma rotation is dominant for highly rotating plasmas.

The second phenomena affecting the sawtooth instability is opposite effect of ∇B drift on co- and counter-passing fast ions born in the vicinity of $q = 1$ surface. The co-passing fast ions are moving inside $q = 1$ surface mainly in the

so-called favourable curvature region and they are contributing to the kink mode stabilization. Because the ∇B drift has an opposite effect for counter-passing fast ions guiding center motion, as shown in the figure 3.2, they are moving inside $q = 1$ surface at the adverse so-called unfavourable region and leads to the kink mode destabilization [20]. The drifts of particles in a vicinity of $q = 1$ surface and the favourable and the unfavourable curvature regions are shown in figure 3.4.

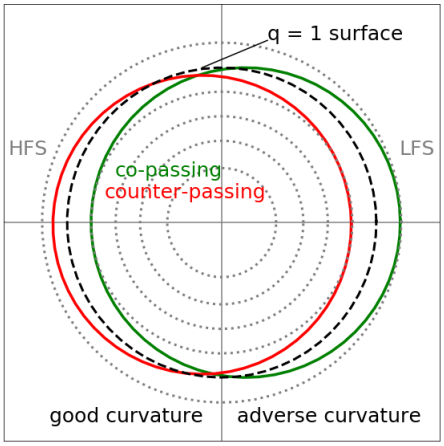

Figure 3.4: The ∇B drift causes that the co-passing and counter-passing fast ions in the vicinity of the $q = 1$ magnetic surface move inside the $q = 1$ surface mainly at the high field side (HFS) and low field side (LFS) respectively. If the fast ions move inside the $q = 1$ magnetic surface at the high field side (favourable curvature region) they stabilize the kink-mode and vice versa for the low field side (adverse curvature region) [21, 22].

3.5.2 Edge localized modes

Edge localized modes (ELMs) accompany the high confinement mode of plasma, so-called *H-mode*. The main characteristic of the H-mode is a region located close to the last closed flux surface (the separatrix), where the sheared perpendicular plasma rotation is driven by $E \times B$ forces. The rotation suppresses turbulences leading to the local neoclassical transport and consequently steep gradient in a plasma pressure and a high bootstrap current. This region is called a *pedestal*. Thanks to the steep gradients, the H-mode confines plasma energy about two times better than a standard plasma mode, called *L-mode* (low confinement mode).

As mentioned in the introduction of this section, the MHD stability is limited by the pressure gradient or the parallel current. The pedestal region can exceed both of these limits. When the MHD stability limits are surpassed, the burst of heat flux towards plasma wall occurs, pedestal gradients drop below MHD limits and start to grow again. These bursts are edge localized modes, ELMs. Because ELMs can be caused by different MHD instabilities, they have different behaviour. Based on the experimental observations, there are two main kinds of

ELMs: Type I and Type III. The observable quantity to distinguish these types is $\mathrm{d}f_{\mathrm{ELM}}/\mathrm{d}P_{\mathrm{sep\,norm}}$, where f_{ELM} is ELM frequency and $P_{\mathrm{sep\,norm}}$ is a power passing through the separatrix normed to the separatrix surface. If the ELMs frequency decreases with the normed power through the separatrix, $\mathrm{d}f_{\mathrm{ELM}}/\mathrm{d}P_{\mathrm{sep\,norm}}$ is negative, the ELMs are considered to be Type III and vice versa for Type I ELMs.

- **Type I ELMs** are big ELMs caused by the pressure gradient limitation. Because they are limited by a pressure gradient, despite increasing $P_{\mathrm{sep\,norm}}$ they reach similar pressure gradient limit. Therefore a lost plasma energy per ELM is almost constant and the ELM frequency f_{ELM} grows with $P_{\mathrm{sep\,norm}}$.
- **Type III ELMs** are thought to be caused by passing the pedestal current limit. As their frequency f_{ELM} drops with $P_{\mathrm{sep\,norm}}$, their limiting pressure gradient increases and also realized energy per ELM.

In general, the released energy per ELM is higher for Type I ELMs, therefore the aim is to avoid them, because they can cause damage to plasma facing components. On the other hand, ELMs flush the fusion ash (helium) and plasma impurities across the pedestal, which prevents the impurity accumulation in the plasma and its consequent radiation collapse. Therefore the research is focused on an H-mode scenario development with small and frequent ELMs and a high plasma energy content or another advanced scenarios without any sudden plasma bursts and simultaneously with a sufficient impurity transport. More detailed description of ELMs mechanism and experimental results is given in [23, 24].

A use of the additional plasma heating leads to the increase of $P_{\mathrm{sep\,norm}}$ and consequently has an impact on the ELMs frequency. Simultaneously, the ELMs affect the fast ions content in the vicinity of the sepatratrix [25] and can affect the fast ions velocity [26].

3.6 Fast ions diagnostics

The presence of the fast ions is measured by various diagnostics. The oldest one is the neutral particle analyzer (NPA), which detects energy and mass resolved fluxes of the fast neutrals escaping plasma. The fast neutrals are products of the charge-exchange reactions of fast ions and neutrals, usually background or halo neutrals.

Another particle-based diagnostic is the fast ion loss detector (FILD), which detects plasma fast ions directly. FILD head is inserted into the edge region of the plasma and the fast ions can enter a small slit. The FILD head shape secures that only fast ions enter the slit. There is a detector mesh inside the FILD head, which counts incident particles. The position on the FILD detector correspond to the fast ions pitch-energy space [27].

The last broadly used fast ions diagnostic is a fast ion D-α (FIDA). FIDA observes a diagnostic beam with several view lines, which serves as an additional neutral source for the charge-exchange, and measures light in a vicinity of the D-α line. As the plasma fast ions collide with beam neutrals, halo or background

neutrals, some of them are excited and the excitation energy is almost immediately radiated as a D-α photon. However, the wavelength is Doppler-shifted, as it is radiated by a fast neutral. Therefore, there is a branch of the measured D-α, which wavelength shift from the original line corresponds to the pitch-energy space of the original fast ions, and the branch intensity is proportional to the fast ions local density [14].

As two of three usually used fast ions diagnostics are based on the charge-exchange reaction, I have been also working on the background neutral density detection. The background neutral density is one of the inputs for the synthetic diagnostics, which are essential for the further analysis of FIDA and NPA.

4. Tokamak COMPASS and its additional heating system

Tokamak COMPASS was originally constructed and operated by UKAEA at Culham, UK. It was moved to IPP, CAS, CR in 2007. The tokamak COMPASS has the same magnetic configuration as the ITER tokamak and it is 1:10 proportionally smaller in a size. Therefore it is a perfect testing device for the ITER tokamak [28, 29]. The overview of basic COMPASS parameters is given in the table 4.1.

Major radius R	0.56 m
Minor radius a	0.23 m
Maximum plasma current I_P	400 kA
Toroidal magnetic field on axis B_t	0.9–2.1 T
Maximum puls duration	$\sim$ 1 s

Table 4.1: The tokamak COMPASS basic parameters [29].

The following section 4.1 introduces the tokamak COMPASS diagnostics systems, which are exploited for this thesis. The section 4.2 describes the neutral beam heating system installed on the COMPASS tokamak.

4.1 COMPASS diagnostics

The tokamak COMPASS is equipped by a wide range of diagnostics [30]. Diagnostics exploited for this thesis are listed below:

- **Magnetic diagnostics** provide inputs for the EFIT equilibrium reconstruction and the plasma current I_P measurements. The EFIT solves the Grad-Shafranov equation (4.1) and it simultaneously employs a boundary condition, that a kinetic plasma pressure on the separatrix is zero [31, 32].

$$R^2\nabla\left(\frac{\nabla\psi}{R^2}\right) = -\mu_0 R^2\frac{\mathrm{d}p}{\mathrm{d}\psi} - j\frac{\mathrm{d}j}{\mathrm{d}\psi}\,, \tag{4.1}$$

  where R is the tokamak major radius, ψ is the magnetic flux, μ_0 is the vacuum permeability, p is the plasma pressure and j is the plasma current density.

  The outputs of the Grad-Shafranov equation solution are profiles of the toroidal current density and the plasma pressure gradient profiles as functions of the magnetic fluxes and a map of the magnetic fluxes. The condition $p_\mathrm{separatrix} = 0$ allows to determine pressure profile and consequently the stored energy in the plasma W_EFIT. The EFIT reconstruction employed on the COMPASS does not include any correction on the centrifugal pressure caused by the plasma rotation or correction to the NBI fast ions presence [33].

- **Soft X-rays (SXR)** are mainly produced by a bremsstrahlung radiation and are also emitted by plasma impurities. Three pinhole cameras with 2×35 and 1×20 channels are installed on the COMPASS tokamak for the tomographic reconstruction of the plasma radiation. The cameras detect photons in energy range 1–13 keV with a time resolution 3 μs, which allows detection of MHD instabilities evolution such as the sawtooth instability [34].

- **Thomson scattering** radiation of electrons is triggered by a laser passing through the plasma. Electron temperature T_e and density n_e profiles are determined from intensities of the scattered spectral lines and their FWHMs. There are four Nd:YAG lasers, each with 30 Hz repetition rate, and two collection objectives installed on the COMPASS tokamak. One objective with 24 view-lines is dedicated to a plasma core and second one with 30 view-lines is directed at the plasma edge. [35, 36].

- **Interferometer** measures the line integrated density $\langle n_e \rangle$, which is inferred from the phase shift difference of microwaves passing through the plasma with respect to reference waves. The COMPASS interferometer is unique by its two similar wavelengths adjustment [37].

- **Radiometer** detects frequencies in a range of the electron cyclotron emission (ECE) by 16 channels. Magnitudes of signals are proportional to local electron temperatures. Usually the radiometer collects directly ECE waves, however COMPASS operates often with over-dense plasmas. Despite that, the local electron temperatures can be derived from the radiometer signals thanks to the EBW-X-O conversion [38, 39, 40].

- **Neutron detection** is provided by a couple of unshielded NaI(Tl) scintillation detectors, a composite ZnS(Ag) scintillation detector shielded by 10 cm of lead and by a ^{3}He detector with a count rate 33 counts/s [30, 41]. Data in this thesis were measured by the ZnS(Ag) detector.

- **Neutral particle analyzer (NPA)** measures energy spectra of escaping neutral atoms from the plasma, mainly hydrogen and deuterium. NPA collects thermal or super-thermal atom fluxes. Currently, the NPA is the only diagnostic on the COMPASS providing information about ion temperatures or fast ion behaviour. Therefore it is a crucial diagnostic for NBI impact studies and it is described more into the detail in the following subsection.

4.1.1 Neutral particle analyzer

Neutral particle analyzer (NPA) collects atoms ejected from the plasma, which are products of the charge-exchange collisions of the plasma ions and neutrals presented in the bulk plasma. The neutrals entering the NPA entrance slit are ionized by collisions with nitrogen gas inside a stripping cell. Formed ions are sorted by an electric and a magnetic field into channeltrons, which are 24 in total (12 for hydrogen, 12 for deuterium) in case of ACORD-24, which is installed on the COMPASS tokamak. Scheme of the ACORD-24 is depicted in the figure 4.1.

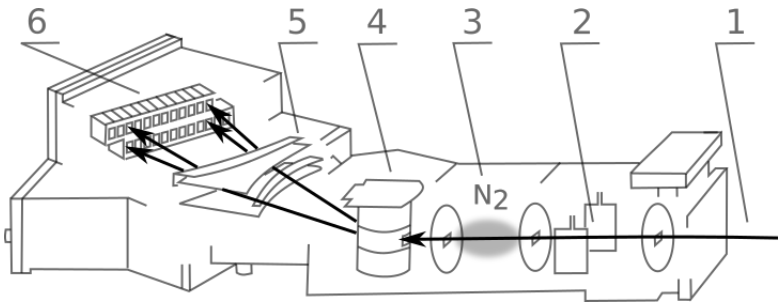

Figure 4.1: Scheme of the neutral particle analyzer ACORD-24 installed on the COMPASS tokamak. Charged particles are deflected from the incident flux of upcoming particles (1) by the electric field (2). Remaining neutrals are ionized while passing through the stripping cell filled by nitrogen (3). Formed fast ions are sorted by the magnetic field (4) and the electric field (5). Finally, sorted ions hit the array of the detectors (6) according to their mass and energy. Reprinted from [42].

The ratio of measured energies by the NPA is given by its geometry, however the variability of the sorting fields allows us to tune measured energy ranges. ACORD-24 is capable to measure hydrogen atoms in the energy range from 0.25 keV to 70 keV and deuterium from 0.3 keV to 50 keV with a time resolution from 1000 μs down to 50 μs [43, 44].

Despite the fusion plasmas are considered as the fully ionized, there are neutrals in the entire volume of a tokamak plasma with energies in the energy range of the ACORD-24. Their origin is as follows. Working gas molecules, mostly hydrogen isotopes, are injected into a tokamak chamber by a gas puff or they are desorbed from tokamak chamber walls, as the walls are heated up during the discharge. As soon as molecules reach the plasma edge, they are dissociated. The formed cold atoms with temperatures $\sim$ 2 eV [45, 46] can undergo charge-exchange (CX) collisions with plasma ions with energies given by local ion temperatures. The products of the CX collisions are atoms with almost same energy distribution as the original plasma ions and thus their temperatures are several orders of magnitude higher than those of the original neutrals. The faster atoms are, the longer mean free paths through the plasma they have. Therefore the CX products can reach even the plasma core. The multi-step CX collisions supply the neutrals into the bulk plasma. This process is depicted in the figure 4.2. Other sources of neutrals inside the COMPASS plasma are ion-electron recombination, which can be omitted for plasma densities below $10^{20}\mathrm{m}^{-3}$ [46], NBI injection, a source of the high-energetic neutrals and consequent halo neutrals in a vicinity of NBI plasma trajectory, or the pellet injection, which is used only for the specific COMPASS experiments [47].

The bulk plasma neutrals propagate independently on the tokamak magnetic field and therefore they can easily escape plasma. The escaping neutrals are detected by the neutral particle analyzer, which measures line integrated escaping neutral fluxes. The measured flux depends on profiles along the plasma NPA sight line of the background neutral density, the plasma ions distribution and the neutral flux attenuation caused by re-ionization collisions of neutrals with plasma particles. The measured neutral flux is expressed by the equation (4.2). The term

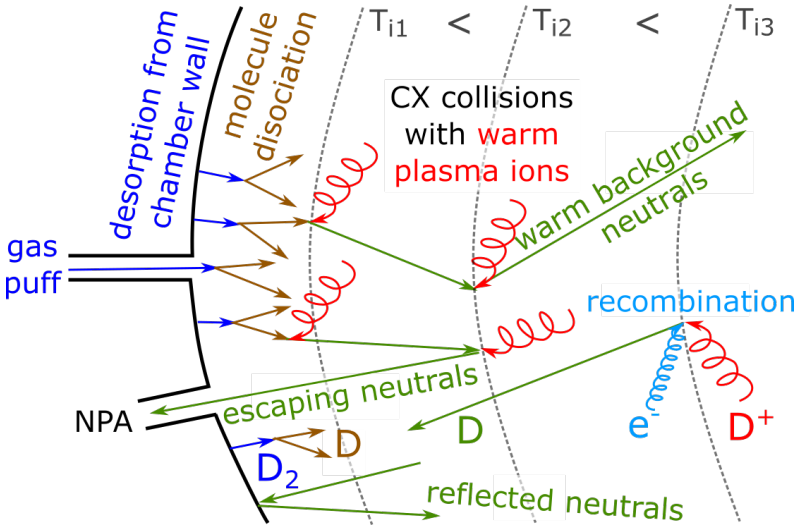

Figure 4.2: Scheme of a formation of background neutrals. Injected or desorbed molecules of the working gas D_2 (blue arrows) dissociate. Formed atoms (brown arrows) have low energies and therefore short mean free paths. When they undergo charge-exchange collision with the plasma ions (red swirls), they form faster atoms with longer mean free path (green arrows). The newly formed fast neutrals undergo multiple CX collisions and produce fast neutrals with same energies as the plasma ions have. The other source of the background neutrals is recombination collisions of plasma ions and electrons (cyan arrow). Image reprinted from [48].

integrated along the NPA line of sight is called emissivity, as it is expressed in the equation (4.3).

$$\Gamma(E_n) = A \int_0^L n_0 \langle \sigma v \rangle_{\mathrm{CX}} n_{\mathrm{i}}(E_n, p, l) \left(\int_0^l \frac{1}{\lambda_{\mathrm{att}}(E_n, l)} \mathrm{d}x \right) \mathrm{d}l \,, \tag{4.2}$$

defining the emissivity as

$$\Gamma(E_n) = \int_0^L \mathrm{emissivity}(E_n, p, l) \mathrm{d}l \,, \tag{4.3}$$

where E_n is the measured energy of n-th channel, A is the geometrical factor including a size of an NPA aperture and an opening angle, L is the length of the NPA view-line, $\langle \sigma v \rangle_{\mathrm{CX}}$ is the CX collision rate, $n_{\mathrm{i}}(E_n, p, l)$ is the density of ions with velocity vectors directed towards the NPA, p is the fraction of the ion velocity vector along the magnetic field lines so called pitch, $\lambda_{\mathrm{att}}(E_n, l)$ represents the re-ionization rate of the formed neutral flux and l describes the path along the NPA view-line. The emissivity function median position along NPA view line moves towards a plasma core with the measured energy. There are two reasons for this phenomena. More energetic ions entering CX collisions are more likely populated in the plasma core as the ion temperature is usually highest in the plasma core. A second reason is that the faster neutrals are the less probable their re-ionization is. Therefore the emissivity of each measured neutral flux is different based on the neutrals energy.

As the NPA signal depends on several plasma parameters, it's analysis can be used to infer different plasma quantities, which are listed below.

- **Ion temperature** is determined from the slope of the measured energy spectra in the logarithmic scale, when thermal energy range is set. If we assume that the majority of detected neutrals comes from the plasma core, the collected neutrals have the same energy distribution function as the core ions. However, these condition are barely fulfilled and a correction between the determined ion temperature $T_{\mathrm{i\,CX}}$ and the real core ion temperature $T_{i\,0}$ has to be done [49, 43]. The ion temperature determination by this approach is discussed more into detail in the section 6.3.1.

- **Background neutral density profile** can be obtained from the NPA data, if all other quantities in the equation (4.2) are known [50] and the developed method is described in the chapter 8.

- **H/D mix ratio** can be derived from the ratio of hydrogen and deuterium neutral fluxes with the same energy [51].

- **Fast ions behaviour** translates into high-energy neutral fluxes.

For more detailed analysis of the measured fluxes, it is possible to employ synthetic diagnostics such as FIDASIM [52] or DOUBLE [51] .

4.2 NBI on the COMPASS tokamak

The COMPASS tokamak was equipped by ECRH during its operation in the UK. However, this system was not relocated to Prague. The neutral beam injection (NBI) was selected as an additional heating system for COMPASS operation in Prague. Two identical NBI systems were purchased from the Budker Institute of Nuclear Physics, RU [53], each with a power up to 400 kW in produced neutrals. The nominal beam energy is 40 keV which is obtained by a system of four acceleration grids with voltages 40 keV, 32 keV, −500 V and 0 V. Overview of the main COMPASS NBI parameters is given in the table 4.2 and its scheme is depicted in the figure 4.3.

maximum beam power in neutrals	2 × 400 kW
maximum beam current	12 A
maximum beam energy	40 keV
beam duration	$<$ 300 ms
operational gasses	H, D, He
neutralization efficiency	$\sim$ 85% for D
focus	1.86 m
width in focus	$\sim$ 40 mm
grid diameter	167 mm
holes in each grid	887
grid hole diameter	$\sim$ 4 mm

Table 4.2: Base parameters of NBIs on the COMPASS tokamak [53, 54].

Both beams are injected tangentially, usually co-current. The geometrical focus of the NBI grids is aimed into the narrowest part of the beam duct to

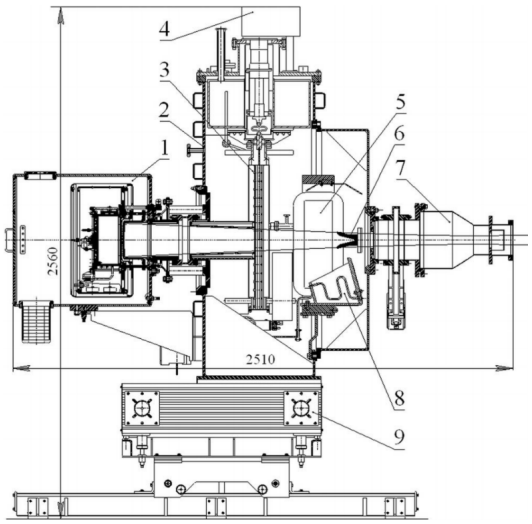

Figure 4.3: Scheme of the COMPASS NBI unit. 1: ion source, 2: vacuum tank, 3: cryopanels, 4: cryocooler head, 5: bending magnet, 6: movable calorimeter, 7: connection to the tokamak, 8: positive ion dump, 9: injector carriage support. Reprinted from [53].

eliminated a beam scraping in the beam duct, as shown in the figure 4.4. The beam duct size is eliminated by the space between the COMPASS toroidal coils.

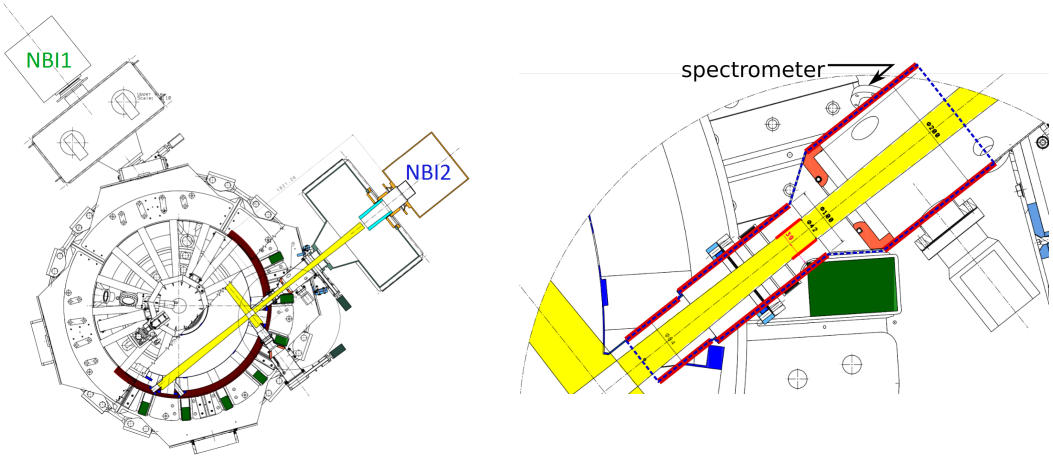

Figure 4.4: Connection of NBIs with the COMPASS vacuum chamber (left) and a detail of the beam duct (right). Thick red lines represent simplified geometry of the duct used for an estimation of the beam losses.

To predict losses caused by a relatively wide beam width in respect to the narrow beam duct, a simple beam model based on measured beam parameters was employed. The beam parameters are derived from the Doppler shifted D_α lines measured by the spectrometer, thermocouples installed in the beam calorimeter and beam electrical quantities, such as the beam current I_{beam} and the acceleration voltage U_{beam}. The following subsections introduce an employed beam model, the beam diagnostics and than the derived power losses in the beam duct.

4.2.1 Beam model

The neutral beams can be described by two different sets of parameters. The less accurate but more simple is a single Gauss beam representation. This model is used to simulate beam inside a plasma, which is far enough from the last beam grid. However, as shown later in this section, we can use this approximation only for a limited range of beam settings. The second approach is to describe a beam using multiple Gaussian beamlets emitted by the grid holes, which is more accurate model. The beamlet approach is described and than the parameters of a single Gaussian beam approach are derived from it. The scheme of a single Gaussian beam and beamlets parameters is depicted in the figure 4.5.

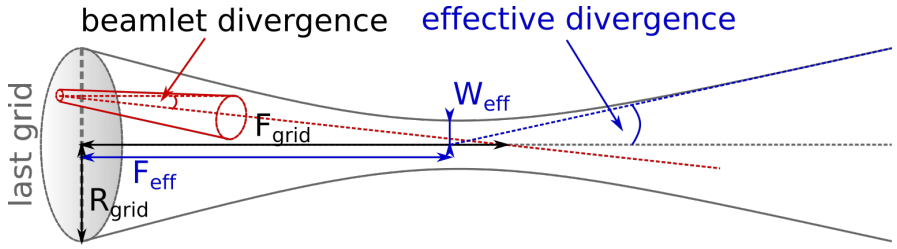

Figure 4.5: A scheme of a single Gaussian beam and beamlets parameters. Beamlet model is described by a grid system geometrical focus F_{grid}, the last grid radius R_{grid} and a beamlet divergence. Single Gaussian model is represented by an effective beam focus F_{eff}, an effective beam waist radius W_{eff} and an effective beam divergence. The waist is the narrowest part of the beam.

There are 887 identical Gaussian beamlets extracted from the last NBI grid holes ($z = 0$) used in the model. The diameter of each hole is $\sim$ 4 mm. Following equations (4.4), (4.5) and (4.6) describe a general Gaussian beam and are employed for both models.

$$W_{\mathrm{z}}(z) = r_{\mathrm{b}}\sqrt{1 + \left(\frac{(z-f)\tan\xi_0}{r_{\mathrm{b}}}\right)^2} \tag{4.4}$$

$$I(r,z) = \left(\pi N_{\mathrm{grid}} W_{\mathrm{z}}^2\right)^{-1} \exp\left[-\left(\frac{r}{W_{\mathrm{z}}}\right)^2\right] \tag{4.5}$$

$$2\pi \int \sum_{N_{\mathrm{grid}}} I_n(r,z)\mathrm{d}r = 1 \tag{4.6}$$

The W_{z} is the 1/e beam/beamlet width in a distance z from the last grid, r_{b} is the beam/beamlet width in its focus f, which is grid focus F_{grid} in the case of the single beam model and the holes position ($z = 0$) in the case of the beamlet model, ξ_0 is the beam/beamlet divergence, I is a beam intensity, N_{grid} is a number of the grid holes in case of beamlet model and one for the single beam model and r is a distance from a beam/beamlet axis. The intensity of the single beamlet is normalized so that the total beam intensity is one.

The grid used in the beamlet model is planar and all beamlets are aimed into the grid focus F_{grid}. The grids are in the reality a spherical segments, but its curvature can be neglected. The model grid and the real one are compared in the figure 4.6.

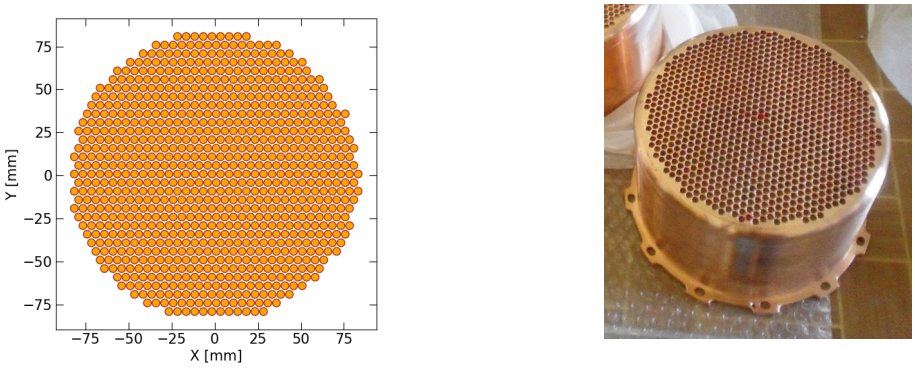

Figure 4.6: A grid used for calculations (left) and a photo of the real one (right) [55].

Examples of several NBI profiles based on the beamlet model for the different beamlet divergences ξ_0 in various distances from the last grid are shown in the figure 4.7. As far as the resulting NBI profile is sufficiently Gaussian, NBI can be described by the single beam model. Therefore NBI profiles derived by the beamlet model are fitted by a single Gaussian shape and effective parameters, employed in the single beam model, are determined. The determined effective single beam parameters as a function of the beamlet divergence ξ_0 are plotted in the figure 4.8.

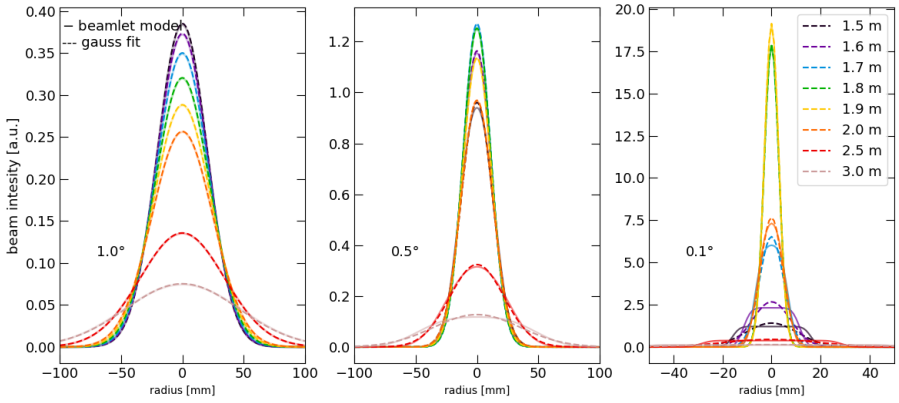

Figure 4.7: NBI profiles for the different beamlet divergences ξ_0 and in the different distances from the last grid are a result of all beamlets contributions (solid lines). The beamlet model profiles are fitted with the single Gaussian (dashed lines). The single Gaussian model fits nicely for the highest beamlet divergence (left), however it is accurate only in the vicinity of the grid focus (grid distance = 1.86 m) in the case of the lowest beamlet divergence. The x-axis on the right panel has different range than two others, as the beam is significantly narrower.

As the beamlet divergence ξ_0 increases, the NBI profiles are more Gaussian-like, see the figure 4.8, but simultaneously the effective parameters are deviating from the NBI ion optical parameters, see the figure 4.8. The total beam effective waist radius W_{eff} and divergence grow and the effective focus F_{eff} moves closer

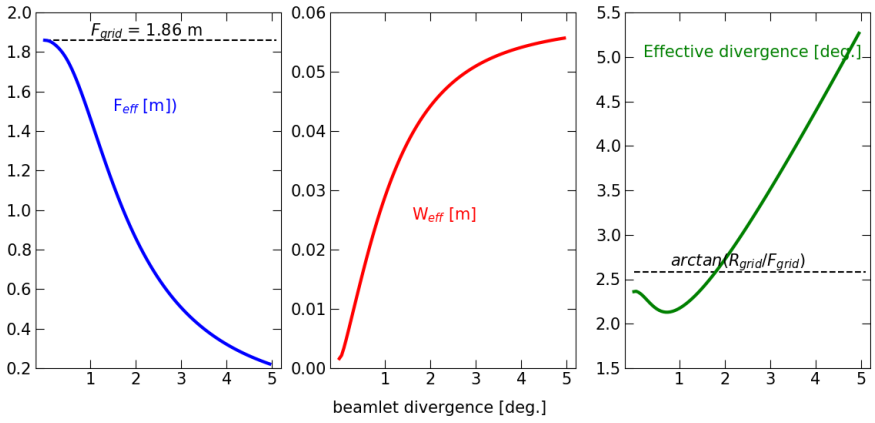

Figure 4.8: Effective NBI parameters characterizing NBI as a single Gaussian beam as a function of the beamlet divergence, which is the beamlet model parameter. The effective parameters of the single beam model are obtained by the fitting outputs of the beamlet model.

to the last grid. Simultaneously the beam is becoming wider in the area of the narrow beam duct.

4.2.2 NBI diagnostics

The parameters of NBI are monitored by a spectrometer, which observes a set of the Doppler shifted D_α lines. Its location is depicted in the figures 2.2 and 4.4. The Doppler shifted D_α lines provide information about the beam composition, the neutralization efficiency and the beamlet divergence [12]. The neutralization efficiency can be also determined from the calorimeter thermocouples.

Doppler shifted spectra

A part of the fast neutrals produced by NBI is excited and it emits light, including D_α lines. Extracted neutrals move with a few discrete energies, 40 keV, 20 keV, 13.3 keV and 4 keV in case of COMPASS NBIs, due to the different kinds of accelerated and consequently dissociated ions (D^+, D_2^+, D_3^+, D_2O^+). Their high speeds lead into significant Doppler shifts of the emitted light, which is described by the following equation:

$$\Delta\lambda_D = \lambda_0 \frac{v_b}{c} cos\Theta_0 \,, \tag{4.7}$$

where $\Delta\lambda_D$ is a line Doppler shift, λ_0 is the wavelength of the original unshifted line, v_b is the velocity of the certain energy beam component, c is the speed of light and Θ_0 is an observation angle with respect to the velocity vector, which is $\sim 45°$ in case of the COMPASS tokamak, as shown in the figure 2.2. The light, including the shifted lines, is collected by the high-resolution spectrometer observing the beam by the window shown in the figure 4.4. An example of the collected spectra is shown in figure the 4.9.

The concentration of the extracted ions by the acceleration grids is directly proportional to the corresponding Doppler shifted line intensity. Therefore it

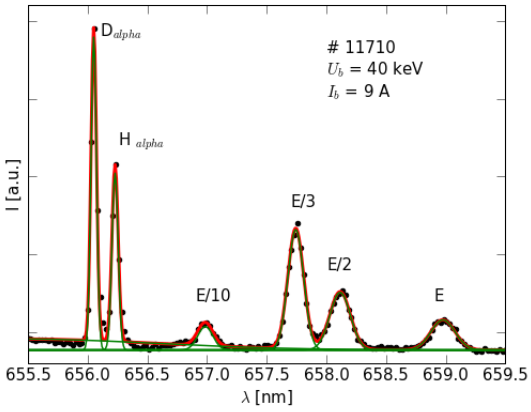

Figure 4.9: An example of the measured NBI spectra. There are unshifted D_α and H_α lines and four Doppler shifted D_α lines, which are emitted by fast neutrals of the different beam energy components. The spectrum is measured by the spectrometer installed in the beam duct under $\sim 45°$ with respect to the NBI axis. Black points represent measured data, red curve is the total fit by several Gaussians and green lines are individual Gaussians.

is possible to determine the extracted ions rations as defined in the following equations:

$$\frac{n_{\mathrm{D}_2^+}}{n_{\mathrm{D}^+}} = c_2 \frac{I_{\mathrm{E}/2}}{I_{\mathrm{E}}}\,, \qquad \frac{n_{\mathrm{D}_3^+}}{n_{\mathrm{D}^+}} = c_3 \frac{I_{\mathrm{E}/3}}{I_{\mathrm{E}}}\,, \qquad \frac{n_{\mathrm{D_2O}^+}}{n_{\mathrm{D}^+}} = c_1 0 \frac{I_{\mathrm{E}/10}}{I_{\mathrm{E}}}\,, \tag{4.8}$$

where n_{D^+}, $n_{\mathrm{D}_2^+}$, $n_{\mathrm{D}_3^+}$ and $n_{\mathrm{D_2O}^+}$ are concentrations of extracted ions by the NBI grids, I_E, $I_{E/2}$, $I_{E/3}$ and $I_{E/10}$ are Doppler shifted lines intensities and c_2, c_3, c_{10} are constants derived from neutralization, excitation, radiation and the dissociation, in case of the molecular ions, cross sections. Since the extracted ion ratios are known, the total measured beam current can be divided between each ions species. Subsequently, the power carried by the each energy component (P_{E}, $P_{\mathrm{E}/2}$, $P_{\mathrm{E}/3}$, $P_{\mathrm{E}/10}$) is calculated as a product of the corresponding ions current, the corresponding neutralization efficiency and the energy of the given component. The total beam power carried by the produced fast neutrals P_{tot} is a sum of power contributions of all beam energy components.

Divergences of beamlets formed by the NBI grid holes are derived from the Doppler shifted line widths, again separately for each beam energy component. Detailed description of the data processing used on the COMPASS is given in my master thesis [56] and partially published in [12], which follows [57, 58] for beam species composition, using cross sections from [59, 60], and [61] is followed for a beamlet divergence. To derive the beamlet divergence following equations are used:

$$\xi_i = \sqrt{\frac{\delta_i^2 - \delta_{\mathrm{s}}^2}{\Delta\lambda_{\mathrm{D}_i}^2 \mathrm{tg}^2\Theta_0} - \frac{R_{\mathrm{grid}}^2}{F_{\mathrm{grid}}^2} - \frac{T_{\|_i}}{E_i \mathrm{tg}^2\Theta_0}} \qquad i = E, E/2, E/3, E/10\,, \tag{4.9}$$

where ξ_i is the beamlet divergence in 1/e beam width, δ_i is 1/e Doppler shifted line width, δ_{s} is the spectrometer instrumental 1/e broadening (FWHM = 0.06,nm for spectrometer used on the COMPASS tokamak), $\Delta\lambda_{\mathrm{D}}$ is the line Doppler shift,

R_{grid} is the NBI grid radius, F_{grid} is the NBI ion optical focus, $T_{\|_i}$ is the parallel temperature of the accelerated neutrals with an energy E_i and Θ_0 is the observing angle ($\sim 45°$ in our case).

The parameters derived by this method for NBI1 are published in [12], however the NBI1 measurements do not cover all possible NBI1 power range. The dependencies of NBI2 parameters on the product of the beam acceleration voltage and the extracted beam current $U_{\mathrm{beam}}I_{\mathrm{beam}}$ are in the figures 4.10, 4.11 and 4.12. All measurements were obtained with the nominal beam voltage $U_{\mathrm{beam}} = 40\,\mathrm{keV}$ during a wide range of the COMPASS experiments. Usually a single spectrum per a single NBI injection is collected. A variation of data points for one value of the extracted beam power $U_{\mathrm{beam}}I_{\mathrm{beam}}$ is given by different NBI conditions during operation such as status of the ion source and the grids surfaces and fraction of heavy particles.

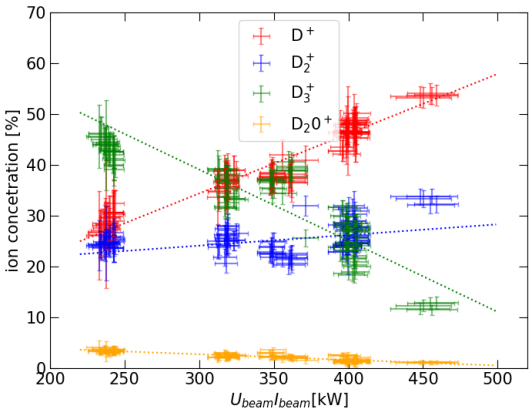

Figure 4.10: Dependence of the extracted ions concentrations on the extracted beam power $U_{\mathrm{beam}}I_{\mathrm{beam}}$ for NBI2.

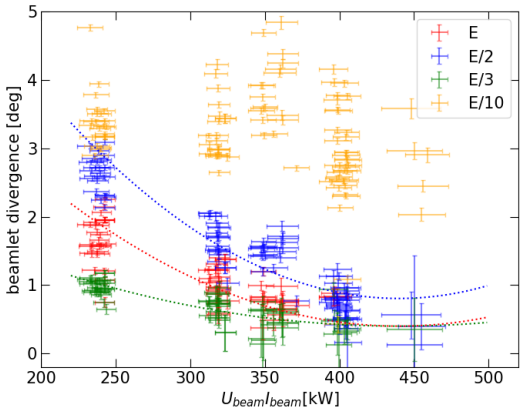

Figure 4.11: Dependence of the NBI2 beamlet divergences ξ_i on the extracted beam $U_{\mathrm{beam}}I_{\mathrm{beam}}$. The beamlet divergence for an energy component $E/10$ is $\sim 4°$ with data points spread $\pm 1°$ without significant dependence.

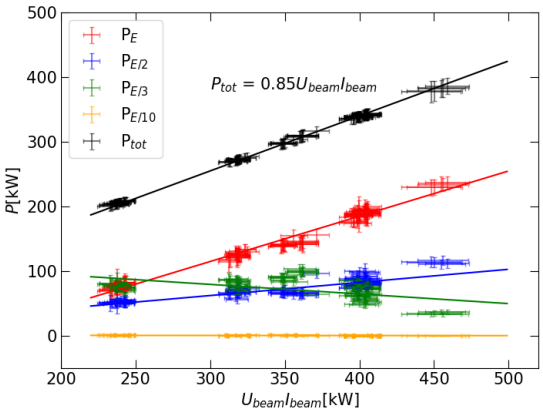

Figure 4.12: Dependence of the total produced NBI2 powers carried by fast neutrals on the extracted beam power $U_{\mathrm{beam}}I_{\mathrm{beam}}$ carried by ions.

The concentration of D^+ ions increases with the extracted beam power carried by ions $U_{\mathrm{beam}}I_{\mathrm{beam}}$ and it is mainly balanced with the drop of the D_3^+ ions concentration, as seen in the figure 4.10. It is given by the increase of the applied RF power into the ion source discharges, which leads to the more efficient molecule dissociation before their acceleration inside the ion source.

The beamlet divergences ξ_i of E, $E/2$ and $E/3$ components reduce with the extracted beam power $U_{\mathrm{beam}}I_{\mathrm{beam}}$, as seen in the figure 4.11. It is in the agreement with the grid system design, which was optimized for the beam current $I_{\mathrm{beam}} \sim 10\,\mathrm{A}$ and the beam voltage $U_{\mathrm{beam}} = 40\,\mathrm{keV}$ [53]. Unfortunately, the additional line broadening caused by the beamlet divergence itself for the highest values of the extracted beam power $U_{\mathrm{beam}}I_{\mathrm{beam}}$ is in range of the method inaccuracy and therefore it is indistinguishable. The general decreasing trend is important for NBI transition through the narrow beam dump as is shown in the section 4.2.3. The beamlet divergence of E/10 component is significantly higher, but does not play a role as the $P_{\mathrm{E/10}}$ is negligible.

Despite different trends of powers carried by fast neutrals for each energy component, their sum P_{tot} is linearly increasing with the extracted beam power carried by ions $U_{\mathrm{beam}}I_{\mathrm{beam}}$ with the factor 0.85, which is the total NBI neutralization efficiency f_{neut}.

Calorimeter thermocouples

The total neutralization NBI efficiency f_{neut} can be also determined from temperature measurements of eight thermocouples installed inside the calorimeter as depicted in the figure 4.13. The integral over time of the thermocouple signal is directly proportional to the applied heating power. However, the proportionality factor depends on many parameters and vary over time how the thermocouples material degrades. Despite that the neutralization efficiency can be determined from a ratio of the thermocouples measurements for a pair of the NBI injections with switched on and switched off bending magnet. When the bending magnet is switched on, the calorimeter is heated only by a power of produced neutrals. While the bending magnet is switched off, the calorimeter is heated by the all

extracted ions from the ion source. The neutralization efficiencies derived from two pairs of the NBI2 injections are shown in the table 4.3.

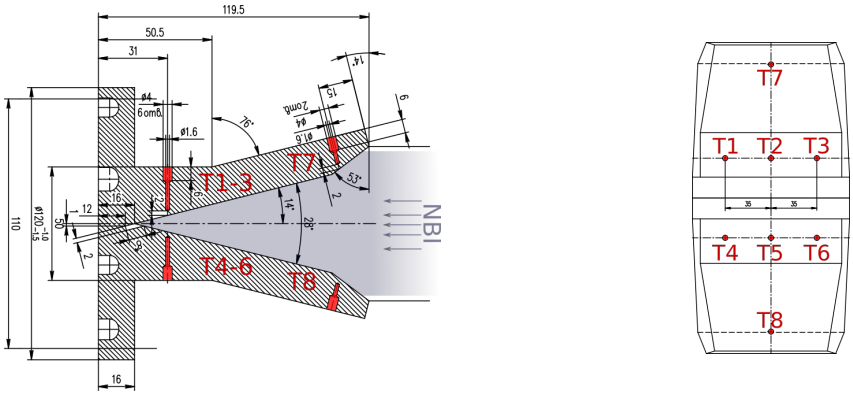

Figure 4.13: Calorimeter side view (left) and front view (right) with the thermocouples locations T1–T8.

$U_{\text{beam}}I_{\text{beam}}$	$\sim$ 360 kW	$\sim$ 400 kW
beam duration	120 ms	20 ms
T1	97.5 %	83.7 %
T2	92.2 %	87.6 %
T3	93.7 %	80.9 %
T4	86.7 %	92.8 %
T5	98.8 %	80.7 %
T6	94.8 %	86.2 %
T7	95.2 %	93.7 %
T8	100 %	100 %
average	94.0 %	86.5 %

Table 4.3: Neutralization efficiency for two different NBI2 settings derived from calorimeter thermocouples measurements.

The thermocouples measurements are slightly higher than the resulting 85 % determined by the spectroscopic measurements. However, a difference between individual thermocouples measurements is significant. As this method requires a pair of identical NBI injections and it does not bring any advantages in comparison with the spectroscopic measurements, it is rarely used.

4.2.3 Power losses in the beam duct

NBIs are injected into the COMPASS tokamak through the narrow beam ducts, as seen in the figure 4.4. The total beam power produced in neutrals P_{tot} is reduced by a power lost inside the beam duct P_{duct} before it is injected into the tokamak as the auxiliary heating power P_{AUX}. There are two common channels of the beam power losses in the beam duct. First, the NBI neutrals can be reionized by collisions with the residual gas inside the beam duct and the formed ions are deflected by the tokamak magnetic field. Second, it is the NBI scraping

due to the narrow beam duct, which can be estimated by a geometrical beam model. Both of these effects are discussed below.

Re-ionization NBI losses

As the beam neutrals are passing through the beam duct, they can be ionized as they collide with the residual gas coming from the tokamak chamber. The re-ionization losses are important only if the mean free path of the beam neutrals in the beam duct is comparable or shorter than the beam duct length. The estimation of the beam neutrals mean free path inside the beam duct is as follows. The ionization cross-section σ_{i} for the studied range of NBI neutrals energies is $\sigma_{\mathrm{i}} \sim 1\text{–}2 \times 10^{-20}\,\mathrm{m}^2$, the pressure of the residual gas p_{gass} inside the beam duct is $\sim 10^{-3}\,\mathrm{Pa}$ and its temperature T_{gas} is assumed to be the room temperature. The gas pressure is measured by the pressure gauge located nearby the NBI duct and it measures a pressure inside the tokamak chamber. As NBI is equipped by own vacuum pumps, the tokamak pressure is considered as the upper limit. The estimation of re-ionization mean free path is given in the following equation:

$$\lambda = (n_{\mathrm{gas}}\sigma_{\mathrm{i}})^{-1} = \frac{k_{\mathrm{B}}T_{\mathrm{gass}}}{p_{\mathrm{gass}}\sigma_{\mathrm{i}}} = 202\text{–}405\ \mathrm{m}\,, \tag{4.10}$$

where n_{gas} is the beam duct residual gas density and k_{B} is the Boltzmann constant. The re-ionization under these conditions causes the NBI losses lower than 1 % per 1 m. Even if the residual gas pressure was one order higher, $10^{-2}\,\mathrm{Pa}$, the lost power would increase up to 5 % per 1 m. Therefore the re-ionization losses are no considered as a part of the beam duct losses as they are negligible in case of the COMPASS tokamak.

Beam duct scraping losses

The effect of the narrow beam duct is assessed by the geometrical beam model described in the section 4.2.1 and by the simplified beam duct geometry for the COMPASS tokamak beam duct. The beam duct is represented by three cylinders, highlighted in the figure 4.4. The passing fraction of NBI varies with the beamlet divergence ξ_0. The examples of the NBI profiles cross-section are shown in the figure 4.14.

The effective beam parameters evolution with the beamlet divergence ξ_0 seen in the figure 4.8 is well visible on the beam vertical cross sections. As the beamlet divergence ξ_0 increases the position of the NBI waist, the narrowest beam location with the effective radius W_{eff}, moves towards the last grid, i.e. the effective beam focus F_{eff} shortens. Consequently the beam is becoming wider in the region of the beam duct which leads to degradation of the passing beam power fraction through the beam duct. The dependence of the beam passing fraction through the beam duct on the beamlet divergence ξ_0 based on the beamlet and the single Gaussian beam model is in the figure 4.15.

The single beam model, which is more simple, matches well the results of the more accurate beamlet model. The beam lost fraction is negligible for the beamlet diverges $\xi_0 < 0.6°$.

If the measured beamlet divergence depicted in the figure 4.11, is combined with the NBI passing fraction through the COMPASS narrow beam duct in the

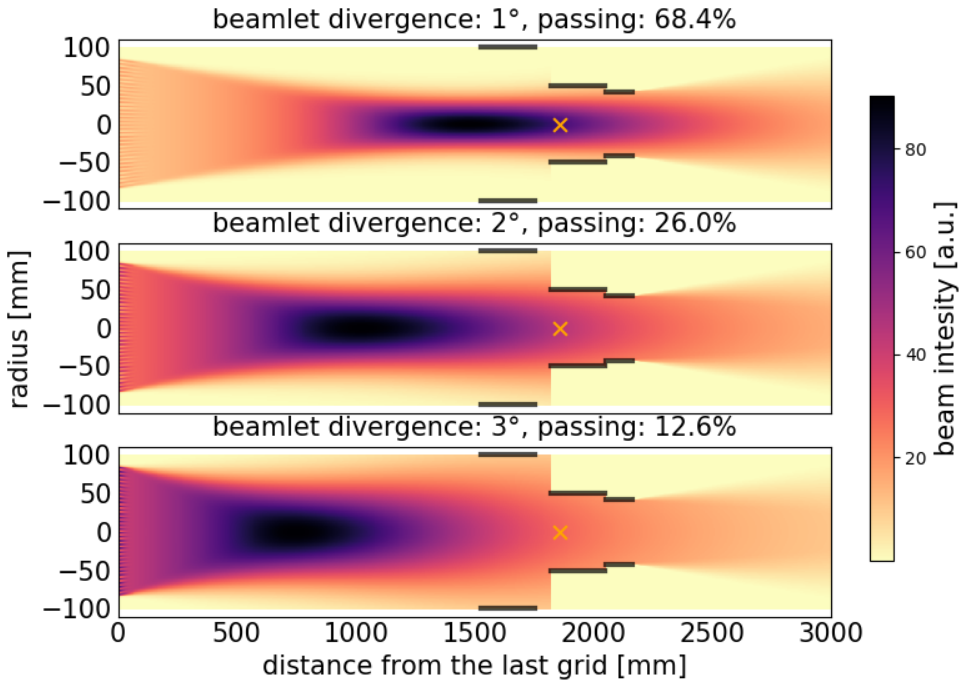

Figure 4.14: Vertical beam cross sections of the NBI installed on the COMPASS tokamak based on the beamlet model, defined by the equations (4.4), (4.5) and (4.6), for different beamlet divergences ξ_0 and the passing power through the cylinders represented by black lines. The orange crosses represent the beam ion grid focus F_{grid}. As the beamlet divergence ξ_0 increases the beam becomes wider and the passing fraction of the beam power through the beam duct is reduced.

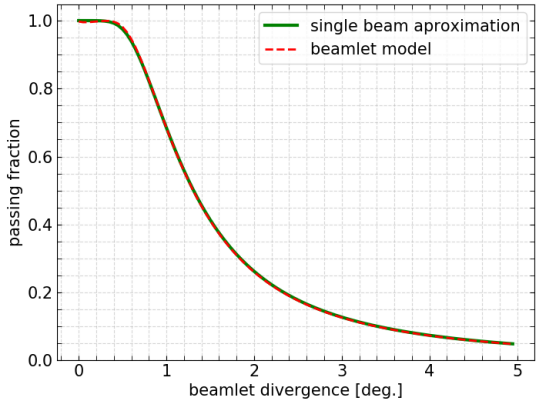

Figure 4.15: Beam passing fraction through the COMPASS narrow beam duct, which is causing the beam scraping, versus the beamlet divergence ξ_0 for the NBIs installed on the COMPASS tokamak. The dashed red line is based on the beamlet model and the the green solid line is based on the single beam model exploiting the effective beam parameters shown in the figure 4.8.

figure 4.15, the passing fraction of the each beam energy component is deduced. By multiplying the passing fractions with the produced powers in each energy component shown in the figure 4.12, the auxiliary heating entering the COMPASS

tokamak P_{AUX} is determined. The passing fractions separately for each energy component are shown in the figure 4.16 and the passing powers, including the power entering the tokamak chamber, i.e. the auxiliary heating power P_{AUX}, are depicted in the figure 4.17.

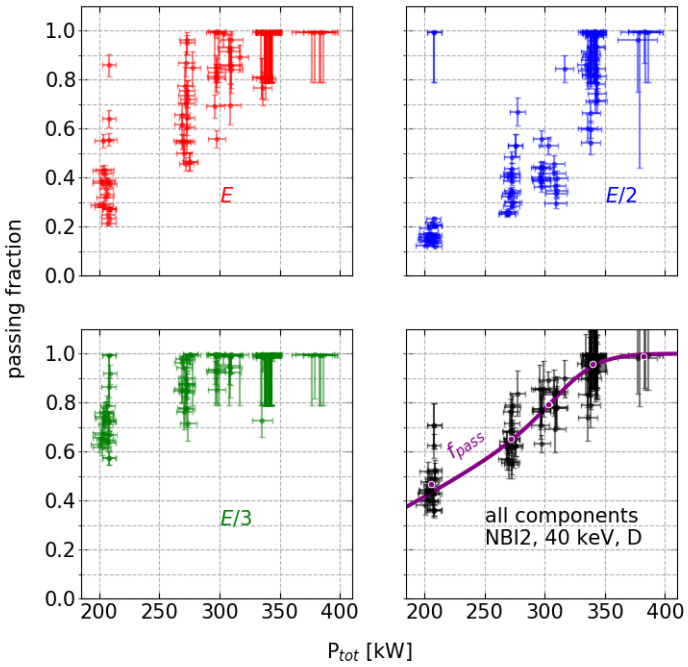

Figure 4.16: The passing beam fraction for each beam energy component and the total power fraction entering the tokamak chamber P_{AUX}/P_{tot}. The E/10 component is not considered as there is almost no power in it and its beamlet divergence is pretty high. In the panel for all components, the violet dots represents mean values of neighbouring points and the violet line is a fit used in the following chapters.

The total NBI power lost due to the narrow beam duct is $\sim$ 50 % in the worst case and improves with the total produced NBI power P_{tot}. As the Doppler shifted spectra measurements are not available each time, it is not possible to derive the beam passing fraction for each individual NBI injection. Therefore it is beneficial to derive a general formula for the total passing fraction dependence, the violet solid line in the figure 4.16. It is fitted by modified hyperbolic tangent function, which is sufficiently variable. The fit is following:

$$f_{\mathrm{pass}} = 0.5 \left[\frac{\exp(x) + f\exp(-x)}{\exp(x) + \exp(-x)} + 1 \right] , \tag{4.11}$$

where

$$x = c(P_{\mathrm{tot}} - p) , \qquad f = a + bP_{\mathrm{tot}} , \qquad P_{\mathrm{tot}} = 0.85 U_{\mathrm{beam}} I_{\mathrm{beam}} , \tag{4.12}$$

$$c = 0.0258 , \quad p = 320 , \quad a = -1.286 , \quad b = 0.00558. \tag{4.13}$$

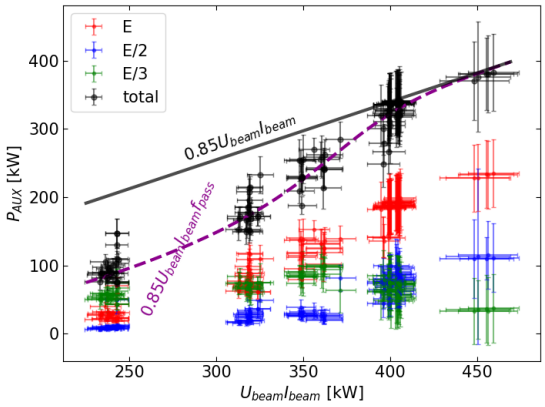

Figure 4.17: Passing power through the narrow beam duct based on the measured NBI beamlet divergences ξ_0 from the figure 4.11 and the calculated beam passing fraction dependence on the beamlet divergence ξ_0 from the figure 4.16. The solid black line represents a case of no losses in the beam duct, total power produced in the fast neutrals P_{tot}, and violet dashed line represents total power entering the COMPASS tokamak chamber P_{AUX}.

To conclude, the NBI auxiliary heating power entering the COMPASS chamber P_{AUX} is derived from the measured Doppler shifted beam spectra and from the derived passing fraction dependence, which is shown in the figure 4.15. If the Doppler spectra are not available, it is possible to employ the determined formula for the passing fraction f_{pass} introduced in the equation (4.11) which requires the beam acceleration voltage U_{beam} and the extracted beam current I_{beam} as the inputs. The re-ionization losses of fast neutrals in the beam duct are omitted as they are negligible in comparison with the beam scraping losses.

5. Campaigns and simulations dedicated to the NBI characterization

Several thousands of NBI-assisted discharges were performed during the COMPASS tokamak operation. Dedicated campaigns operated in the low confinement modes (L-modes) were set up to assess the basic characterisation of the impact of the NBI heating on the plasma. The L-mode is more suitable for the basic characterization as there is a lack of pedestal or L-H transition effects, which can cause ambiguous data interpretation. The vast majority of these discharges was carried out with the NBI injector 2 (NBI2) and several similar discharges were also carried out with the NBI injector 1 (NBI1), depicted in the figure 4.4. Basic dependencies that were intended to be observed, among those the dependencies on the line-averaged plasma density $\langle n_e \rangle$, on the toroidal magnetic field B_t, on the plasma shape and size, depicted in the figure 5.1, and the plasma current I_P including co- and counter- injection. The dedicated NBI characterization campaign in the high confinement mode (H-mode) has never been done, but many H-modes with the NBI heating were realized within other campaigns.The NBI L-modes scans parameters realized on the COMPASS to characterize the NBI impact on the plasma are listed in the table 5.1.

scan type	**varied par.**	**constant par.**
Co-current, NBI2 only experiments:		
Basic	$\langle n_e \rangle = 2\text{–}8 \times 10^{19}$ m^{-3}	$I_P = 180$ kA
(power and density)	$I_{beam} = 6, 8, 10, 12$ A	$B_t = 1.15$ T
Current	$I_P = 140\text{–}220$ kA	$\langle n_e \rangle = 4 \times 10^{19}$ m^{-3}
		$I_{beam} = 8$ A
		$B_t = 1.15$ T
Magnetic field	$B_t = 1\text{–}1.35$ T	$I_P = 180$ kA
		$I_{beam} = 10$ A
		$\langle n_e \rangle = 4 \times 10^{19}$ m^{-3}
Shape	figure 5.1	$I_P = 180$ kA
	$\langle n_e \rangle = 2\text{–}8 \times 10^{19}$ m^{-3}	$B_t = 1.15$ T
	$I_{beam} = 6, 10$ A (8 A)	
Counter-current, NBI2 only experiments:		
Basic	$\langle n_e \rangle = 2\text{–}8 \times 10^{19}$ m^{-3}	$I_P = 180$ kA
	$I_{beam} = 8$, 10 A (6, 12 A)	$B_t = 1.15$ T
Current	$I_P = 140\text{–}220$ A	$\langle n_e \rangle = 4 \times 10^{19}$ m^{-3}
	$I_{beam} = 8, 10$ A	$B_t = 1.15$ T

Table 5.1: An overview of the NBI characterization L-modes parameters.

An example of the NBI assisted L-mode discharge from the NBI dedicated campaign is shown in figure 5.2. As NBI is switched on, both the plasma stored energy derived from the EFIT reconstruction W_{EFIT} and the edge D_α radiation

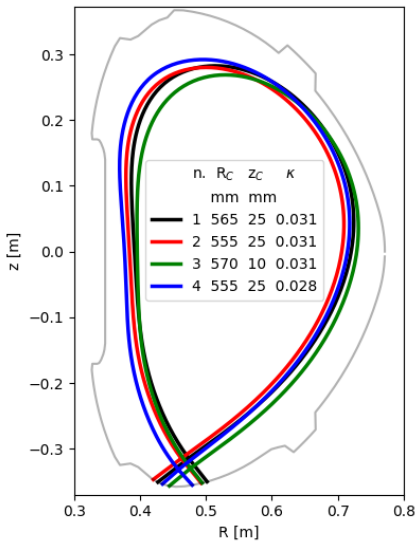

Figure 5.1: Different plasma shapes used in the dedicated L-mode discharges for the NBI characterisation. The shapes have different position of the center (R_C, z_C) and triangularity κ and they are referred by their number n = 1–4 in the following chapters. The grey line represents the first wall boundary.

increase, neutrons are produced, while values of other plasma parameters controlled by a feedback, such as the plasma current I_P or the line-averaged plasma density $< n_e >$, remain unchanged.

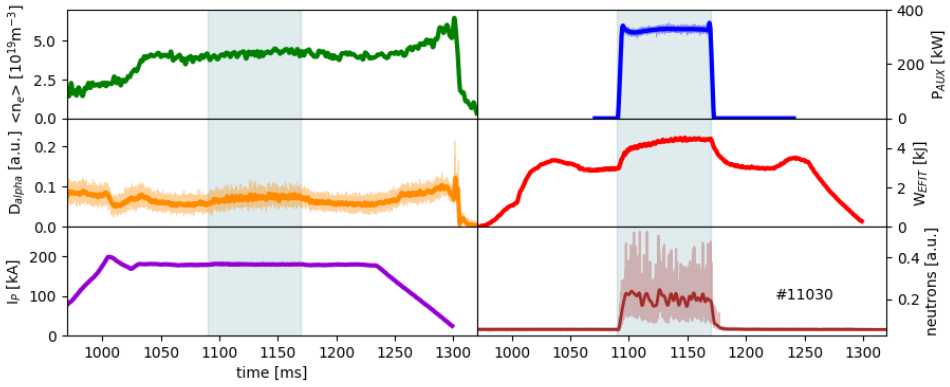

Figure 5.2: An example of basic plasma parameters of an NBI-assisted L-mode. The NBI heated part of the discharge is highlighted by a shaded background. The discharge #11030 is a part of the Basic Co-current scan.

The power balance analysis in the section 6.1 focuses on this transient part of discharges shortly after NBI is switched on. After a few tens of ms, plasma parameters settle on new stable values. The stage of the discharge with constant plasma parameters is so-called flat-top and the majority of the analysis presented in the following chapters 6 and 7 exploits the flat-top stages of discharges.

Different stages of the tokamak discharge are necessary for proper assessment of the NBI heating effect on various phenomena. The requested discharge stages for the various studies in following chapters 6 and 7 are summarized in the ta-

ble 5.2.

	NBI assisted		**Ohmic only**	
	L-mode	H-mode	L-mode	H-mode
power balance	NBI switch on	×	×	×
kinetic profiles	flat-top	flat-top	flat-top	flat-top
energy confinement time	flat-top	flat-top	flat-top	flat-top
sawtooth	flat-top	×	flat-top	×
ELMs	×	flat-top	×	flat-top

Table 5.2: An overview of the requested discharge stage for the different analysis held in the chapters 6 and 7.

Results in the chapter 6 are compared with published simulations performed in FAFNER [62], RISK and METIS [63]. The RISK and METIS simulations are based on the measured COMPASS NBI-assisted discharges parameters, which were a part of the NBI2 co-current basic scan in the table 5.1. Basic plasma parameters of these performed simulations are listed in the table 5.3.

discharge number	$\langle n_e \rangle$ [10^{19} m^{-3}]	B_t [T]	I_p [kA]	P_{AUX} [kW]	injection direction
FAFNER					
-	4	1.2	200	2x300	co-/counter-
-	8	1.2	200	2x300	co-/counter-
RISK/METIS					
11031	5	1.15	180	300	co-
11033	9	1.15	180	300	co-
11034	2	1.15	180	300	co-

Table 5.3: Overview of the FAFNER [62], RISK and METIS [63] simulations parameters, which are later compared with the experimental data. The discharges #11031, #11033 and #11034 are a part of the Basic Co-current scan.

6. Global plasma parameters during NBI heated discharges

The main purpose of the neutral beam injection (NBI) on the COMPASS tokamak is an additional heating of the plasma. The higher total kinetic energy of plasma and presence of the fast ions, which are consequences of the NBI heating, have observable effects on many global plasma parameters. Additionally, there are fusion collisions producing neutrons if the deuterium beams are injected into deuterium plasmas.

The section 6.1 studies so-called power balance, which represents a balance of the plasma power sources and sinks. Assuming that the all plasma power sources and losses, excluding an additional heating term, are known, it is possible to determine a delivered additional heating power. The determined additional heating power is compared with the injected auxiliary power derived in the subsection 4.2.3.

Once the auxiliary heating power of the injected neutrals determined in the section 4.2.3 is confirmed by the power balance results the energy confinement times τ_E of NBI heated discharges are derived, as presented in the section 6.2. This allows to study the impact of the NBI heating on the energy confinement time τ_E.

In the section 6.3 the impact of the NBI heating on the kinetic profiles, the plasma electron and ion temperatures and the plasma density profiles, is assessed.

The last section 6.4 of the chapter discusses briefly measured neutron yield, which is a consequence of the fusion reactions, mainly between NBI fast ions and bulk plasma ions.

6.1 Plasma power balance

In the tokamak plasmas, there are several channels of the power losses. These losses has to be balanced by the power sources in order to achieve a steady state operation. The common power sources are the ohmic heating, the additional plasma heating and the fusion products heating. If the power sinks and sources (excluding auxiliary heating) are determined it is possible to derive the auxiliary heating power, which is delivered in the plasma.

The NBI auxiliary heating power, which enters the tokamak chamber is determined in the section 4.2.3 for the case of the COMPASS tokamak. Since, the additional heating powers derived from the power balance are independent on the used parameters in the section 4.2.3, therefore it is possible to confirm independently the power passing fraction equation (4.11) with the results of the power balance analysis.

There are various losses of the NBI power as NBI is produced and delivered into the tokamak chamber and as NBI particles transfer their energy into the plasma particles. Therefore only a fraction of the power carried by the extracted ions from the NBI ion source actually ends up heating up the plasma. The different NBI loss terms are schematically shown in the figure 6.1.

The procedure of the NBI power delivery into the plasma with the particular

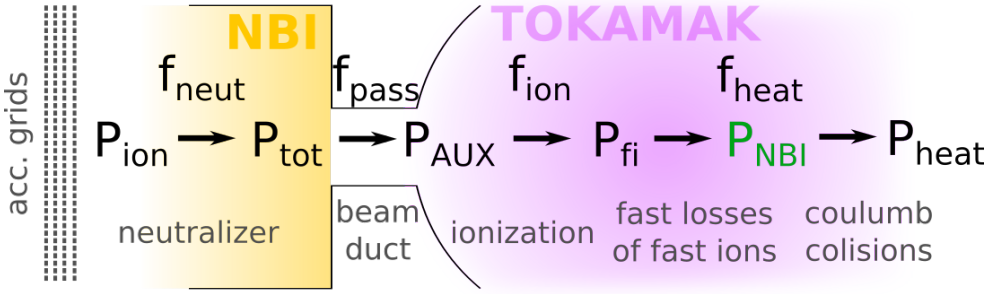

Figure 6.1: Scheme of different quantities related to the additional heating by neutral beam injection. The total power of accelerated ions by the NBI grid system P_{ion}, a product of the beam acceleration voltage U_{beam} and ion current extracted by the grids I_{beam}, is lowered by the fast ions neutralization f_{neut} to the total power in the fast neutrals P_{tot}. The beam is partially scraped in the beam duct and the passing fraction f_{pass} enters the tokamak chamber as the real auxiliary heating power P_{AUX}. The injected fast neutrals are ionized f_{ion} and only a part of the NBI fast ions inside a plasma P_{fi} transfer their energy into bulk plasma particles via Coulomb collisions f_{heat} and actually heat the plasma with the power P_{heat}. The NBI power P_{NBI} is a value, which is possible to derive with the below presented power balance analysis.

efficiencies of the power transmission mechanisms illustrated in the figure 6.1 is as follows. Ions are accelerated inside the neutral beam injector by a system of grids. The power carried by accelerated ions P_{ion} is the product of applied acceleration voltage U_{beam} and measured extracted current of fast ions I_{beam}. The extracted ions are neutralized inside the neutralizer with the neutralization efficiency f_{neut} and the total power carried by produced neutrals is P_{tot}. The calculation of P_{tot} using the measured NBI Doppler shifted D_α lines is described in the section 4.2.2. As fast neutrals are injected into the tokamak chamber from neutral beam injector, they have to pass through the narrow port called beam duct, where the beam is partially scraped and the delivered auxiliary heating power P_{AUX} is a fraction of the original P_{tot}. The efficiency of beam passing through the beam duct f_{pass} is derived in the section 4.2.3.

As the fast neutrals enter plasma volume, they collide with plasma particles, which leads to their ionization. However a part of the fast neutrals pass through the plasma without being ionized. This losses are called shine-through. The overall NBI ionization efficiency inside the plasma is represented by f_{ion}. The fast NBI neutrals in the plasma become the fast ions once they are ionized. These fast ions inside the plasma are slowed down by the Coulomb collision and they heat up the plasma P_{heat}. Before the fast ions fully transfer their energy to the bulk plasma particles, they can be lost by various channels such as the charge-exchange collisions with plasma background neutrals or the unfavorable trajectories guiding fast ions into the tokamak wall as described more into the detail in the section 3.3. The NBI power P_{NBI} is a value, which is possible to derive with the below presented power balance and its value is somewhere between P_{fi} and P_{heat}. The difference is explained later on.

Once the NBI is switched on, the fast ions are present in the plasma and they

are transferring their energy into the bulk plasma particles. The fast ions presence and the additional heating power appears as an increase of the total measured stored energy in the plasma. The balance between plasma power sources and sinks is described by the power balance equation (6.1) for a case of the NBI heated discharges,

$$P_{\text{ext}} + P_{\text{NBI}} = P_{\text{sep}} + P_{\text{rad}} + P_{\text{shape}} + P_{\text{cur}} + \frac{\mathrm{d}W}{\mathrm{d}t}\,, \text{substituting} \tag{6.1}$$

$$P_{\text{shape}} = I_{\text{P}} \frac{I_{\text{P}} \mathrm{d}L}{\mathrm{d}t}\,, \tag{6.2}$$

$$P_{\text{cur}} = I_{\text{P}} \frac{L \mathrm{d}I_{\text{P}}}{\mathrm{d}t}\,, \tag{6.3}$$

where P_{ext} represents an external ohmic heating power, consequence of the driven plasma current, P_{NBI} includes NBI additional heating power. The power terms P_{ext} and P_{NBI} are plasma power sources. The power lost from a plasma is described by terms P_{sep}, which is a power lost by particles and heat crossing border of well-confined region (separatrix) in the plasma, and P_{rad}, which is the radiated power. The remaining terms are consequences of changes inside a plasma itself. P_{cur} is a "power used to build up the magnetic field energy by changes of plasma current" and P_{shape} is a "contribution of the plasma shape and current profile changes to the magnetic field energy content" [32]. The powers P_{shape} and P_{cur} depend on a plasma current I_{P} and a plasma inductance L and their time derivatives. The last term of the equation (6.1) is the time derivative of the plasma stored energy W, which is determined by the EFIT reconstruction. The terms P_{ext}, P_{cur} and P_{shape} are based on the magnetic measurements. Thus, for simplification, let's introduce the magnetic power P_{mag}, which will simplify the equation (6.1):

$$P_{\text{mag}} = P_{\text{ext}} - (P_{\text{cur}} + P_{\text{shape}})\,. \tag{6.4}$$

Detailed description of the aforementioned terms of the power balance equation (6.1) and how they are determined for the COMPASS tokamak is given in [64].

All terms of the equation (6.1), excluding P_{NBI} and P_{sep}, are measured on the COMPASS tokamak. An example of their measured time traces is shown in the figure 6.2. To determine the NBI power P_{NBI} it is necessary to eliminate the term P_{sep} in the equation (6.1), which is not measured. To do so, it is assumed that the losses through the separatrix P_{sep} remain unchanged shortly after NBI is switched on. If this assumption is valid, it is possible to derive the power through the separatrix P_{sep} in the discharge stage shortly before NBI is switched on, named as the NBI-off stage, and to use its value for the power balance equation when the NBI is switched on. However, the power through the separatrix P_{sep} starts to modify after a short period when the NBI is ongoing and this assumption is not valid anymore. Therefore the peak value of the P_{NBI} after NBI is switched on corresponds to its real value. NBI-on name stands for this peak value position.

To determine the NBI power as precise as possible, the suitable discharges are selected with the following criteria. First, there has to be at least a short flat-top just before NBI is started, which excludes all time derivatives in the power balance equation for the NBI-off stage and allows to use time averaged terms. Second, the experiments where other transients, such as L-H transition, were ongoing simultaneously with the NBI start or the H-mode discharges are excluded. In

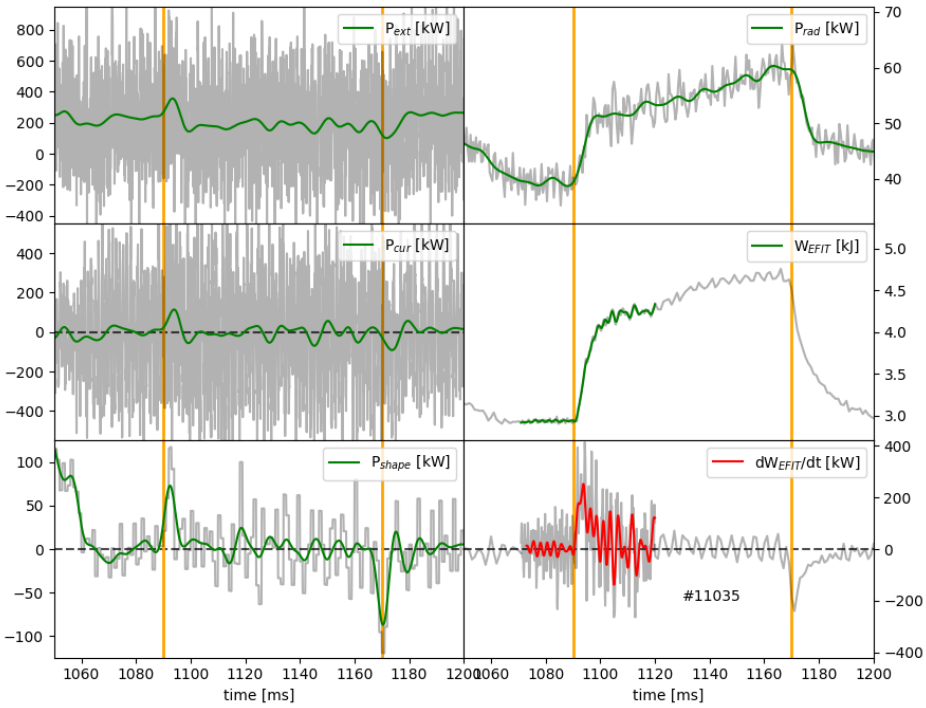

Figure 6.2: Measured terms of the equation (6.1) are shown by grey and green lines (with applied low-pass filters), determined $\mathrm{d}W_{\mathrm{EFIT}}/\mathrm{d}t$ employing low-pass Butterworth filter is shown by the red line and vertical orange lines represent NBI start and stop for the discharge #11035.

case of such discharges, it would not be possible to distinguish an impact of the NBI heating from the transition phenomena or H-mode modification. Thanks to the additional discharges restrictions and mentioned assumptions, the NBI power P_{NBI} determination simplifies into the following equation (6.5).

$$P_{\mathrm{NBI}} = \left(P_{\mathrm{rad}} + \frac{\mathrm{d}W_{\mathrm{EFIT}}}{\mathrm{d}t} - P_{\mathrm{mag}} \right)_{\mathrm{NBI-on}} - \left(P_{\mathrm{rad}} - P_{\mathrm{mag}} \right)_{\mathrm{NBI-off}} \tag{6.5}$$

The term $\mathrm{d}W_{\mathrm{EFIT}}/\mathrm{d}t$ for NBI-on stage is a dominant term, as can be seen in the figure 6.2. The EFIT energy is based on the total kinetic plasma pressure, the pressure of all charged particles inside the separatrix of the plasma, including fast ions. Since the power through the separatrix P_{sep} is derived before NBI is switched on, it does not cover the instantaneous NBI losses, such as shine through or fast orbit and charge-exchange ions losses. Therefore, the determined NBI power P_{NBI} by the suggested method is not the auxiliary heating power of the injected neutrals P_{AUX}, but it is a power of the NBI fast ions, which are confined inside the plasma. In comparison with the other NBI power terms in the figure 6.1, the derived NBI power from the power balance P_{NBI} is lower than the power of all ionized fast neutrals inside the plasma P_{fi} because the fast orbit and charge-exchange ions losses are included and simultaneously it is higher than the heating power transferred into the bulk plasma P_{heat} because the additional losses, which occur during fast ions slowing down, are not included in P_{NBI}.

The sawtooth oscillations are often visible on the EFIT energy W_{EFIT} for the examined discharges. The oscillation of the EFIT energy W_{EFIT} leads to enormous

noise of the time derivative $\mathrm{d}W_{\mathrm{EFIT}}/\mathrm{d}t$ as seen in the figure 6.2. Therefore, the signal has to be filtered to improve the output quality. As the peak value of the EFIT energy time derivative, after NBI is switched on, is detected in the time range comparable with the sawtooth oscillations period, the filtering of the EFIT energy W_{EFIT} is not trivial and it is discussed more in the following section.

6.1.1 Power balance data processing

The EFIT energy W_{EFIT} noise consists of a random noise and a periodic variation, which is a consequence of the so-called sawtooth instability introduced in the section 3.5.1. The sawtooth period, which varies in a range $\sim$ 1–4 ms, is comparable with a characteristic time of the $\mathrm{d}W_{\mathrm{EFIT}}/\mathrm{d}t$ when the NBI is switched on. The dependence of a ratio of the plasma energy variations σW_{EFIT} for the NBI-off stage, shortly before NBI is switched on, and the total plasma energy increases caused by the NBI heating ΔW_{EFIT} on the sawtooth frequency T_{saw} derived for the NBI-off discharge stage is shown in the figure 6.3.

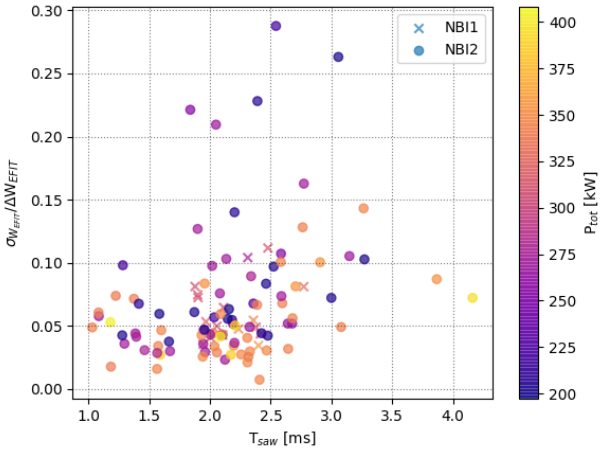

Figure 6.3: A dependence of a ratio of the signal variation σW_{EFIT} caused by the sawtooth oscillations and a random signal noise for the NBI-off discharge stage and the total plasma energy increase caused by NBI ΔW_{EFIT} on the sawtooth period T_{saw} during NBI-off stage. The color corresponds to the total NBI power P_{tot}.

The comparable time scale of the sawtooth period and analyzed phenomena makes data analysis nontrivial. Therefore it is needed to make an error analysis of the possible filters on the testing data set. It is needed to suppress the sawtooth in the W_{EFIT} and simultaneously eliminate an impact of the data filtering on the W_{EFIT} grow caused by the NBI heating.

Two possible filters are considered: low-pass Butterworth filter [65] and Savitzky-Golay filter [66]. The main advantage of the Butterworth filter is its flat frequency response. On the other hand, the Savitzky-Golay filter has low peak degradation, i.e. it can filter-out small signal variation and simultaneously keep more significant fast signal changes. The Savitzky-Golay filter parameters are a number of the considered data-points, so-called filter window width, and the polynomial order. The filter window width is varied and the polynomial order is set to 3, which allows to use a window width ranging from 3. The low-pass

Butterworth filter parameters are a filtration frequency, which is varied, and an order of the filter, which is set to 20. The higher the filter order is the steeper the signal drop at the filtering frequency is.

As it is mentioned above, the sawtooth period is comparable with the time characteristic time of the $\mathrm{d}W_{\mathrm{EFIT}}/\mathrm{d}t$. Therefore the applied filtering method can easily lead to additional systematic error of determined quantities. This possible systematic errors has to be investigated. Here, the testing signals, similar to W_{EFIT}, with well known parameters are employed. The testing signals consist of original function g, the sawtooth wave with period T_{saw} and different phase shifts in respect to the ramp starts, and an additional random noise. The original function g with known maximum of the time derivative $\max(\mathrm{d}g/\mathrm{d}t)$, named as the peak height h_{peak} in the following text, time position of this maximum Δt_{max}, named a peak time shift, and total increase Δg represents unnoise EFIT energy signal. Examples of the testing signals including the noise and the original function time gradients are shown in the figure 6.4.

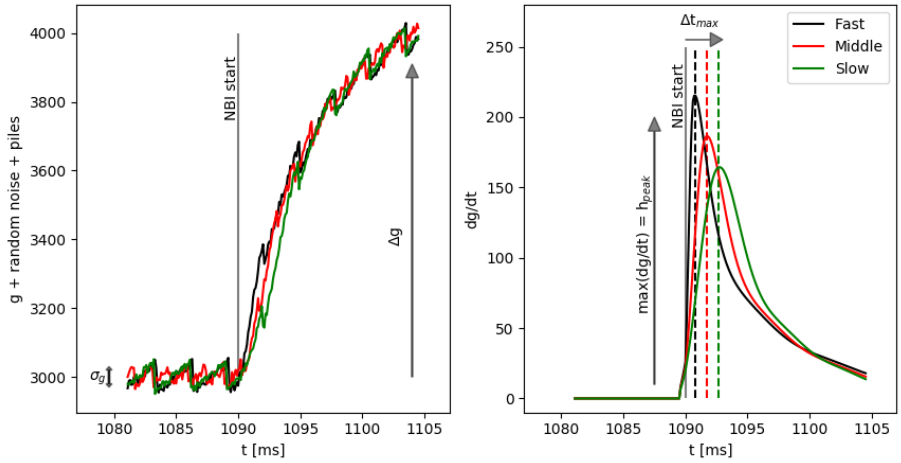

Figure 6.4: Testing function g with a random noise and a sawtooth wave (left) and its original time gradients (right). The arrow in the left part illustrates a total increase of the function g, Δg. The vertical arrow in the right represents a desired maximum gradient value $\max\left(\mathrm{d}g/\mathrm{d}t\right)$, named as the peak height h_{peak}, and Δt_{max} is its position with respect to the NBI start, named a peak time shift, shown by the horizontal arrow on the right. The peak time shift Δt_{max} is a variable parameter of the testing functions in range 1–3.5 ms and the function is normalized in the way that the total increases of the testing function Δg remain same. The testing functions are referred as *Fast* (black), *Middle* (red) and *Slow* (green).

The testing function, including all considered noises, is analyzed by the low-pass Butterworth frequency filter and by the Savitzky-Golay filter and resulting peak height h_{peak} and the peak time shift Δt_{max} are compared with the known values of the original testing functions g. The results for the low-pass Butterworth frequency filter are shown in the figure 6.5 and the results for the Savitzky-Golay filter are shown in the figure 6.6.

The ratio of the detected and the original gradient peak height h_{peak} is sensitive to the peak time shift Δt_{max} of the original function g, i.e. if the Slow, the Middle

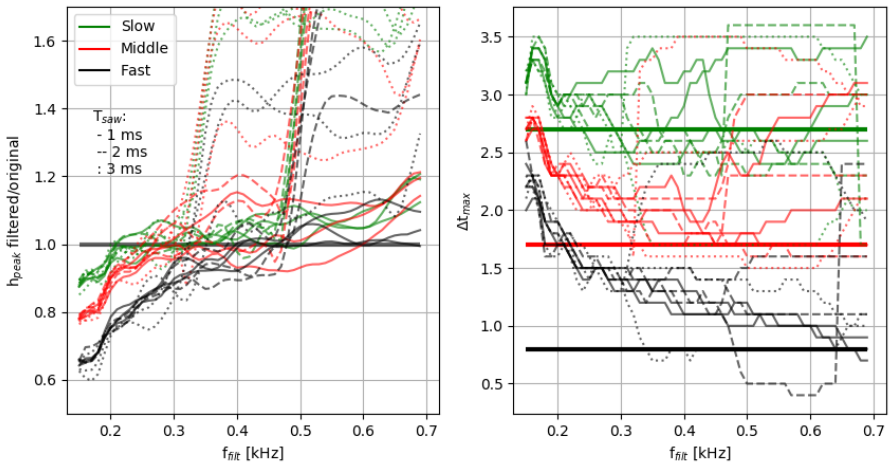

Figure 6.5: Low-pass Butterworth frequency filter: The ratio of the original and detected peak height h_{peak} (left) and the peak time shift from the testing function grow start g Δt_{max} (right) as a function of the low-pass filtering frequency. The horizontal lines on the right stand for the values of the original testing functions. Each color corresponds to the original testing function in figure 6.4, different line styles represent various saw period (solid: 1 ms, dashed: 2 ms, dotted: 3 ms). The lines with the same color and line style are calculated for the different phase shift of the sawtooth waves.

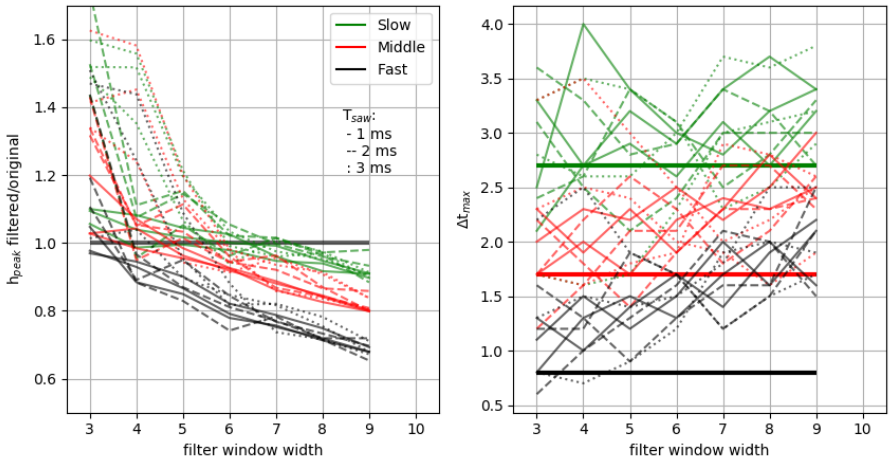

Figure 6.6: Savitzky-Golay filter: TThe ratio of the original and detected peak height h_{peak} (left) and the peak time shift from the testing function grow start g Δt_{max} (right) as a function of the filtering window width. The horizontal lines in the right represent the values of the original testing functions. Each color corresponds to the original testing function in figure 6.4, different line styles stand for various saw period (solid: 1 ms, dashed: 2 ms, dotted: 3 ms). The lines with the same color and line style are calculated for the different phase shift of the sawtooth waves.

or the Fast testing function g is considered, for both examined filtering methods. As the peak time shift Δt_{max} is hard to detect with necessary precision, the chosen filtering method should have same results, independent on the chosen testing function. This is not fulfilled for the low-frequency in case of the low-pass

Butterworth filter or wide window filtering in case of the Savitzky-Golay filter where the ratio of the detected and the original gradient peak height h_{peak} is well defined, but it differs for the different testing functions g. Therefore a target is to find the filtering method with the ratio of the detected and the original gradient peak height h_{peak} close to unity. Simultaneously, it should fulfil a low spread given by the sawtooth wave phase shift, which is expected to be random, and the chosen filtering method should give similar results independently on the peak time shift Δt_{max}, i.e. similar for the Fast, Middle and Slow testing function g. The best window length in case of the Savitzky-Golay filter from this point of view is 4, where the most of the lines are in the range of ~ 0.9–1.1 excluding the sawtooth waves with the longest period, as seen in the left panel of the figure 6.6. The filter window 3 is sufficient for the shortest sawtooth waves. The low-pass Butterworth frequency filter fulfill these conditions for filtering frequency $f_{\mathrm{filt}} \sim 0.45\,\mathrm{kHz}$, excluding the longest sawteeth period as well, as seen in the left panel of the figure 6.5.

To analyze the possible derived outputs by two different methods more into detail, the ratio of the detected and the original gradient peak height h_{peak} is determined for a range of the sawtooth period T_{saw} from 1 ms up to 4 ms and also various sawtooth wave amplitude and relative noise magnitude $\sigma g/\Delta g$ in respect to the total grow of the testing function g. To eliminate issues with the sawtooth wave with the long period the applied filtering algorithms are following:

- Low-pass Butterworth frequency filter:

$$f_{\mathrm{filt}} = \begin{cases} 0.45\,\mathrm{kHz} & \text{if } 92.5\%\, T_{\mathrm{saw}}^{-1} \leq 0.45\,\mathrm{kHz}, \\ 92.5\%\, T_{\mathrm{saw}}^{-1} & \text{otherwise}\,. \end{cases} \tag{6.6}$$

- Savitzky-Golay filter:

$$\text{filter window width} = \begin{cases} 3 & \text{if } T_{\mathrm{saw}} \leq 1.5\,\mathrm{ms}, \\ 4 & \text{otherwise}\,. \end{cases} \tag{6.7}$$

Following figures, the figure 6.7 and the figure 6.8, show the ratio of the detected and the original gradient peak height h_{peak} and its standard deviations, which are derived by varying the sawtooth phase shifts, for all three testing functions g.

The Savitzky-Golay filter exhibits the sufficiently low deviation from the original gradient peaks height h_{peak} only for a small sector of the pre-selected discharges to process, which are represented by the markers. If the discharges with the parameters outside the coloured area in the upper row in the figure 6.8 are processed by the Savitzky-Golay filter the detected peak values are overestimated by more than 15 %.

On the other hand, the filter analysis shows that the low-pass Butterworth frequency filter application as described above leads to the deviation from the original gradient peak height h_{peak} below 5 % for most of the pre-selected discharges. Only in the case of the Fast testing function g with long sawtooth period T_{saw} and Slow testing function g with high noise level of the testing function $\sigma g/\Delta g$, the derived values of the gradient peak height h_{peak} deviate by 10

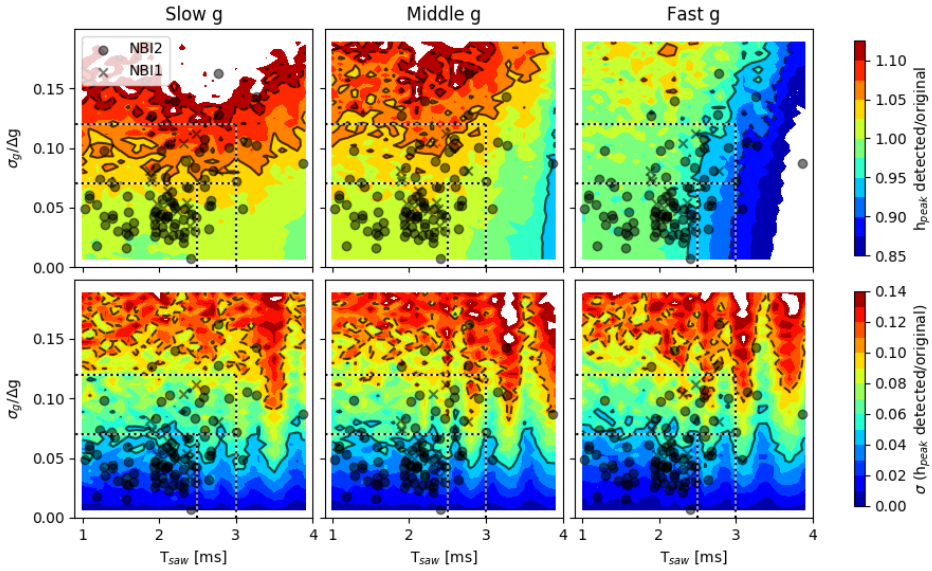

Figure 6.7: The low-pass Butterworth frequency filter analysis. The graphs are paired in columns. The horizontal axes are the sawtooth periods T_{saw} and the vertical axes are the relative noise magnitudes $\sigma g/\Delta g$ of the testing function g. The ratios of the detected and original gradient peak height h_{peak} are in the upper row and their standard deviations derived from signals with different sawtooth phase shifts are shown in the bottom row. The left pair uses the Slow testing function g, the middle row uses the Middle testing function g and the right one uses the Fast testing function g. The markers are the same as in the figure 6.3 and they represent parameters of the pre-selected discharges for the power balance analysis. The solid and dashed lines highlight areas with the deviation up to 5 % and 10 % from original original gradient peak height h_{peak} respectively.

%. The standard deviation of the ration of the detected and original gradient peak heigh h_{peak} is below 5 % if the noise level of the testing function $\sigma g/\Delta g$ is less than 0.07. Therefore the low-pass Butterworth frequency is selected as the filter for the EFIT energy W_{EFIT} data processing. The simplified selection of the total error of the detected gradient peak heigh h_{peak} used for the EFIT energy W_{EFIT} analysis is summed up in the table 6.1. The discharges with the sawtooth periods T_{saw} longer than 3 ms or with the noise level $\sigma g/\Delta g$ higher than 0.12 are excluded from the analysis.

$\sigma g/\Delta g$	< 0.07	> 0.07
$T_{\mathrm{saw}} < 2.5$ ms	10%	15%
$T_{\mathrm{saw}} > 2.5$ ms	15%	20%

Table 6.1: Overview of the requested W_{EFIT} signal parameters for NBI L-modes characterization.

Summarizing the analysis with two different filtering methods applied on the testing signals, the low-pass Butterworth frequency filter is chosen as the more suitable one. The filtering frequency equals to 0.45 kHz, if the sawtooth frequency is higher than 92.5 % of 0.45 kHz, i.e. the sawtooth period is lower than 2.4 ms, otherwise the 92. % of the sawtooth frequency is used. The algorithm of the

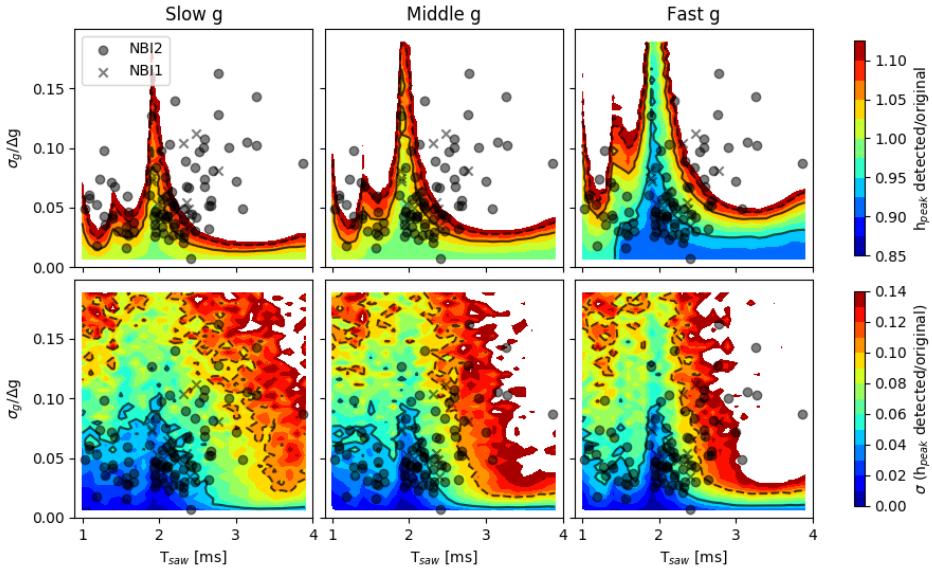

Figure 6.8: Savitzky-Golay filter analysis. The graphs are paired in columns. The graphs are paired in columns. The horizontal axes are the sawtooth periods T_{saw} and the vertical axes are the relative noise magnitudes $\sigma g/\Delta g$ of the testing function g. The ratios of the detected and original gradient peak height h_{peak} are in the upper row and their standard deviations derived from signals with different sawtooth phase shifts are shown in the bottom row. The left pair uses the Slow testing function g, the middle row uses the Middle testing function g and the right one uses the Fast testing function g. The markers are the same as in the figure 6.3 and they represent parameters of the pre-selected discharges for the power balance analysis. The solid and dashed lines highlight areas with the deviation up to 5 % and 10 % from original original gradient peak height h_{peak} respectively. The white areas are out of the selected range of the color scales.

filtering frequency selection is summed up in the equation (6.6). The EFIT data are suitable for the data analysis only if the sawtooth period is lower than 3 ms and if the total relative noise level $\sigma g/\Delta g$ of the EFIT energy W_{EFIT} before NBI start is lower than 0.12. The last condition is that the peak time shift from the NBI start Δt_{max} of the EFIT energy W_{EFIT} has to be in the range of the testing functions. This is examined by the EFIT energy filtering with the low-pass Butterworth filter with the low filtering frequency < 0.3 kHz, where the detected peak time shift Δt_{max} varies a little with the sawtooth phase and the sawtooth period, seen on the testing functions in the figure 6.5. The peak time shift Δt_{max} variation with the low filtering frequency for the measured EFIT energy W_{EFIT} of the pre-selected discharges is compared with the testing functions values in the figure 6.9.

Most of the EFIT peak time shifts Δt_{max} are in the range of the testing signals, as seen in the figure 6.9. The discharges, which are below the fast testing function, are excluded from the power balance analysis.

The remaining terms in the equation (6.5), P_{mag} and P_{rad}, should be determined in the same time of discharge as the gradient peak value $\mathrm{d}W_{\mathrm{EFIT}}/\mathrm{d}t$. The origin peak time shift Δt_{max} has apparent values for different filtering frequencies, as seen in the figure 6.5. Therefore it is necessary to find out the additional

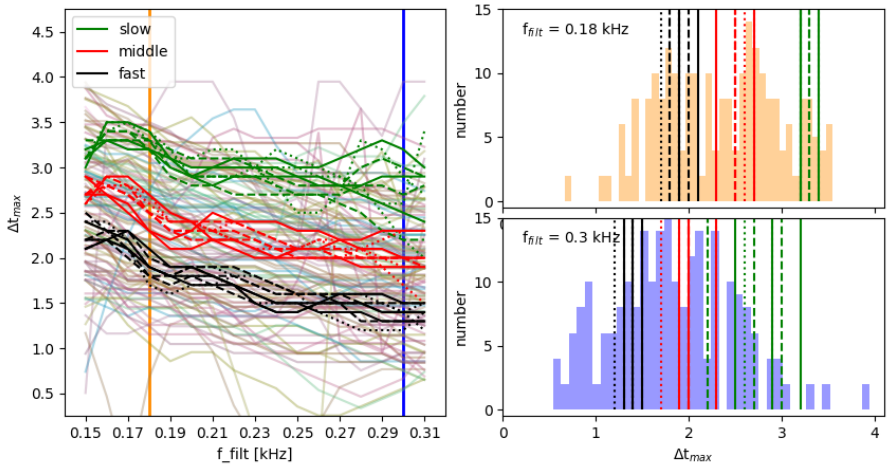

Figure 6.9: The peak time shift $\Delta t_{\max}$ of the pre-selected discharges (left, bright solid lines) and of the testing signals (green, red, black lines, same as in the figure 6.5) as a function of the applied low-pass Butterworth frequency and corresponding histograms of the peak time shift $\Delta t_{\max}$ for two different filtering frequencies 0.18 kHz and 0.3 kHz (right). A majority of the apparent peak time shift $\Delta t_{\max}$ of the measured EFIT energy for the pre-selected discharges are in the range of the used testing signals.

time shift, which is done as follows. Firstly the apparent peak time shift $\Delta t_{\max}$ is examined for the testing functions and based on its behaviour the process how to determine the additional time shift of the peak time shift $\Delta t_{\max}$ for the measured EFIT energies is defined. The figure 6.10 shows a dependence of the apparent peak time shift $\Delta t_{\max}$ for the testing functions g and corresponding uncertainties while different filtering frequencies, 0.2 kHz, 0.25 kHz and 0.3 kHz, are applied.

As the apparent peak time shift $\Delta t_{\max}$ is directly proportional to its original values the reverse proportionality is applied to determine the original value from the apparent one when the measured data are processed. The original value of the peak time shift $\Delta t_{\max}$ is determined from three apparent values of the peak time shift $\Delta t_{\max}$, which are derived with the different filtering frequencies, 0.2 kHz, 0.25 kHz and 0.3 kHz. The NBI-on values of the magnetic power P_{mag} and the radiated power P_{rad} are derived in the time of the determined original peak time shift from the NBI start $\Delta t_{\max}$ with expected uncertainty of the original peak time shift $\Delta t_{\max}$, the black dashed line in the left part of the figure 6.10. The NBI-off values of the magnetic power P_{mag} and the radiated power P_{rad} are evaluated as mean values in the time range 1–5 ms before NBI is switched on. An example of the origin peak time shift $\Delta t_{\max}$ and time traces of the magnetic power P_{mag} and the radiated power P_{rad} close to the NBI start are shown in the figure 6.11.

Because we need the additional filtering of the P_{mag} and P_{rad}, as is shown in the figure 6.11, and simultaneously their NBI-on values are derived in the time range of the peak time shift $\Delta t_{\max}$ uncertainty, the additional error to the P_{NBI} is estimated to be $\sim$ 20 kW.

To conclude this subsection, based on the analysis of the testing signals, the low-pass Butterworth frequency filter is selected for the EFIT energy gradient analysis. The selection of the filtering frequency is described in the equation

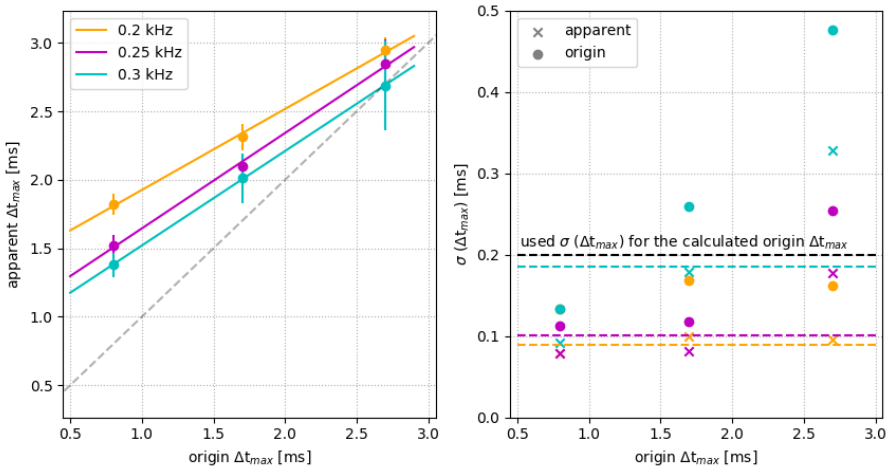

Figure 6.10: Origin and apparent peak time shift $\Delta t_{\max}$ derived from testing functions g for three different low-pass filtering frequencies (left) and the corresponding uncertainties $\sigma(\Delta t_{\max})$ for the apparent $\Delta t_{\max}$ and for the original $\Delta t_{\max}$ if the original would be derived from the apparent values based on their linear dependence (right) employing the reverse proportionality from the left panel. The apparent peak time shift $\Delta t_{\max}$ uncertainties are derived from the testing functions with different sawtooth phases shifts and periods. The colored dashed lines in the right correspond to the average σ values of the origin peak time shift $\Delta t_{\max}$. The black dashed line is used as the time range for determination if the NBI-on values of the magnetic power P_{mag} and the radiated power P_{rad}.

(6.6). The analyzed discharges has to fulfill following conditions:

- Sawtooth period T_{saw} just before the NBI start has to be lower than 3 ms.
- The standard deviation of the total noise signal before the NBI start, where it would be constant in the ideal case, has to be lower than 12 % of the total EFIT energy increase caused by the additional NBI heating.
- The time shift of the EFIT energy gradient maximum in respect to the NBI start derived from filtered signal $\Delta t_{\max}$, called peak time shift, should fit into the range of this quantity for the testing functions, as shown in the figure 6.9.

The total error of derived P_{NBI} consists from the errors presented in the table 6.1, which comes from $\mathrm{d}W_{\text{EFIT}}/\mathrm{d}t$, and an additional 20 kW, which is the consequence of the determination of the magnetic power P_{mag} and the radiated power P_{rad}.

6.1.2 Power balance results

The delivered NBI heating power into the plasma P_{NBI}, derived with the equation (6.5) based on the power balance equation (6.1), depends on the beam losses before the fast neutrals enter the tokamak chamber itself and also on the losses inside a plasma, introduced in the section 3.3, which depend on plasma parameters. Therefore, the NBI heating power P_{NBI} dependencies on various parameters are discussed in this section.

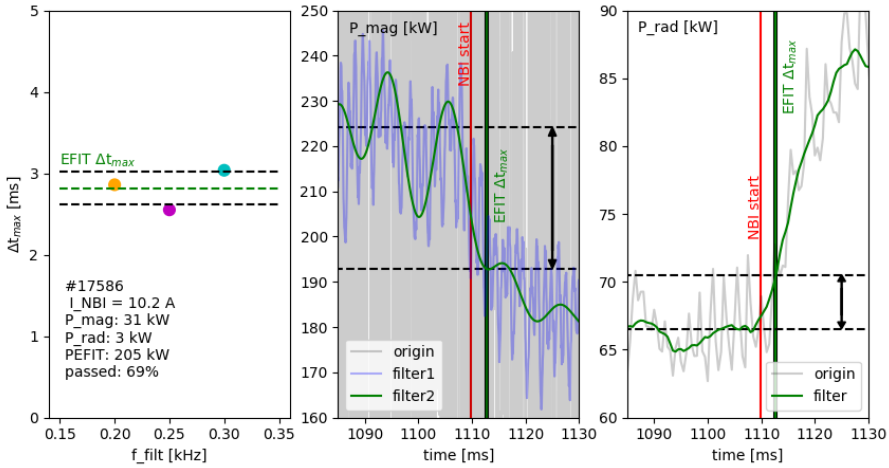

Figure 6.11: Derived origin peak time shift $\Delta t_{\max}$ for the EFIT plasma energy with three different filtering frequencies (left), the magnetic power time trace P_{mag} (middle) and the radiation time trace P_{rad} (right) around the NBI start. The red line highlight the NBI start, the green lines correspond the origin peak time shift $\Delta t_{\max}$ and its range is represented by black lines. As the magnetic power P_{mag} (middle) and the radiated power P_{rad} are noisy, they are filtered and the NBI-off/-on differences, highlighted by arrows, are derived from these filtered values. P_{mag} is filtered by the low-pass Butterworth filter with filtering frequency 0.1 kHz and P_{rad} is filtered by Savitzky-Golay with the 3$^{\text{rd}}$ polynomial order and window width = 15.

Impact of the initial beam duct conditions

The neutral beam is passing through the narrow beam duct before it enters the COMPASS tokamak chamber. The NBI scraping losses in the beam duct are discussed in the section 4.2.3. Excluding NBI scraping losses, there can be additional losses of the NBI power inside the beam duct, when the beam duct surfaces are in the poor condition regarding the dust and sorbed gas. This is recognized in the evolution of the delivered NBI power P_{NBI} for a few subsequent NBI1 discharges with same plasma parameters and NBI settings shown in the figure 6.12. These discharges were performed after a longer period without the use of NBI. The enhancement of the delivered NBI power P_{NBI} after the first NBI shot is clearly visible.

Each opening of the tokamak vessel requires subsequent conditioning of the inner surface, which is subjected to atmospheric pressure during this time. Adsorbed gasses along with dust particles are released via heating the metallic walls including connection ports in a process called *baking*. Afterwards, the tokamak itself undergoes one or more days of a so-called *restart*. The restart is a series of standard discharges, which lead to the release of the dust and remaining gas absorbed inside the tokamak first wall. The similar process, performing of a few initialization NBI shoots, is requested for the beam duct. The NBI fast neutrals heat up the beam duct surfaces and realise the sorbed gas and dust particles. The abnormal residual gas density inside the beam duct within this process leads to the additional beam attenuation before reaching a tokamak chamber. This effect is only temporal and it vanishes after a few discharges. It seems, that in

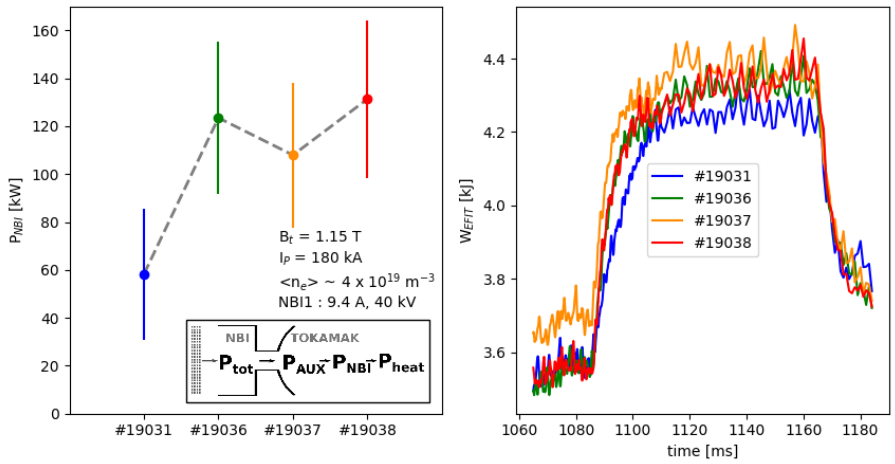

Figure 6.12: Detected NBI heating power P_{NBI} (left) and plasma stored energy W_{EFIT} (right) for the consequent discharges after a longer period without NBI use. All discharges were realized with same plasmas and NBI1 settings. The slower increase of the W_{EFIT} in case of the discharge #19031 leads to the lower detected P_{NBI}.

the presented case one discharge was sufficient, as the following discharges have already comparable EFIT plasma energy W_{EFIT} increase and derived NBI power P_{NBI}.

Impact of the NBI scraping, the initial NBI power and the plasma density

Another effect, that lowers the delivered NBI power into the tokamak chamber, caused by the beam duct is the scraping of the beam as it passes through. Here, the NBI powers P_{NBI} derived by the power balance analysis of L-mode discharges, heated by NBI2, from the Basic Co-current, the Shape Co-current scans defined in the table 5.1 are studied. Additionally, the NBI powers P_{NBI} delivered by NBI1 into plasmas with similar plasma parameters, as the discharges performed in the NBI2 scans, are presented. The measurement results are compared with the available outputs of the simulations, introduced in the table 5.3.

First, the dependence of the NBI power P_{NBI} on the total produced NBI power P_{tot} carried by the fast neutrals is investigated. The left panel of the figure 6.13 shows dependence of the ratio of the NBI heating power and the total produced NBI power $P_{\mathrm{NBI}}/P_{\mathrm{tot}}$ on the total produced NBI power P_{tot}. The right panel of the figure 6.13 shows the ratio of $P_{\mathrm{NBI}}/P_{\mathrm{tot}}$ from the left panel (coloured markers) divided by the determined passing fraction $f_{\mathrm{pass}} = P_{\mathrm{AUX}}/P_{\mathrm{tot}}$ (dashed line) from the section 4.2.3. The ratio is actually $P_{\mathrm{NBI}}/P_{\mathrm{AUX}}$, which is a fraction of the NBI power and the power carried by the NBI neutrals, which enter the tokamak chamber.

The fraction of NBI power $P_{\mathrm{NBI}}/P_{\mathrm{tot}}$ detected in the plasma by the power balance is increasing with the total NBI power P_{tot}, similarly as the total heating power passing through the narrow NBI duct $P_{\mathrm{AUX}}/P_{\mathrm{tot}}$ derived in the subsection 4.2.3. This is a confirmation, that there are additional NBI power losses caused by the scraping inside the beam duct and that the predicted passing fraction

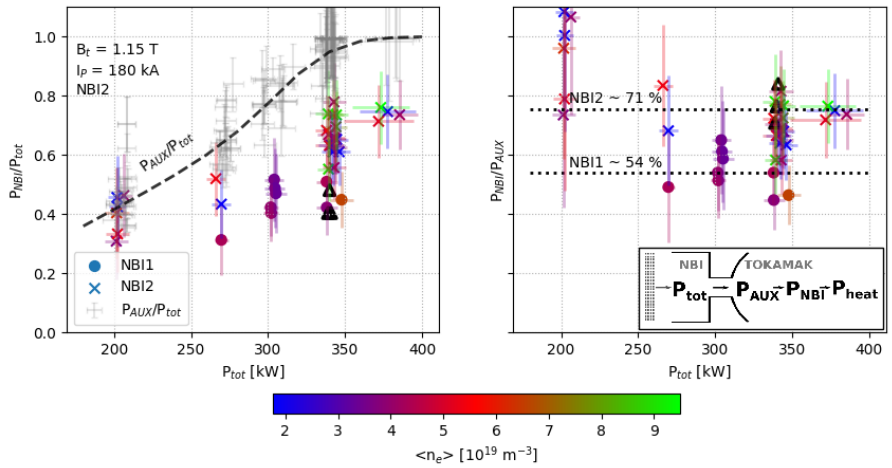

Figure 6.13: Ratios of the additional heating power identified inside the plasma and the total power held by formed NBI fast neutrals $P_{\mathrm{NBI}}/P_{\mathrm{tot}}$ are depicted by dots (NBI1) and crosses (NBI2) with predicted passing fraction through the narrow beam duct $P_{\mathrm{AUX}}/P_{\mathrm{tot}}$ (the figure 6.13) in the left part (grey crosses and dashed line). The ratio of coloured markers with the predicted dashed line is shown in the right, which should correspond to a ratio $P_{\mathrm{NBI}}/P_{\mathrm{AUX}}$. Hollow triangles represents results of the METIS simulations, but actually for $P_{\mathrm{heat}}/P_{\mathrm{tot}}$ (left) and $P_{\mathrm{heat}}/P_{\mathrm{AUX}}$ (right). The markers are coloured in scale of a plasma line-averaged density $\langle n_{\mathrm{e}} \rangle$.

$f_{\mathrm{pass}} = P_{\mathrm{AUX}}/P_{\mathrm{tot}}$ in the equation (4.11) is in agreement with the independent power balance results. Moreover, $P_{\mathrm{NBI}}/P_{\mathrm{AUX}}$ is almost constant with the total produced NBI power P_{tot} within error bars for each NBI injector. It seems that the losses caused by the scraping inside the beam duct are slightly overestimated in the lowest P_{tot} case, ~ 200 kW.

The power delivered into a plasma from NBI1 is systematically lower than for NBI2. There can be different causes of this behaviour, for example different beamlet divergences, slight misalignment of the NBI1 or imprecise beam focusing. Therefore, the auxiliary heating power P_{AUX} for NBI1 is determined for the following sections from the calculated passing fraction through a beam duct for NBI2 (dashed line in the figure 6.13) and it is reduced by an additional $71 - 54 = 17\,\%$ of the total neutral power P_{tot}.

The figure 6.14 shows a dependence on the plasma line-averaged density $\langle n_{\mathrm{e}} \rangle$ of the ratios of the derived NBI power P_{NBI} and the total produced NBI power P_{tot} and the NBI auxiliary power P_{AUX} respectively.

It seems that there is no strong dependence of the ratio of the NBI power derived by the power balance and the auxiliary heating power entering the tokamak chamber $P_{\mathrm{NBI}}/P_{\mathrm{AUX}}$ on the plasma line-averaged density $\langle n_{\mathrm{e}} \rangle$. This means, that there are no significant shine-through losses at the lowest densities of the studied range.

Before the simulation results are compared with the power balance results, it is necessary to stress that the power balance provides information about slightly different quantity than the simulations. The NBI neutrals entering the tokamak chamber deliver the auxiliary heating power P_{AUX}. Part of this power is lost via

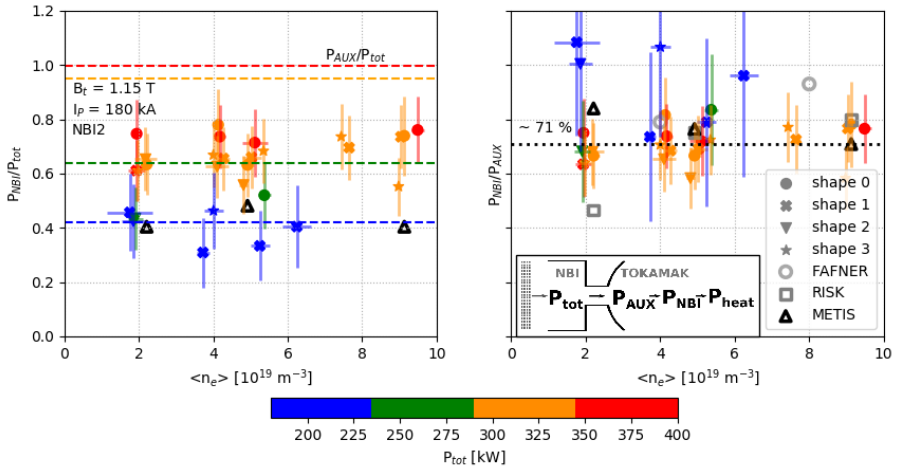

Figure 6.14: Plasma line-averaged density $\langle n_\mathrm{e} \rangle$ dependence of a portion of the derived NBI power in respect to the total power in produced neutrals $P_\mathrm{NBI}/P_\mathrm{tot}$ with corresponding expected passing fraction $P_\mathrm{AUX}/P_\mathrm{tot}$ as derived in the figure 6.13 is shown in the left part. Dependence of derived $P_\mathrm{NBI}/P_\mathrm{AUX}$ on plasma density n_e (coloured markers) is compared in the right part with various simulations results (hollow markers) introduced in the table 5.3, which more precisely stand for $P_\mathrm{heat}/P_\mathrm{AUX}$. Colours corresponds to the total NBI power P_tot.

the shine-through losses and the power in all ionized NBI neutrals is P_fi. Part of these fast ions is lost almost immediately via the first orbit losses and the charge-exchange losses. The remaining fast ions can heat up the plasma. However, there are still some fast ions losses ongoing during the process of the energy transfer between the fast ions and the bulk plasma particles. The successfully transferred power into the bulk plasma ions is the NBI heating power P_heat. Therefore the lost power from the fast ions power P_fi, that is not transferred into the bulk plasma consists from the fast ions losses, which occurs almost immediately after the NBI neutrals are ionized, and from the fast ions losses, which occurs later on, during the slowing down time process.

The NBI power P_NBI, which is a result of the power balance analysis, is derived in the time shortly after the NBI is switched on $\sim$ 1–3 ms. Therefore the derived power from the power balance P_NBI differs from the all fast ions power P_fi only by the almost immediate fast ions losses, but it still includes the power, which is lost later-on during the fast ions slowing down. Contrary, the simulations provides the power, which heats up the plasma P_heat. Therefore the difference between the power derived with the power balance analysis P_NBI and the NBI heating power P_heat, provided by simulations, is the power lost during the fast ions slowing down. However, as can be seen in the figure 6.13, right part, the values of $P_\mathrm{NBI}/P_\mathrm{AUX}$ and $P_\mathrm{heat}/P_\mathrm{AUX}$ for METIS simulations are comparable. This means that most of the fast ions losses occur via the almost immediate loss channels and that the power derived from the power balance P_NBI is almost the same as the NBI heating power P_heat.

A plasma density dependence of fractions of the NBI power derived by the power balance P_NBI and the total power of the NBI produced neutrals P_tot or the auxilliary heating power P_AUX in the figure 6.14 seems to be weak, if any.

The simulation predictions of the fraction of the transferred heating power from the auxiliary heating power $P_{\mathrm{heat}}/P_{\mathrm{AUX}}$ are unclear as RISK expects more significant losses for the lowest densities $\sim 2 \times 10^{19}$ m^{-3}, METIS exhibits slight power absorption improvement for the lowest densities and FAFNER indicates enhancement of the power absorption with an increasing plasma density.

Impact of the plasma shape and size

Figures 6.13, 6.14 show results of discharges from the Shape scan defined in the table 5.1 for the various plasma shapes and sizes, which are depicted in the figure 5.1. The lack of the dependence of the NBI power P_{NBI} on the plasma shapes from the figure 5.1 is seen also in the figure 6.15.

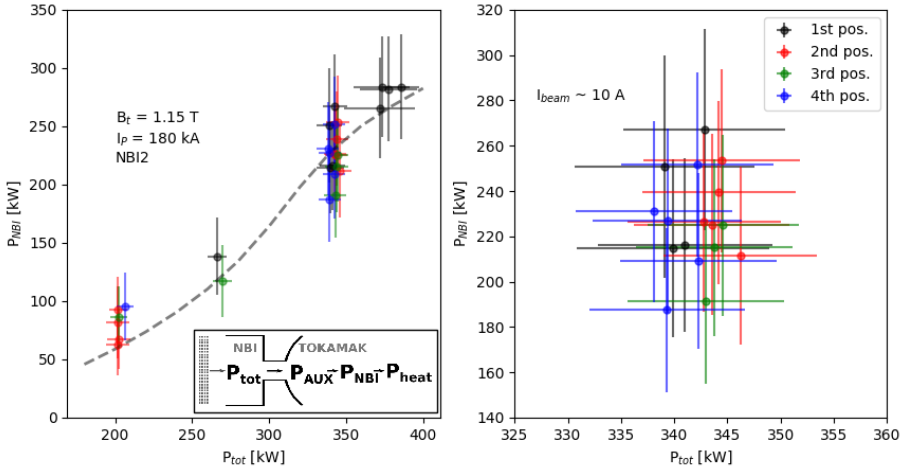

Figure 6.15: The detected NBI power P_{NBI} for different plasma shapes and sizes as a function of the total NBI produced power P_{tot} with the predicted values, based on the figure 6.13 and depicted by a dashed line, (left) and the close-up on the power $\sim$ 350 kW (right). It seems there is no significant difference caused by various plasma shapes and sizes.

Difference between co- and counter-injection

The NBI power orbit losses can significantly increase in case of the NBI counter-injection due to the different co- and counter-passing vertical drift consequences on the particles guiding center motion, as illustrated in the figure 3.4 and discussed in the section 3.3. The effect of the different fast ions orbit losses is important when the fast ions are formed at the low field side, close to the plasma edge. Therefore, as the NBI fast neutrals are more likely being ionized closer to the plasma edge at the low field side for higher or extremely low plasma densities n_{e}, we can expect more significant dependence on the plasma density for the counter-injection than in case of the co-injection.

The co- and counter- NBI injections are realized by a reversal of the plasma current I_{p} on the COMPASS tokamak. The comparison of the Co-current and Counter-current NBI2 heated Basic scans, defined in the table 5.1, and FAFNER simulations is presented in the figure 6.16.

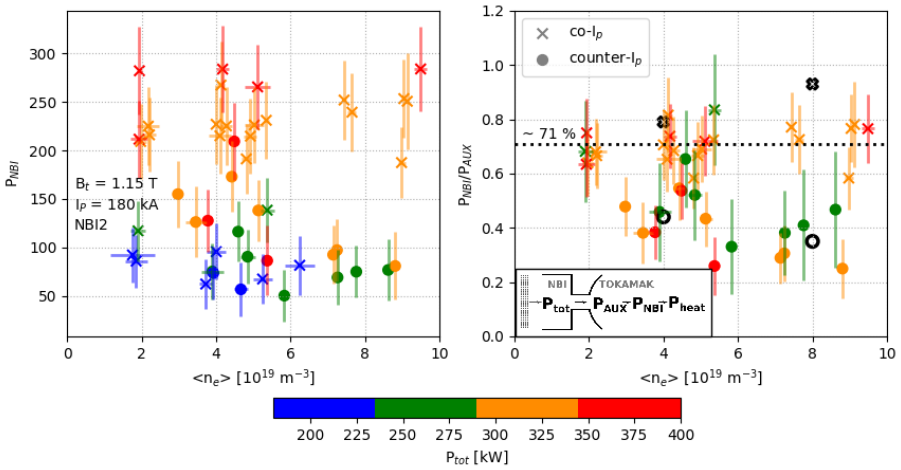

Figure 6.16: The NBI power P_{NBI} derived by the power balance as a function of the plasma line-averaged density $\langle n_{\mathrm{e}} \rangle$ for co- and counter-injection (left) and its relative value in respect to the auxiliary heating power P_{AUX} (right) for measured data (coloured markers) and FAFNER simulations representing $P_{\mathrm{heat}}/P_{\mathrm{AUX}}$ (hollow markers). There is a range of the plasma line-averaged densities $\langle n_{\mathrm{e}} \rangle$ with the enhanced power absorption $P_{\mathrm{NBI}}/P_{\mathrm{AUX}}$ for the counter-injection.

The counter-injection has $\sim$ 30 % higher NBI power losses than otherwise identical discharges with co-injection. This behaviour is also indicated by the FAFNER simulations, which provide information about the NBI heating power P_{heat}. The simulations predict opposite trends with the plasma line-averaged density $\langle n_{\mathrm{e}} \rangle$ for co- and counter-injection. However, this is not clearly confirmed by the power balance results, as the expected changes are in the range of the measurements error-bars.

But, it seems there is an optimal plasma line-averaged density $\sim$ 4–5 $\times$ $10^{19}\,\mathrm{m}^{-3}$ for counter-injection, where the absorbed power ratio is systematically higher. This can be caused by the fact that fast neutrals are in this case ionized deep enough in the plasma and the effect caused by the low field side edge ionization is suppressed.

Impact of the magnetic field and the plasma current

The last studied parameter that influences the absorbed and lost NBI power in the plasma is the impact of the fast ion Larmor radius and the banana orbit width. The fast ions orbits are affected by the toroidal magnetic field B_{t} and the plasma current I_{P}. They are having an impact mainly on the Larmor radius of fast ions $r_{\mathrm{L}} \sim 1/B_{\mathrm{t}}$, their banana orbit widths $\sim q r_{\mathrm{L}}$, where q is the safety factor $\sim 1/I_{\mathrm{P}}$, and the helicity of the resulting magnetic field lines. Therefore the sets of the discharges investigating the influence of the toroidal magnetic field B_{t} and the plasma current I_{P} on the NBI power inside the plasma P_{NBI} were realized. The results are shown in the figure 6.17.

It seems that in the studied range of the toroidal magnetic field B_{t} and the plasma current I_{P}, the impact of the fast ions trajectories variation is not significant. However, the difference between NBI1 and NBI2 is still well visible and it is comparable with the figure 6.13 left panel. The density chosen for the discharges

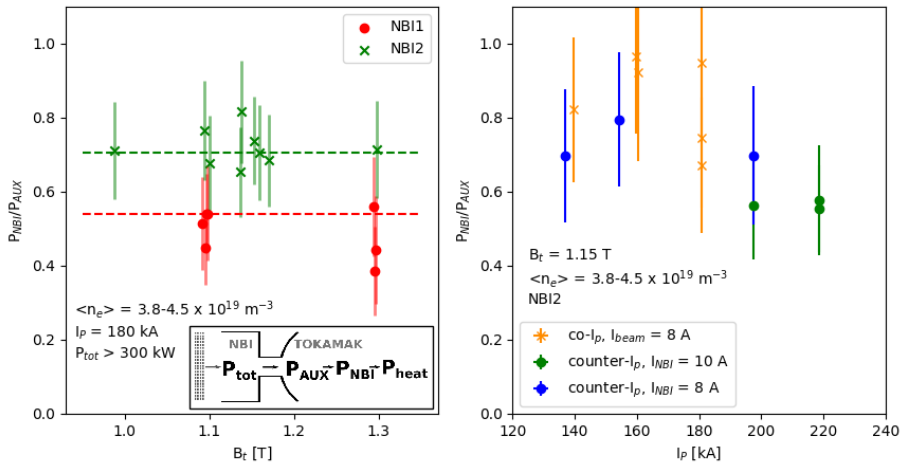

Figure 6.17: Fractions of the NBI power P_{NBI} derived by the power balance and the NBI power entering the tokamak chamber P_{AUX} as a function of the toroidal magnetic field B_{t} (left) for NBI1 (dots) and NBI2 (crosses) and as a function of the plasma current I_{P} (right) for co- and counter-injection. The dashed lines in the left panel corresponds to the ratios $P_{\mathrm{NBI}}/P_{\mathrm{AUX}}$ derived in the figure 6.13 for the NBI1 and NBI2.

in which the plasma current dependence of $P_{\mathrm{NBI}}/P_{\mathrm{AUX}}$ was observed is close to the optimal density identified for the counter-injection (see above text dedicated to the co- and counter-injection differences or the figure 6.16). Therefore the co- and counter-injected discharges end up with similar values of $P_{\mathrm{NBI}}/P_{\mathrm{AUX}}$ in the figure 6.17.

Conclusion

There are two important outputs of the power balance analysis. The predicted beam scraping, the equation (4.11), is in an agreement with the measurements determined by the power balance analysis, as can be seen in the figure 6.13. There is a slight disagreement only for the lowest NBI powers. Therefore the scraping power losses derived in equation (4.11), that enumerates the fraction of the NBI power passing through a given narrow NBI port, is used in the following analysis to determine P_{AUX}.

The unexpected result is, that the NBI1 provides $\sim 17\,\%$ less power into the tokamak than NBI2, as seen in the figures 6.13 and 6.17. There can be various causes of this, such as a misalignment of NBI1, inaccuracy in the ion optics, which can lead to an unfocused beam, or a wider beam due to higher beamlet divergence. This difference in the delivered power into the COMPASS tokamak between NBI1 and NBI2 is taken into account when P_{AUX} is calculated in the following parts of the thesis.

There are no significant trends with varied toroidal fileds B_{t}, plasma currents I_{P}, plasma shapes or plasma densities n_{e} in case of the co-injection. It seems there is an optimal window for the range of plasma line-averaged densities for the counter-injection $\sim$ 4-5 $\times$ 10^{19} m^{-3} with an enhanced NBI power deposited in a plasma P_{NBI}.

6.2 Energy confinement time

The energy confinement time τ_E is one of the parameters of the triple product in the Lawson equation (1.4), which defines the threshold for fusion ignition. The energy confinement time τ_E describes the power loss rate of the total power applied into a plasma. It is often used as a reference value for comparison of the various fusion devices.

Due to many parameters affecting plasma transport, it is practically impossible to determine an analytical formula for the energy confinement time τ_E based on the tokamak basic physics principles. Therefore there are attempts to derive energy confinement time scalings based on the measured confinement times databases. It is important for the design of new machines, such as ITER. Here the widely used energy confinement times scalings for L-modes and H-modes are compared with energy confinement times measured on the COMPASS tokamak. Part of the below discussed analysis of the energy confinement time for the COMPASS tokamak was presented in [67].

The energy confinement time τ_E is evaluated based on the equation (1.3) from the total stored energy W in the plasma and the total input heating power delivered into plasma P_{in}. The terms are derived in the case of the COMPASS tokamak as follows. The total stored energy W is determined by the EFIT reconstruction W_{EFIT}. The plasma heating power P_{in} is equal to the ohmic heating power P_{ext} in case of the ohmic discharges or to a sum of the ohmic heating power P_{ext} and the NBI auxiliary heating power P_{AUX} in case of the NBI-heated discharges. The auxiliary heating power P_{AUX} is derived from the equation (4.11) and it is lowered by an additional 17 % for NBI1 injector, as it seems there are systematically additional losses based on the conclusion in the section 6.1.

L-mode energy confinement time scalings

The first examined energy confinement time scaling is the so-called *neo-Alcator* scaling. On the Alcator tokamak it was observed that the energy confinement times are linearly growing with the line-integrated plasma densities $\langle n_{\mathrm{e}} \rangle$. Later, it was discovered, that this linear increase saturates at a certain value and does not increase anymore for even higher plasma densities. This limiting plasma density is so-called saturation density n_{sat}. The shortcuts for linear regime and saturated regime are LOC (linear ohmic confinement) and SOC (saturated ohmic confinement) respectively. These original observations were done for L-mode discharges. Later on, it was found that there are different phenomena ongoing while transition between LOC and SOC. Despite that LOC and SOC regimes are well known, it is not still fully explained what is causing the transition. The currently known phenomena related to the LOC-SOC transition are summed up in [68].

The definitions of the neo-Alcator scaling [5], p. 285 and saturation density [3], p. 181 are following:

$$\tau_{\mathrm{Alc}}(\mathrm{s}) = 0.103\, q^{0.5} \langle n_{\mathrm{e20}} \rangle a^{1.04} R^{2.04}\,, \tag{6.8}$$

$$n_{\mathrm{sat}}(\mathrm{m}^{-3}) = 0.06 \times 10^{20} I_{\mathrm{P}} R A^{0.5} \kappa^{-1} a^{-2.5}\,, \tag{6.9}$$

where q is the safety factor. The safety factor at magnetic surface $\rho = 0.95$ q_{95} is usually used. $\langle n_{e20} \rangle$ is the line-integrated plasma density in $10^{20}\,\mathrm{m}^{-3}$, a and R are the plasma minor and major radius in meters, I_P stands for a plasma current in MA, A is an atomic mass of a major plasma species and κ is the plasma elongation.

The measured energy confinement times are obtained from the EFIT energy W_{EFIT}, from the ohmic heating power P_{ext}, which exhibits high noise level as seen in the figure 6.2, and from the NBI auxiliary heating power P_{AUX}. To eliminate impact of the inputs noise level and time derivatives in the energy confinement time determination, equation (1.3), only discharge stages at least 15ms long in the steady stage of the discharge are considered. Despite that, the resulting uncertainty of the energy confinement time τ_E is high and therefore their error-bars are not displayed in all figures in this section.

The comparison of the COMPASS data with neo-Alcator scaling had been already published, when COMPASS was operated in the Culham Laboratory [69], UK. A comparison of the previously measured energy confinement times with currently measured is shown in the figure 6.18.

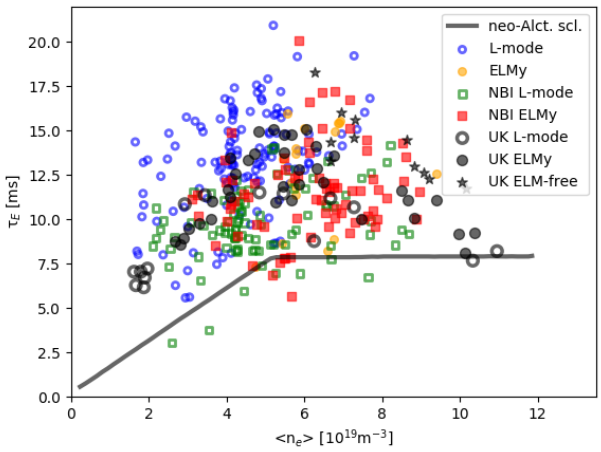

Figure 6.18: The energy confinement time τ_E dependence on the line-integrated plasma density $\langle n_e \rangle$ for various operation modes (L-modes, ELMy H-modes and ELM-free H-modes, with/without NBI heating). The data points and neo-Alcator scaling, LOC and SOC parts, from [69] are plotted by grey markers and the grey line respectively. The data points measured during COMPASS operation at IPP, CAS are depicted by coloured symbols.

The energy confinement times τ_E measured during the COMPASS operation at IPP, CAS have comparable values with the previous measurements done during the UK COMPASS operation. The energy confinement times τ_E are systematically above the line, that corresponds to the neo-Alcator scaling for the COMPASS tokamak.

When NBI auxiliary heating has become available for the fusion research, it was found that the energy confinement times τ_E degrades with an applied additional heating power. Therefore, the new confinement time scaling, which includes the additional heating power, was introduced, so-called Kaye-Goldston energy confinement time scaling [5], p. 286. It consists from a thermal part,

which is represented by the neo-Alcator scaling, and from an auxiliary heating part, which is represented by τ_{AUX}. This scaling is valid for L-mode discharges.

$$\tau_{\mathrm{K-G}} = \left(\frac{1}{\tau_{\mathrm{Alc}}^2} + \frac{1}{\tau_{\mathrm{AUX}}^2} \right)^{-1/2} \tag{6.10}$$

$$\tau_{\mathrm{AUX}}(\mathrm{s}) = 0.037 \kappa^{0.5} I_{\mathrm{P}} P_{\mathrm{in}}^{-0.5} a^{-0.37} R^{1.75} \tag{6.11}$$

Where P_{in} is a total plasma heating power in MW.

Later on, there were more data available and newer energy confinement times scalings were published. Here one more scaling for L-modes, which is widely used, is introduced. It was developed for the ITER energy confinement time prediction and is called ITER89-P [3], p. 740.

$$\tau_E^{\mathrm{ITER89-P}}(\mathrm{s}) = 0.048 I_{\mathrm{P}}^{0.85} R^{1.2} a^{0.3} \kappa^{0.5} \langle n_{\mathrm{e20}} \rangle^{0.1} B_{\mathrm{t}}^{0.2} A^{0.5} P_{\mathrm{in}}^{-0.5} \tag{6.12}$$

Where B_{t} is a toroidal magnetic field on a plasma axis.

The above mentioned scalings can be compared with the measured values on the COMPASS. Moreover, it is possible to clarify the heating power dependence as in the COMPASS experimental database are available L-mode experiments with the additional NBI heating, where two flat-top stages with and also without NBI heating are achieved, while other plasma parameters are kept constant. A dependence of the ratio of the measured energy confinement times τ_E with and without (ON/OFF) NBI on the ratio of the heating powers P_{in} with and without (ON/OFF) NBI are shown in the figure 6.19.

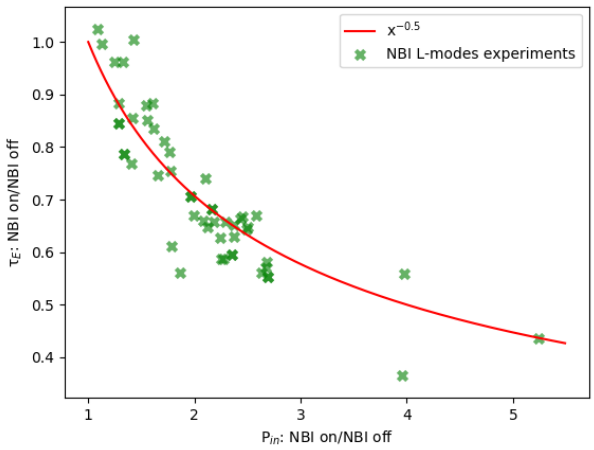

Figure 6.19: The ration of the energy confinement times τ_E measured during the NBI-on and NBI-off flat-top stages of the discharge in respect to the ratio of the total heating powers P_{in} for the corresponding discharge stages. Each point is derived based on the NBI on/off stages of single discharge, which should eliminate impact of the discharge specific parameters. Other plasma parameters are kept constant during both, NBI on/off, discharge stages.

The data obtained in the NBI heated L-mode discharges on the Compass tokamak nicely follows the expected $x^{-0.5}$ trend. A comparison of the experimental confinement times and those based on the introduced L-mode scalings is shown in the figure 6.20.

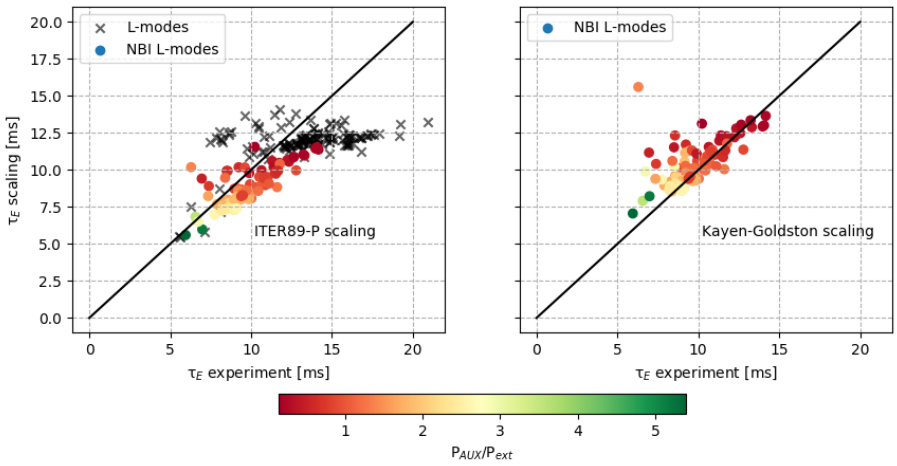

Figure 6.20: A comparison of the experimental and scaling-based, the equations (6.12), (6.10), energy confinement times τ_E for a set of the flat-top ohmic (black crosses) and NBI-heated (coloured dots) L-modes. The ohmic discharges are displayed only for ITER89-P scaling, as the Kayen-Goldston scaling was primarily derived for the auxiliary heated discharges. The colour of the dots corresponds to the fraction of the auxiliary heating P_{AUX} and the ohmic heating power P_{ext}.

The NBI heated discharges nicely follow both scalings. On the other hand, there is a group of the ohmic L-modes, which exhibit slightly better energy confinement times than predicted. It is again nicely seen that as the portion of the auxiliary heating increases, the energy confinement time drops.

H-mode energy confinement time scalings

Once the H-mode has been discovered, there were attempts to find out confinement time scalings also for the H-modes. Actually, an increased energy confinement time τ_E is one of the basic H-mode feature, as the H-mode stands for a high confinement mode. It was shown that the H-mode can reach up to two times higher energy confinement times, as it would be in case of L-mode with the same plasma parameters. In this section, the COMPASS H-mode energy confinement times τ_E are compared with widely used H-mode energy confinement time scaling, called IPB98(y,2) [3], p. 740, [4], p. 131, introduced in the equation (6.13). This scaling is valid for the H-modes accompanied with the edge localized modes (ELMs). The H-mode and ELMs are introduced in the section 3.5.2.

$$\tau_E^{\mathrm{IPB98(y,2)}}(\mathrm{s}) = 0.145 I_{\mathrm{P}}^{0.93} R^{1.39} a^{0.58} \kappa_{\mathrm{a}}^{0.78} \langle n_{\mathrm{e20}} \rangle^{0.41} B_{\mathrm{t}}^{0.15} A^{0.19} P_{\mathrm{in}}^{-0.69}\,, \tag{6.13}$$

where κ_{a} is a ratio of the area of the plasma cross-section inside the separatrix A and the circle area with the major radius a:

$$\kappa_{\mathrm{a}} = \frac{A}{\pi a^2}\,. \tag{6.14}$$

A comparison of the measured confinement times τ_E with IPB98(y,2) scaling is shown in the figure 6.21.

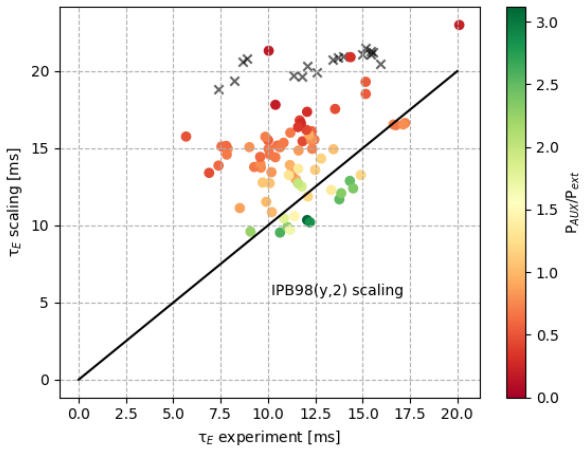

Figure 6.21: A comparison of the experimental and scaling-based H-modes energy confinement times τ_E for ohmic (crosses) and NBI-heated (dots) discharges. Color corresponds to a ratio of the auxiliary heating power P_{AUX} and the ohmic heating power P_{ext}.

The COMPASS ELMy H-modes seem to have quite low energy confinement times when compared with the H-mode scaling IPB98(y,2). The lower H-mode confinement quality is usually given by presence of ELMs, which eject plasma particles and energy out of the confined region. The magnitude of the confinement degradation caused by the ELMs vary with the ELMs kind, frequency and magnitude. The discharges with a higher fraction of the auxiliary heating are closer to the confinement scaling, than the ohmic heated only or with low fraction of the auxiliary heating.

conclusion

The energy confinement times measured during COMPASS operation at IPP, CAS are in the same range as the measured one during its previous operation in the Culham Laboratory and they are both above values expected by the neo-Alcator scaling as seen in the figure 6.18. The predicted drop of the energy confinement times with the increased heating power $\tau_E \sim P_{\mathrm{in}}^{-0.5}$ was confirmed in the figure 6.19. Generally, the measured energy confinement times during L-modes and ELMy H-modes are close to the expected values by scaling laws as seen in figures 6.20 and 6.21.

6.3 Kinetic profiles

The main goal of the auxiliary plasma heating is to enhance plasma temperatures, mainly in the plasma core. Fast ions in plasmas transfer their energy into both bulk plasma particles, ions and electrons. The portion of the power deposited into ions and electrons depends on the critical energy E_{C} defined by the equation (3.5). The kinetic energy of the fast ions is transferred into the plasma as the bulk plasma thermal energy, but also as the additional plasma momentum, i.e. modifying the plasma rotation. The injected neutrals are also an additional plasma fueling, which can cause an increase of the plasma density. This chapter

focuses on the impact of the NBI heating on the plasma temperatures and density and shape of their profiles. The impact of the NBI heating on the plasma rotation is omitted, as it is not routinely measured quantity on the COMPASS tokamak.

The electron temperature and density profiles are measured on the COMPASS tokamak by the Thomson scattering system (TS) equipped with four lasers. The repetition rate of each TS laser is 30 kHz. Therefore there are only a few TS profiles measured during studied flat-top stages. To increase a number of the averaged points, ten innermost core TS points are used, which values match well within their error-bars, as the electron temperature and density profiles at COMPASS are rather flat. A low number of the measured TS time points, usually 2 or 3 in the analyzed stages of discharges, introduces an additional error into results as the Thomson system is asynchronous with the sawtooth instability. The sawtooth causes variation in the core electron temperature by $\sim 200\,\mathrm{eV}$ and in the core electron density $\sim 0.5 \times 10^{19}\ \mathrm{m}^{-3}$, as is shown later in the section 7.1. This is considered as the additional error of the derived values.

The second available diagnostic on the COMPASS tokamak, which detects electron temperature profiles, is the radiometer, which measures the electron cyclotron emission (ECE). The studied set of the discharges are in over-dense regime for the standard ECE measurements, but here the relative changes of the core electron temperature are derived thanks to the waves conversion EBW-X-O [40]. The advantage of ECE is the fact, that it has high time resolution and therefore by long period averaging the sawtooth additional error vanishes. However, the signal is disappearing for high plasma densities.

Ion temperature and plasma rotation is nowadays usually measured by charge-exchange recombination spectroscopy (CXRS) on other tokamaks. Unfortunately, this system was not available on the COMPASS tokamak for studied set of discharges. Therefore the neutral particle analyzer (NPA) data are used to determine plasma ion temperatures by an older method. A short overview of the basics of this diagnostic is given in subsection 4.1.

The following subsection contains details about the NPA ion temperature determination and it is followed by the subsection dedicated to the natural dependence of the plasma temperatures on the plasma densities for ohmic L-modes. Then, the impact of the additional heating source location on the kinetic profiles shapes is discussed. The variation of the core values of the plasma temperatures and density is presented for L-mode discharges performed on the COMPASS tokamak that utilize the NBI2 injector co- and counter-injected and NBI1 injector co-injected. The systematic studies of the NBI impact on the H-mode discharges were not done. Examples of the kinetic profiles during NBI-heated H-mode discharges are shown later in the section 7.2.

6.3.1 Ion temperature from the neutral particle analyzer

Neutral particle analyzers measure energy spectra of neutral particles escaping from tokamak plasmas Γ. The basics of the neutral particle analyzer itself are described in the subsection 4.1.1. If the neutral particle analyzer operates in the low energy range, called also thermal, with measured energy range between hundreds of eV and a few keV, it collects neutrals, which are products of the charge-exchange collision of the plasma thermal ions and background neutrals.

The escaping neutrals have the same energy distribution as the original thermal ions. If we assume that the measured escaping neutrals birth place is well localized in the plasma core and simultaneously that plasmas are transparent for neutrals within the measured energy range, means that we can neglect variation of all terms in the equation (4.2). The dependence of the measured flux on the ion temperature T_i is then simplified accordingly:

$$\Gamma(E_\mathbf{n}) \sim \sqrt{E_\mathbf{n}} \exp\left(-\frac{E_\mathbf{n}}{T_\mathrm{i}}\right) , \tag{6.15}$$

where $E_\mathbf{n}$ is the energy of the counted neutrals by NPA and T_i should equal the core ion temperature $T_\mathrm{i}(0)$. However, the assumption that all terms in the equation (4.2) can be considered as constants is barely fulfilled, as the measured fluxes origin location, the emissivity function in the equation (4.3), usually differs with the energy of the measured flux as seen in [49] for the COMPASS tokamak or in [48] for the ASDEX Upgrade tokamak. The ion temperature derived from the slope of the $\log(\Gamma(E_\mathbf{n})/\sqrt{E_\mathbf{n}})$ is usually labeled as T_CX, as it is based on the neutrals, which are products of the charge-exchange collisions. Using the code DOUBLE [51], which is a synthetic NPA diagnostic, and predefined ion temperature profiles, it was shown that despite the invalidity of the assumptions leading to the simplified equation (6.15), T_CX derived from the synthetic diagnostic data deviates from the core ion temperatures $T_\mathrm{i}(0)$ by $\sim 100\,\mathrm{eV}$ [49] for the examined core plasma density range $2\text{–}10 \times 10^{19}\,\mathrm{m}^{-3}$. As this deviation mainly depends on the plasma density, we can expect that the relative changes of T_CX are same as the relative changes of $T_\mathrm{i}(0)$ for discharges with constant density.

It was also shown in [49], that a magnitude of the difference between the determined ion temperature and the real core ion temperature $\Delta(T_\mathrm{CX}, T_\mathrm{i}(0))$ depends on the energy range of the NPA data used for the calculation of the flux energy spectra. Examples of the measured energy spectra and of the determined ion temperature T_CX for various energy ranges are shown in the figure 6.22.

The fluxes measured by NPA for plasmas without NBI operation (green dots) are above noise level, represented by the grey dotted lines in left panel of the figure 6.22, up to energy $\sim$ 2500–3500 eV. Noise levels, the grey dotted lines, are determined by the low count rate, 1 3 or 5 counts per measured time window, of the measured fluxes. For lower densities, up to $\sim 4 \times 10^{19}\,\mathrm{m}^{-3}$, the determined ion temperatures T_CX of ohmic L-modes for the E_stop in the range $\sim 2500\text{–}3500\,\mathrm{eV}$ of analyzed energy spectra have comparable values as seen in the right panel of the figure 6.22. Once the higher energy channels with a low count rate are also used in the evaluation of the ion temperature T_CX the resulting ion temperature T_CX is increasing. On the other hand, the ion temperature T_CX dependence on the considered energy range for high density discharges is observed even if E_stop is low. This is given by the fact that dense plasmas in case of the COMPASS tokamak are not transparent for the escaping neutrals and the birth location, i.e. the emissivity, of the measured neutrals by NPA strongly varies with their energies as shown in [49]. Generally, the emissivity moves outwards with the increasing plasma density or the decreasing measured flux energy.

NPAs are also installed on other tokamaks, so we can draw on the experience obtain on these machines. For example on the TCV tokamak, which has similar dimensions and operational parameters as the COMPASS tokamak, uses the

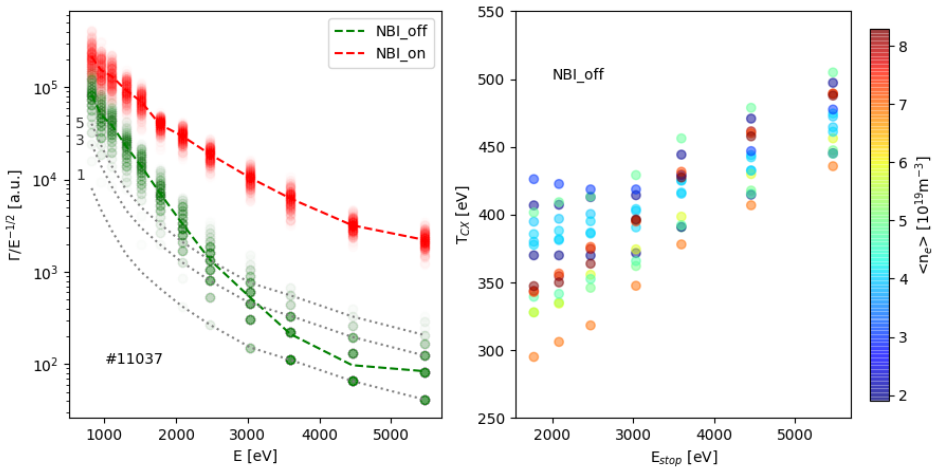

Figure 6.22: left: The measured neutral fluxes Γ for L-mode discharge #11037 in NBI-off (green) and NBI-on (red) discharge stages. The dotted lines represents flux corresponding to the count rate 1, 3 and 5 particles per one measured time window, which was in this case 80 μs, to highlight the low count rate signals. Right: Ion temperature for various L-modes determined from the slope of the NBI-off fluxes for various energy ranges. The slope of $\log(\Gamma(E_\mathbf{n})/\sqrt{E_\mathbf{n}})$ is taken from the lowest energy channel up to the channel with an energy E_{stop} on the x-axis. A color represents the line-integrated plasma density $\langle n_\mathrm{e} \rangle$.

measured flux energies in the range $\sim$ 2–8$\times$ of the expected core ion temperature $T_\mathrm{i}(0)$ for the ion temperature determination [70]. That would be in the case of the core ion temperature $T_\mathrm{i}(0) = 400$ eV a range 800–3200 eV. The determined ion temperature T_CX of ohmic L-modes in the figure 6.22 is constant for lower plasma densities when it is evaluated from fluxes in the energy range up to $\sim$ 2500 eV. The increase of the derived T_CX is caused by the low count rate of the higher energy channels signals (green dots in the left panel in the figure 6.22). Considering this fact, the conclusions in [49] and the above mentioned recommendation from the TCV tokamak, the considered energy range for T_CX determination is chosen to be from 800 eV up to 2500 eV for the ohmic L-modes.

While NBI is in operation and shortly after, there is a population of the non-maxwellian fast ions in the plasma. The presence of these fast ions in the plasma leads to the formation of the fast neutral fluxes escaping plasma, which contribute to the measured NPA flux Γ, as seen on the difference between NBI-on and NBI-off fluxes in the left panel of the figure 6.22. To eliminate the fast neutrals impact on the derived ion temperature T_CX the energy range for NPA fluxes that are used in determining the ion temperature T_CX is shrunken to be from 800 eV up to 2000 eV for the NBI-heated stage of discharges. To improve the ion temperature values quality the flat-top stages are analyzed, which allow to sum up the counts during long time periods. The resulting $T_{\mathrm{i}0}$ error consists of the aforementioned $\sim$ 100 eV deviation estimated from T_CX and a a flux fitting error. The flux fitting error considers the uncertainty of energy range of each NPA channel combined with the uncertainty of the flux count given by the Poisson distributed count rate.

There was another possible correction of the NPA ion temperature T_CX to derive the core ion temperature $T_\mathrm{i}(0)$ evaluated for the COMPASS tokamak NPA,

ACORD-24 [43]. The dependence of the ratio of the core ion temperature and the evaluated ion temperature $T_i(0)/T_{CX}$ was determined using DOUBLE simulation with parabolic shapes of plasma temperatures and density. Resulting temperature ratio as an output of this method is shown in the figure 6.23. It can be clearly seen that for sufficiently low plasma densities the evaluated T_{CX} closely matches the core ion temperature T_{i0}.

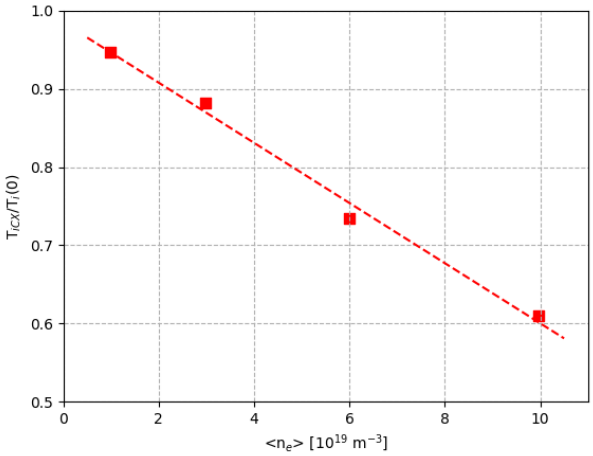

Figure 6.23: Expected ratio of the ion temperature derived from the NPA flux slope T_{CX} and the core ion temperature T_{i0} as a function of the line-integrated density $\langle n_e \rangle$ for the COMPASS NPA. Image reprinted from [43].

6.3.2 Ohmic L-mode temperature

The energy exchange between different species of plasma particles is given by their collisionality, which is proportional to the particle species density. As the driven plasma current heats up mainly electrons, which than transfer their energy to the plasma ions, it is possible to observe different temperatures for different species, if the energy exchange is not sufficient. The core electron and the core ion temperatures with respect to the plasma densities for ohmic phases of the L-mode discharges, where $I_P = 180$ kA, $B_t = 1.15$ T, are shown in the figure 6.24.

As can be seen in figure 6.24 the NPA ion temperature T_{CX} and the core ion temperatures $T_i(0)$, based on the correction in the figure 6.23, do not significantly vary with the plasma line-averaged density $\langle n_e \rangle$. On the other hand, the observed core electron temperatures $T_e(0)$ are $\sim$ 2–3$\times$ higher then the measured core ion temperatures T_{CX}, $T_i(0)$ for the lowest plasma line-averaged densities $\langle n_e \rangle$. This difference gets smaller with increasing the plasma line-averaged density $\langle n_e \rangle$. The electron temperature is crucial for the fast ions slowing down, as it defines the critical energy E_C, which is given by the equation (3.5). Fast ions are dominantly slowed down on bulk plasma electrons until they reach to the critical energy E_C. After this they are more likely to be slowed down on the bulk plasma ions. Therefore, the electron temperature directly determines the expected ratio of the transferred power into the plasma ions and electrons from the fast ions. Based on the observed drop of the core electron temperatures with the plasma line-averaged densities, as seen in the figure 6.24, we can expect that the bulk electron heating

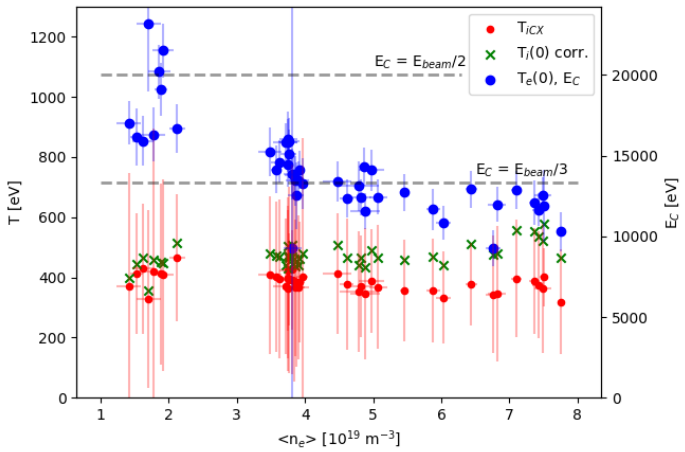

Figure 6.24: The core electron temperatures $T_e(0)$ (blue dots), the NPA ion temperatures T_{CX} (red dots) and the corrected core ion temperatures $T_i(0)$ (green crosses), defined by the figure 6.23, as a function of the line-averaged density $\langle n_e \rangle$ for the ohmic stage of the L-modes. The right axis, valid for the blue dots only, shows corresponding values of the critical energy E_C, which is directly proportional to the electron temperature $T_e(0)$, and it is defined in the equation (3.5).

by the fast ions will be lower for the higher plasma densities and vice versa for the bulk ions heating.

6.3.3 Kinetic profile flattening

Generally, additional plasma heating can cause kinetic profiles, such as the plasma temperatures and the plasma density, flattening if the absorption is well localized in a small region of the plasma magnetic surfaces outside the plasma core [2]. Consequently, the profile is flat between plasma core up to the additional heating location and drops towards edges. This could theoretically occur when the plasma density is too high for NBI core deposition. The NBIs for the COMPASS were constructed with energy 40 keV, which should be optimal for densities ~ 4–$5 \times 10^{19}\,\mathrm{m}^{-3}$. Examples of the electron density and temperature profiles, which are available for the COMPASS tokamak, for various plasma densities for NBI2 L-mode experiments with $B_t = 1.15$ T and $I_P = 180$ kA and different NBI heating power are depicted in the figure 6.25.

As it can be seen, we do not observe evidence of additional profiles flattening. It means that NBI fast ions are well distributed within the plasma. The drop of the electron temperature for the ohmic stage of the discharges with the increase of the plasma density is observed again. It can be also seen that at the lowest plasma density, there is a slight grow of the plasma density during NBI phase, despite the fact that we have been using density feedback during these discharges. Simultaneously, there is a drop of the core electron temperature in this case, which can be caused by the general drop of the electron temperature with the plasma density, by the lowering of the energy confinement time, see the figure 6.19, with the applied heating power or as an artefact of the sawtooth oscillations, as seen in the figure 7.1. It is evident, that the total electron heating is weak, as can be

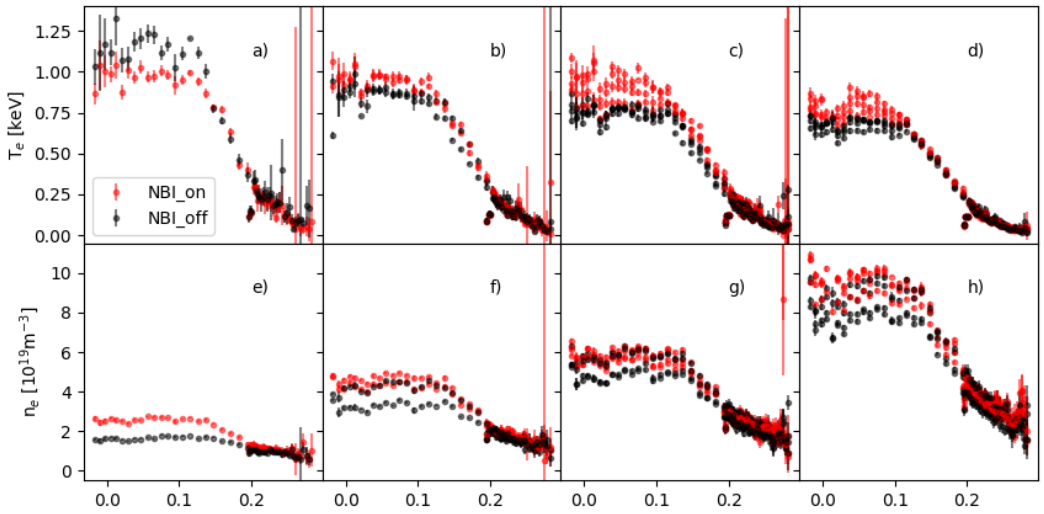

Figure 6.25: The electron densities and temperatures for various plasma densities, increasing from left to right side. Each profile is an averaged profile over the flat-top stage of the NBI-off/-on stage of one discharge. The red dots represent the profiles during the flat-top phases with the additional NBI heating and black dots stand for the flat-top phases of same discharges but ohmic discharge stages. There is no evident additional profiles flattening during the NBI phase. The additional fueling is noticeable only for the lowest plasma density during NBI-on phase.

seen on the NBI-on and NBI-off electron temperature changes. The impact of the NBI heating on the core temperatures and density values is discussed more in the following section.

6.3.4 Change of the core temperatures and densities during L-mode due to NBI heating

Here the relative changes of the core ion and the core electron temperatures and the line-averaged density for various sets of the NBI assisted L-mode discharges introduced in the chapter 5 and analyzed in the section 6.1, are shown. Before the relative changes study itself an example of the time traces of the Thomson scattering data and the NPA data are shown in the figure 6.26.

As the ohmic core electron temperature, and consequently the critical energy E_C, which determines the ration of the bulk ions and electrons heating, varies with the plasma density, as seen in the figure 6.24, it can be expected that the heating of the ions and electrons will evolve also with the plasma density. The relative changes of the electron and the ion temperatures and the line-averaged plasma densities as a consequence of the additional NBI heating for the Basic Co-current and the Shape L-mode scans, as defined in the table 5.1, are depicted in the figure 6.27.

It seems there is no significant difference in the temperatures or densities increases between studied plasma shapes in the figure 6.27. The plasma densities grow is well observed only for the lowest plasma densities, $\sim 2 \times 10^{19}$ m^{-3}. There are two reasons for the plasma density increases due to the NBI. The direct additional plasma fuelling by NBI particles and indirect NBI fuelling. Indirect

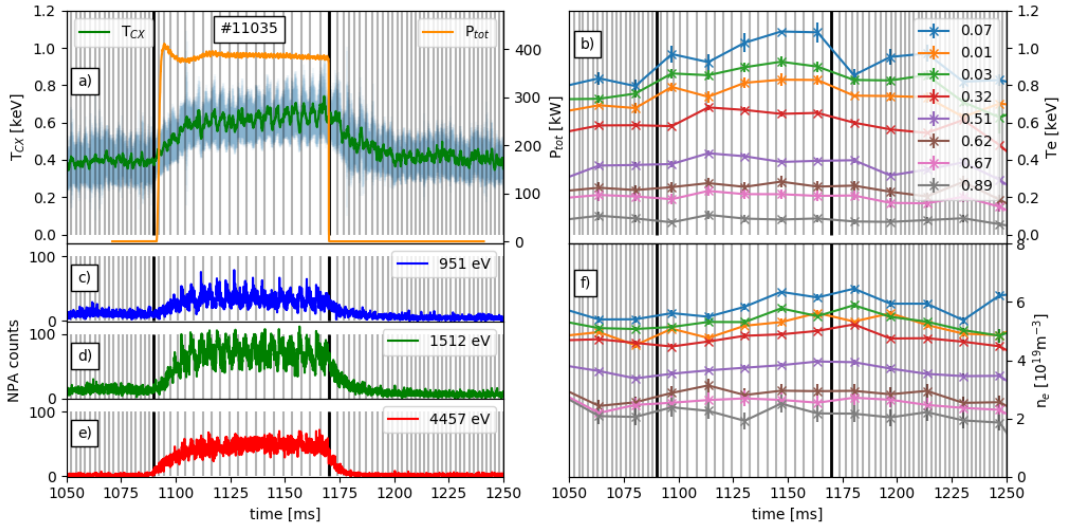

Figure 6.26: a) The NPA ion temperature (green) including error bars (blue) and the total power P_{tot} produced by NBI2 (orange), b) and f) the electron temperature and density for various Ψ normalized positions measured by the Thomson scattering, c), d) and f) the NPA counts for the various NPA energy channels. The oscillations on the NPA fluxes and ion temperature, mostly visible during NBI heated stage, are correlated with the sawtooth instability in the plasma core, which is discussed later in the section 7.1. The sawtooth crashes are highlighted by the grey vertical lines. The black vertical lines represents NBI start and stop.

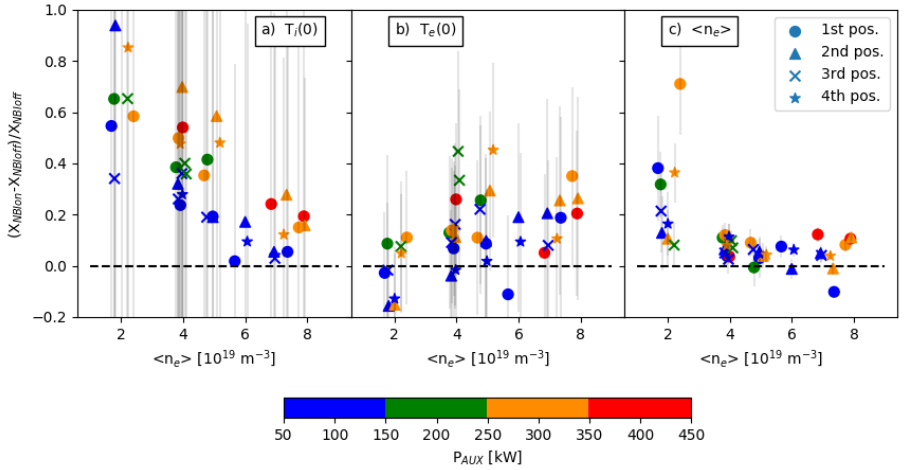

Figure 6.27: Relative increases of the core ion temperatures $T_{\mathrm{i}}(0)$ (a), the core electron temperatures $T_{\mathrm{e}}(0)$ (b), from Thomson measurements only, and the line-averaged plasma densities $\langle n_{\mathrm{e}} \rangle$ (c) due to the NBI heating as a function of the on/off mean line-averaged plasma density $\langle n_{\mathrm{e}} \rangle$ for various plasma positions and shapes (figure 5.1). The markers color corresponds to the applied NBI auxiliary heating power P_{AUX}.

fuelling encompasses particles from the tokamak walls that are additionally desorbed from tokamak walls and plasma facing components (PFC) as a consequence of the higher power losses through the separatrix P_{sep} while NBI is ongoing. The

additional fuelling due to NBI is usually, at higher densities, balanced by a density feedback that lowers the primary gas puff. However, at the lowest densities, the gas puff is already low or even completely off before NBI starts. Therefore even if the gas puff is fully stopped during NBI phases, the additional fueling due to NBI leads to the plasma density growth.

Regarding the core ion temperature $T_\mathrm{i}(0)$, we can see that with the increasing applied NBI auxiliary heating power P_AUX, the core ion temperature grows. However, the efficiency of the bulk ion heating degrades with the plasma line-averaged density $\langle n_\mathrm{e} \rangle$. This is a result of the lower electron temperature and consequently the lower critical energy E_C, defined by the equation (3.5), for high plasma line-averaged densities $\langle n_\mathrm{e} \rangle$, as seen in the figure 6.24. The lower critical energy E_C is for a given energy of NBI, the less total NBI power is transferred into the bulk plasma ions and more into the plasma electrons.

On the other hand, the influence of the NBI heating on the core electron temperature $T_\mathrm{e}(0)$ is not as clear as in the case of the core ion temperature $T_\mathrm{i}(0)$. This is partially due to the oscillations caused by the sawtooth instability, which brings a high additional noise into the measured data. An example of the electron temperature profiles with respect to the sawtooth crashes is depicted in the figure 7.1. This problem is not present for the ECE measurements, since the diagnostic method has higher temporal resolution and therefore it is possible to determine the averaged electron temperature changes, i.e. the sawtooth oscilations do not play a role. Despite the plasma densities are above the critical density for the direct ECE measurements, the relative electron temperature changes are available due to the EBW-X-O wave conversion [40]. The results for the Basic Co-current scan are shown in the figure 6.28.

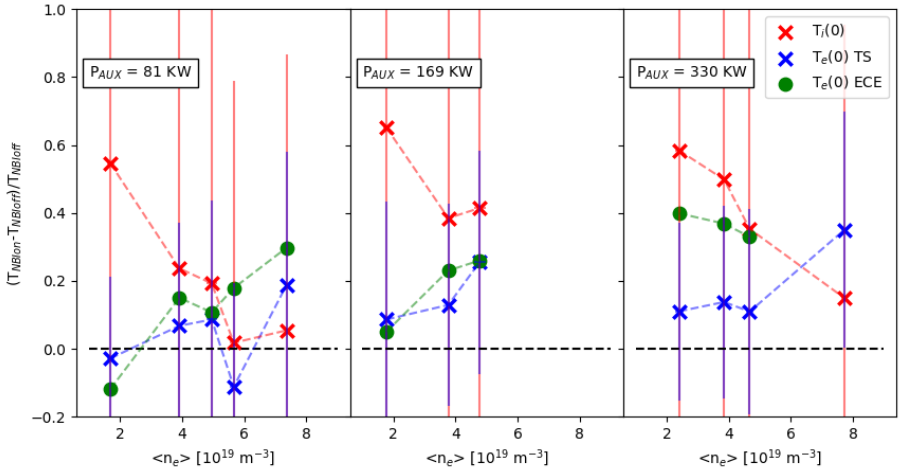

Figure 6.28: Density dependence of the relative changes of the core ion and the core electron temperatures during NBI-on and NBI-off stages of discharges from the Basic Co-current scan. Shown are data measured by the neutral particle analyzer ($T_\mathrm{i}(0)$), the Thomson scattering system ($T_\mathrm{e}(0)$ TS) and the radiometer, measuring the electron cyclotron emission, ($T_\mathrm{e}(0)$ ECE), reprinted from [40], measured in discharges of the Basic Co-current scan shown for various NBI auxiliary powers (P_AUX).

It can be seen that the observed core electron temperature $T_\mathrm{e}(0)$ increase as the

consequence of the NBI heating is comparable in TS and ECE data for the lower NBI powers. There is a different trend in case of the ECE data for the highest NBI power, but they are still within the TS data points error-bars. Generally, it seems that the electron temperature $T_e(0)$ increase more for the higher plasma densities. This is also a consequence, that the starting electron temperature is lower at higher plasma densities, as seen on the figure 6.24. A change of the energy confinement quality can also play a role, as the energy confinement time degrades with the applied heating power, as discussed in the section 6.2. Additionally, the plasma density increase in case of the lowest studied densities $\sim 2 \times 10^{19}\,\mathrm{m}^{-3}$ can cause lowering of the core electron temperature $T_e(0)$, which is seen in the figure 6.25, as in the case of the ohmic core electron temperature, shown in the figure 6.24.

Besides the plasma line-averaged density $\langle n_e \rangle$ and the plasma shape, the plasma current I_P dependence of the temperatures and density changes can be studied, as there measured data available. Figures 6.29 and 6.30 show comparisons of co- and counter- injections with respect to the plasma density $\langle n_e \rangle$ and the plasma current I_P.

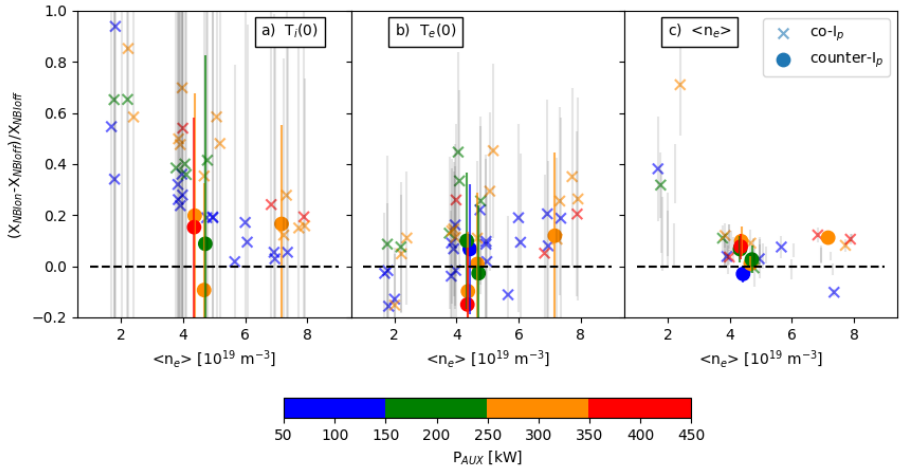

Figure 6.29: Relative increases of the ion temperatures T_i, electron temperatures T_e (from Thomson scattering measurements only) and line-averaged plasma densities $\langle n_e \rangle$ due to NBI heating as a function of the line-averaged plasma density $\langle n_e \rangle$, average value of the NBI-on and NBI-off discharge stages, for co- and counter-injection The markers color corresponds to the applied NBI auxiliary heating power P_{AUX}.

As there are only 5 measured discharges available for the counter-current case and 4 of them have been performed with the similar line-averaged density $\langle n_e \rangle \sim 4 \times 10^{19}\,\mathrm{m}^{-3}$ it is hard to make any conclusion. Therefore the following statements are only preliminary. A trend of the core ion temperature $T_i(0)$ increase with respect to the line-averaged density $\langle n_e \rangle$ is not as clear in the case of the counter-current injection as in the case of the co-current injection. It seems that the increase of the core ion temperature $T_i(0)$ is lower for the counter-current discharges than for the co-current discharges. The core electron temperature $T_e(0)$ increase is pretty low for the counter-current injection. Regarding the plasma line-averaged density $\langle n_e \rangle$, there are no changes. This is a consequence of the

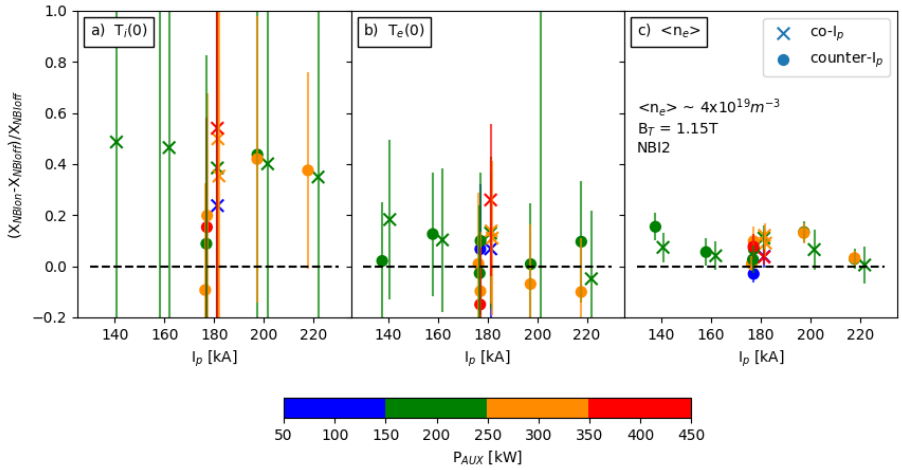

Figure 6.30: Relative increases of the ion temperatures T_i, electron temperatures T_e (from Thomson scattering measurements only) and line-averaged plasma densities $\langle n_\mathrm{e} \rangle$ as a consequence of the NBI heating with respect to the plasma current I_P.

density feedback, discussed already for the co-current case. The plasma current magnitude I_P does not have a noticeable impact on the temperatures or density increases in the case of the co-current injection. The ion temperature increase is lower for the $I_\mathrm{P} \sim 180$ kA in the case of the counter-injection. Otherwise the impact on plasma parameters for counter-current injection is similar as for the co-current injection.

It is possible to compare the observed increases of the core temperatures with the expected trends of the NBI power transferred into ions P_i and electrons P_e based on the simulations, which are introduced in the table 5.3. The results of the simulations are shown in the figure 6.31.

In absolute values, the simulations are strongly inconsistent between each other. Despite that, each predicts a drop of the ion heating with the increase of plasma density and simultaneous electron heating enhancement. These are the same trends as observed on the temperatures increase in the figures 6.27 and 6.28. The only exception is the evolution of the electron temperature increase measured by ECE for the highest NBI power, as it is seen in figure 6.28. The FAFNER simulations, which studied difference between co- and counter-injection, show significant ion heating reduction for counter-injection for both studied densities and reduction of the electron heating for higher density. The reduction of the ion heating for the counter-injection is in the agreement with the lower core ion temperature $T_\mathrm{i}(0)$ increase in the figure 6.29. However the difference in the increases between co- and counter-injection for the core electron temperatures $T_\mathrm{e}(0)$ are not well seen. Here, it has to be stressed, that the simulations provides information about the portion of the transferred NBI auxilliary heating power into ions P_i and electrons P_e. Generally, the additional heating power should lead to the increase of the corresponding temperature. But as the increased temperature of the plasma species leads to the changes in the energy confinement or presence and behaviour of the various plasma instabilities, the increase of the transferred power into plasma ions or electrons do not each time lead to the proportional

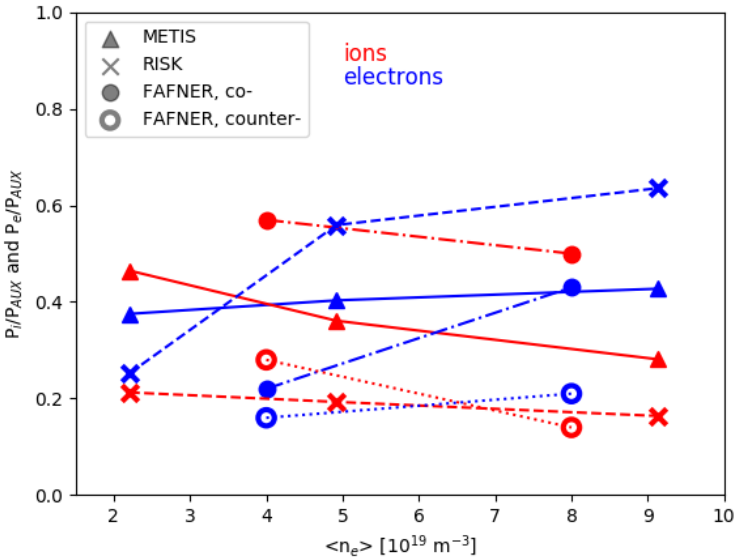

Figure 6.31: NBI auxiliary heating power P_{AUX} transferred into the plasma ions P_{i} and electrons P_{e} expected by various simulations. The simulated plasmas basic parameters are summed up in the table 5.3.

increase of the ion or electron temperature.

6.4 Neutron yield

During injection of a deuterium NBI into a deuterium tokamak plasma on the COMPASS tokamak significant neutron production is observed. Most of the neutrons in COMPASS tokamak discharges are produced in the so called beam-target collisions where fast ions originating from the NBI heating fuse with the bulk plasma ions. Therefore, the actual neutron yield is directly proportional to the plasma density n_{e}, to the fast ion density n_{fi} and the DD fusion collision rate $\langle \sigma_{\mathrm{DD}} v_{\mathrm{b}} \rangle$ in the case of the beam-target collisions, based on the equation (3.8).

An example of observed neutron yield temporal evolution during an L-mode discharge is shown in figure 6.32. It can be clearly seen that despite the basic plasma parameters and NBI power were kept constant, the neutron yield declines from the initial level. In the following paragraphs an explanation of this phenomenon is laid out.

As the plasma density is kept constant, a drop of the neutron yield has to be caused by a reduction of the fast ions density or fusion cross section. A significant part of the neutron drop can be explained by a drop of the collisional velocity between the plasma ions and the NBI passing fast ions, as the NBI transfers an additional torque into the plasma [71], which causes toroidal rotation of the plasma in the NBI injection direction. The direct measurements of the plasma toroidal rotation on the COMPASS are not available, however we can estimate a range of the toroidal rotation speed from the similar machines, like the TCV tokamak, where they measured a toroidal rotation speed caused by NBI $\sim$ 150 km/s [72]. A rough estimate of the DD fusion cross section drop can be done easily by a reduction of the NBI passing fast particles original speed by an expected

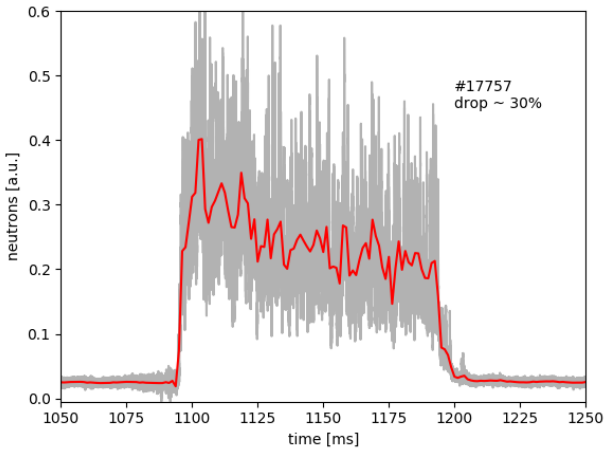

Figure 6.32: Example of the temporal evolution of the neutron yield. Neutron yield is reduced $\sim$ 30 % while other plasma parameters such as plasma density, plasma current, magnetic field are kept constant.

toroidal rotation speed. Results of this simple analysis are shown in figure 6.33.

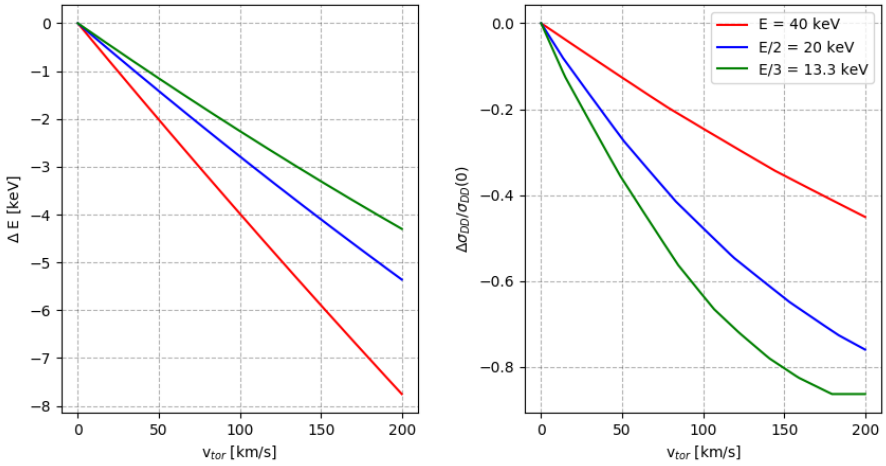

Figure 6.33: Collisional energy drop due to the additional plasma rotation (left) and a consequent reduction of the DD cross section (right) from the figure 3.3 for each NBI energy component.

The additional plasma rotation impact on the DD cross section seems as the likely explanation of the neutron drop. The most important is a drop of the DD cross section for the full energy component 40 keV, which has the highest absolute value of the DD cross section, which is depicted in the figure 3.3. The increase of the toroidal plasma rotation can decreases the effective collisional energy between the NBI fast ions and the bulk plasma ions by several keV and consequently it decrease the DD collision cross section by tens of percents as seen in the figure 6.33. However this hypothesis has to confirmed by a detailed modelling when information about the plasma rotation will be available.

The rest of this section discusses variation of the measured neutron yields at the end of the NBI injection, when it settles down and does not drop anymore. The first studied dependence is on the plasma line-averaged density $\langle n_e \rangle$, shown

in the figure 6.34, because the equation (3.8) predicts a linear dependence of the neutron yield on the plasma density.

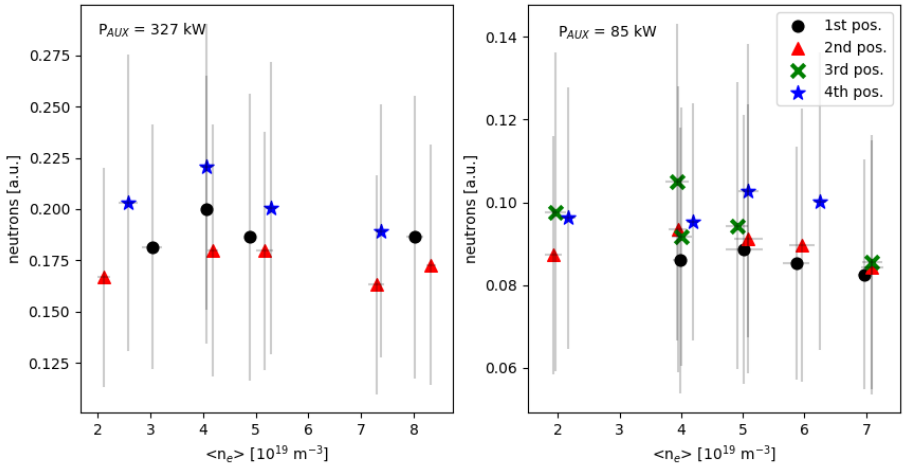

Figure 6.34: The neutron yield dependence on the plasma density for NBI2 assisted L-mode discharges, the Basic Co-current and the Shape scans in the table 5.1 for the low (85 kW) and the high (327 kW) NBI auxiliary heating power P_{AUX}.

It seems that the neutron yield barely changes with the plasma line-averaged density $\langle n_{\mathrm{e}} \rangle$ or plasma size and shape. The independence of the measured neutron yield on the plasma line-averaged density $\langle n_{\mathrm{e}} \rangle$ is caused by the indirect proportionality of the fast ions slowing down time τ_{s} on the plasma density as introduced in the equations (3.6), (3.7). The slowing down time τ_{s} density dependence leads to the simultaneous decrease of the fast ion density n_{fi} in the equation (3.8). Therefore, the expected increase of the neutron yield with the plasma density, from the equation (3.8), is balanced by the shortening of the fast ions slowing down time τ_{s} and it results to almost no density dependence of the neutron yields.

The another examined term in the equation (3.8) is the fast ion density in the plasma n_{fi}, which should be directly proportional to the NBI auxiliary heating P_{AUX}. The dependence of the neutron yields on the P_{AUX} is shown in the figure 6.35.

There is a nice linear dependence of the neutron yield on the NBI2 auxiliary heating power P_{AUX} with no significant differences for the various plasma shapes. However, it seems that there is a slight deviation of the NBI1-assisted L-modes for higher P_{AUX}. It can be a consequence of the rough estimate of the additional NBI1 scraping losses, based on the figure 6.14, which can actually vary with the NBI parameters. However, there is only one measured point and therefore it is not possible to improve the NBI1 passing fraction correction.

The other available data set is for a comparison of the co- and counter-injection, which is shown in the figure 6.36.

The neutron yield is significantly reduced in the case of the counter-injection. It is reduced by a factor ~ 1.5–2.3. There is a weak improvement of the neutron yield with the increasing plasma current I_{P}, but it varies within the error bars.

The last studied dependence of the neutron yield is on the toroidal magnetic field B_{t}, which is depicted in the figure 6.37. The discharges with a lower magnetic field tend to switch to the H-modes, but unstable ones. Therefore they are labeled

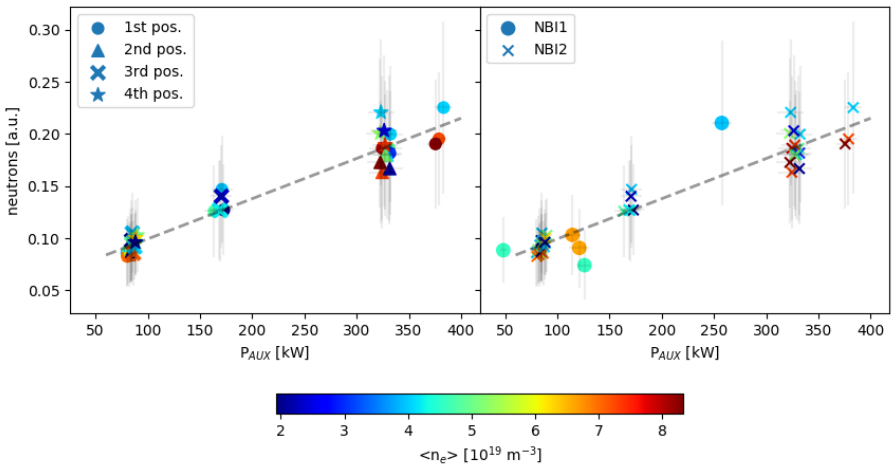

Figure 6.35: The dependence of the neutron yield on the NBI auxiliary heating power P_{AUX} for NBI2-only L-mode discharges with various plasma shapes (left), for the Basic Co-current and Shape scans in the table 5.1, and comparison of the NBI2, from the left panel, and NBI1-assisted L-mode discharges with same plasma parameters as NBI2-assisted discharges (right). The colors corresponds to the plasma line-averaged density $\langle n_{\mathrm{e}} \rangle$.

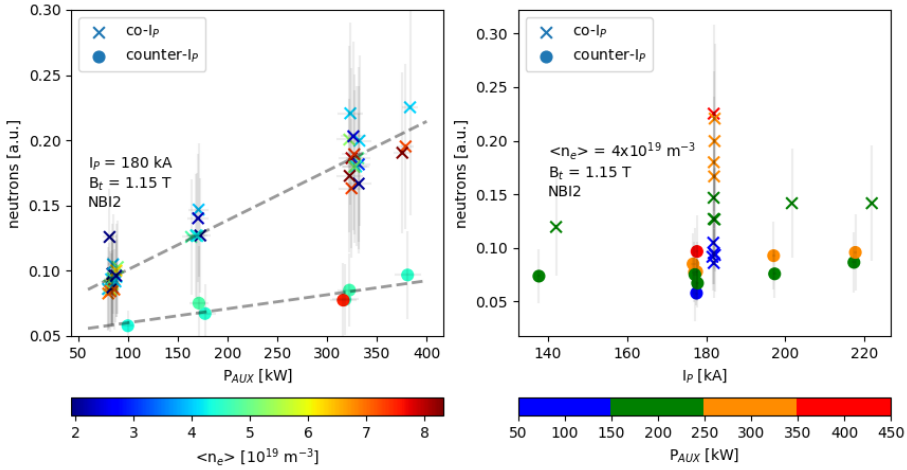

Figure 6.36: Neutron yield dependence on the NBI auxiliary heating power P_{AUX} with colors corresponding to the plasma line-averaged density $\langle n_{\mathrm{e}} \rangle$ for the Co- and Counter-current scans in the table 5.1 (left) and neutron yield dependence on the plasma current I_{P} with colors corresponding to the NBI auxiliary heating power P_{AUX} for the Current scans (Co- and Counter-current) in the table 5.1 (right).

as short H-modes in the figure.

The neutron yields increase with the toroidal magnetic field B_{t}, seen in the left panel of the figure 6.37. The possible explanation is an enhancement of the fast ions confinement, which leads to the increase of the fast ions density n_{fi} in the equation (3.8). The improvement of the energy confinement can be seen on the increase of the stored plasma energy W_{EFIT} with the toroidal magnetic field B_{t}, seen in the right panel of the figure 6.37.

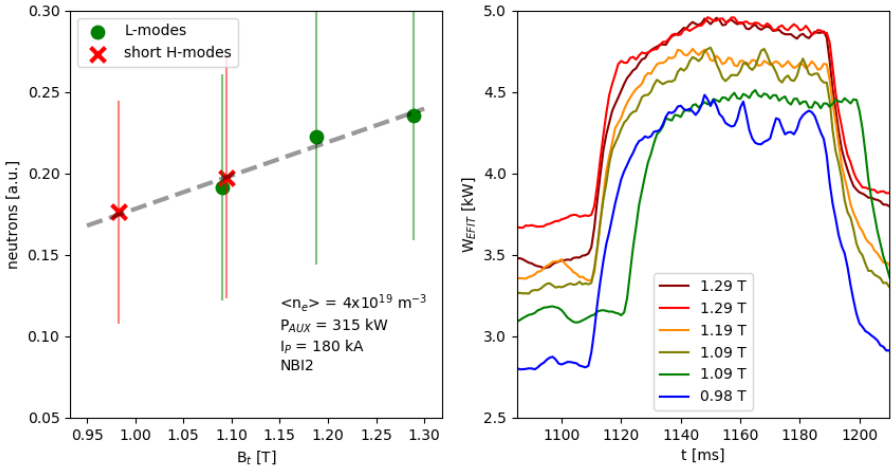

Figure 6.37: Neutron yields as function of the toroidal magnetic field (left) and the EFIT energies temporal evolution during NBI heated phases of the corresponding discharges.

To conclude, the neutron yield varies with the NBI auxiliary heating power P_{AUX} linearly in the first approximation and also with the magnetic field B_{t}. There are two phenomena with opposing impacts on the neutron production that scale with the plasma density. The neutron yield should linearly increases with the plasma density, but simultaneously the fast ions slowing down time shortens with the plasma density and therefore the fast ions density is reduced with the plasma density. These two opposite effects are balanced and it leads to the independence of the neutron yield on the plasma density. There is a strong reduction of the neutron yield for the NBI counter-injection in comparison with the NBI co-injection. But there is no dependence on the plasma current magnitude. The neutron yield enhances with the toroidal magnetic field.

Regarding the temporal evolution, it is commonly observed, that the neutron yield degrades from the initial value during the ongoing single NBI pulse , despite the plasma parameters are kept constant. This effect could be explained by the additional plasma rotation in the same direction as NBI injection, which reduces the relative collisional energy between NBI fast ions and the target plasma particles. The reduction of the relative collisional energy causes lowering of the DD fusion reaction cross section. However, a role of the plasma rotation in the neutron yield has to be confirmed by the appropriate simulations.

7. Impact of NBI heating on MHD instabilities

The possible impact of the NBI fast ions on the magneto-hydrodynamic (MHD) instabilities is introduced in the section 3.5. In this chapter, the changes of the MHD instabilities measured parameters are discussed. There are two MHD instabilities examined, which are often observed on the COMPASS tokamak: the sawtooth instability and the edge localized modes (ELMs).

7.1 Sawtooth instability

The basic mechanism of the sawtooth crashes is described in section 3.5.1. It is a core localized instability, which is characterised with a sudden hot core plasma ejection during so-called sawtooth crash. This is well visible on the plasma density and electron temperature profiles. An example of the plasma electron temperature T_e and the plasma density n_e profiles with respect to the sawtooth crash with the active NBI2 are shown in the figure 7.1.

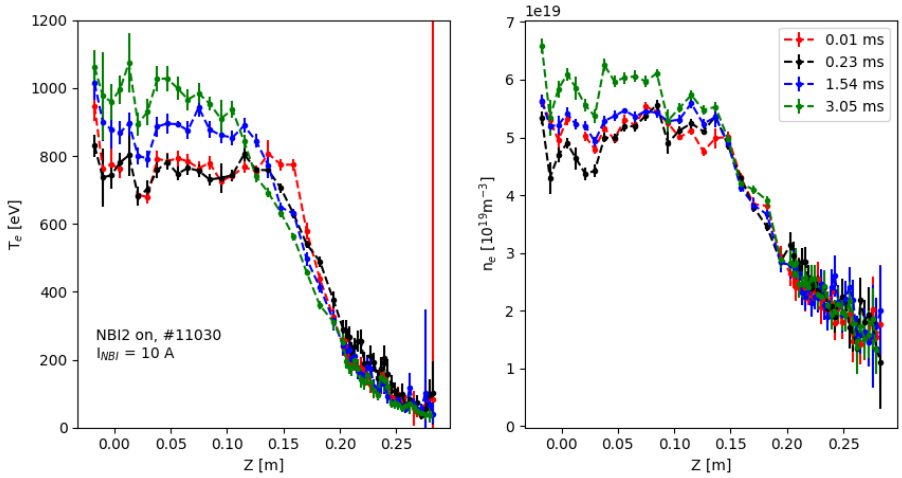

Figure 7.1: The plasma electron temperature T_e and density n_e profiles sorted in respect to the sawtooth crashes for an NBI-heated L-mode flat-top stage of a discharge.

The core plasma temperature after the sawtooth crash slowly recovers and as the crash occur, it suddenly drops. On the other hand, the temperature evolution in more outer region $Z \sim 0.15\,\mathrm{m}$ is the opposite, it slowly drops and than suddenly increases, when the sawtooth crash occur. The radius, where the temporal evolution of the electron temperature is becoming opposite, is called the *inverse radius*. The sawtooth instability is well observed with the Soft X-ray (SXR) measurements, which are sensitive to the electron temperature. SXR signals are used for the sawtooth crash detection and the diagnostic is introduced in the section 4.1. An example of the SXR signal of the channels crossing plasma core for NBI assisted discharge is shown in the figure 7.2. The sawtooth period is detected from sawtooth crash times.

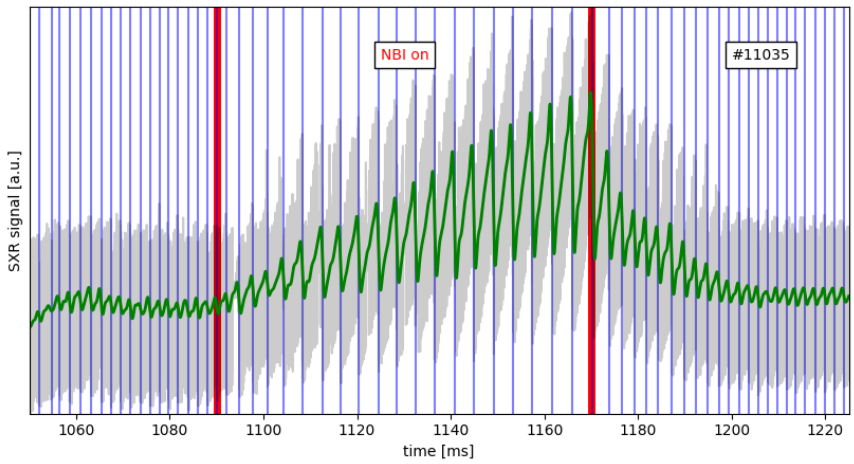

Figure 7.2: An example of the Soft X-ray signal measured on the COMPASS, which is in this case a sum of three channels crossing the plasma core. The vertical blue lines represents detected sawtooth crashes, which are well visible on the filtered data (green) of the raw signal (grey). The vertical red lines highlight NBI start and stop.

The SXR signal has the typical shape of a sawtooth wave, the slow increase and the sudden drop in the presented case of the core SXR or vice versa, if the SXR view line does not cross the plasma region inside the inverse radius. The NBI heating is usually causing an increase of the sawtooth instability amplitude and also a prolongation of the sawtooth period. However, under certain conditions, the NBI heating can also result in a destabilization of the sawtooth instability, which causes an earlier sawtooth crash. The total effect of NBI on the sawtooth period is driven by various phenomena, as it is briefly discussed in the section 3.5.1. The NBI injection orientation in respect to the plasma current and a magnitude of the additional heating power play a role. An example of the temporal evolution of the sawtooth period measured during NBI-assisted discharges, which differ only in the orientation of the plasma current I_{P} and toroidal magnetic field B_{t} are presented in the figure 7.3.

As can be seen the NBI heating is causing sawtooth period T_{saw} prolongation in case of the co-current injection, independently of the toroidal field B_{t} orientation. Contrary, the counter-injected NBI leads to the sawtooth period T_{saw} shortening and it is pretty unstable in time. This is caused by the opposite effect of the co-current and counter-current passing fast ions in the vicinity of the $q = 1$ surface on the sawtooth stability, as it is illustrated in the figure 3.4.

The sawtooth period dependence on the NBI power and injection direction was studied on various tokamaks. The results from the JET [73], EAST [74], TEXTOR[75] and MAST [76] tokamaks are shown in the figure 7.4 and measurements from the COMPASS tokamak are presented in the figure 7.5.

The sawtooth period is prolonged in the case of the co-injection and it increases with the applied NBI auxiliary heating power P_{AUX} on the COMPASS as well as on the other tokamaks. It is given by the fact, that both, the additional plasma torque from the NBI and the co-passing NBI fast ions, cause sawtooth stabilization. On the other hand, the counter-injection can shorten or prolong the sawtooth period. The effect of the counter-injection is a result of two competing

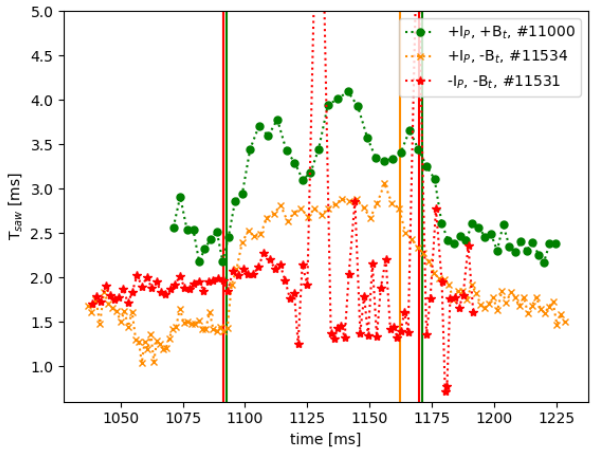

Figure 7.3: Temporal evolution of the sawtooth periods for the set of the NBI assisted discharges with an reversed orientation of the plasma current I_{P} and the magnetic field B_{T}. The vertical lines indicate the interval when the NBI was on with discharge-corresponding colors. NBI is injected in the co-direction in the case of a plus sign of the plasma current and in the counter-direction for a negative plasma current sign.

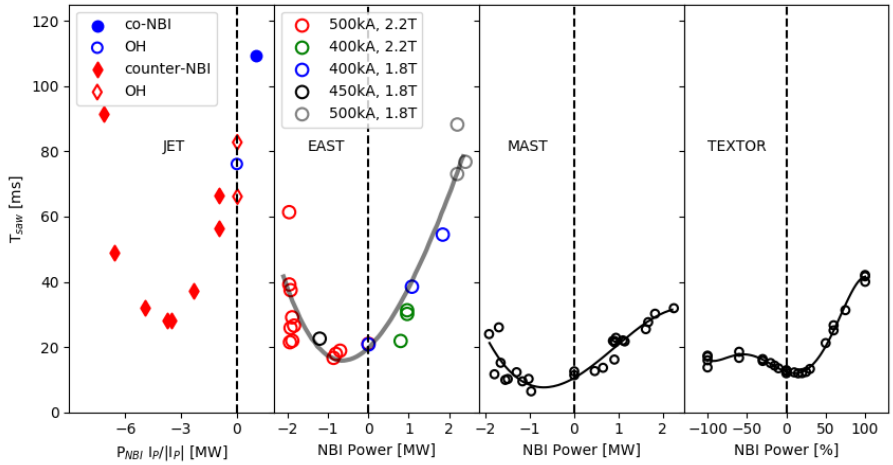

Figure 7.4: Dependencies of the sawtooth period T_{saw} on the NBI heating power for JET [73], EAST [74], TEXTOR [75] and MAST [76] tokamaks. The positive and negative values of the NBI power denote the NBI co-injection and counter-injection, respectively.

phenomena, the sawtooth stabilization by the plasma rotation and the sawtooth destabilization by the counter-passing NBI fast ions. If the intrinsic plasma rotation is in the opposite direction than the momentum transferred to the plasma from the NBI fast ions and the resulting plasma rotation is lower than the intrinsic one, the resulting effect of the plasma rotation change is a degradation of the sawtooth stability.

Usually a dependence of the sawtooth period T_{saw} on the NBI power has a U-shape with a minimum located in the counter-injection part, as seen in the case of the JET, EAST and MAST tokamaks in the figure 7.4. However it is not always like that as shows the case of the TEXTOR tokamak, which has more

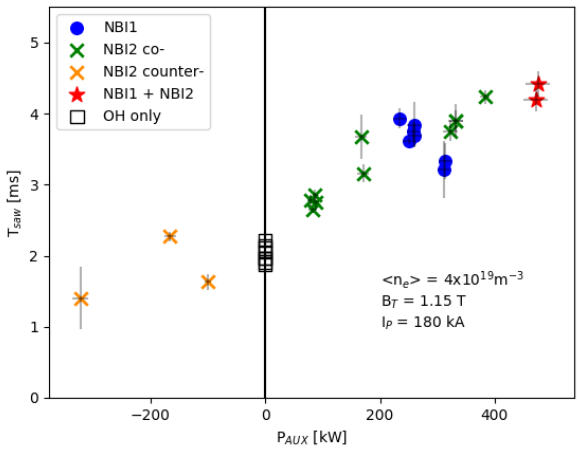

Figure 7.5: The sawtooth period in respect to the NBI auxiliary heating power P_{AUX} for a set of the similar L-mode discharges realized on the COMPASS tokamak. The positive and negative signs of the P_{AUX} represent the co-injection and counter-injection, respectively.

complicated shape of the dependence of the sawtooth period T_{saw} on the NBI for the counter-injection part.

The COMPASS measurements are derived from the flat-top part of discharges when the sawtooth period is settled down after NBI is switched on and the presented sawtooth period is an average value of the several sawteeth cycles during this flat-top NBI-heated discharge stage. As can be seen on the example of the temporal evolution of the sawtooth period in the figure 7.3, the sawtooth period is not inherently stable during NBI heating and such discharges are not considered for the sawtooth period dependence on the NBI auxiliary heating in the figure 7.5.

The sawtooth period T_{saw} dependence on the NBI auxiliary heating P_{AUX} on the COMPASS tokamak is comparable with the measurements on the other tokamaks, see figure 7.4, the sawtooth period T_{saw} increases with the NBI auxiliary heating P_{AUX} in case of the co-injection and vice versa for the counter-injection as seen in the figure 7.5. However, the expected minimum in the counter-injection part is not reached in the presented data-set.

7.2 NBI assisted H-modes and ELMs

The high confinement mode (H-mode) can be accompanied by the edge localized modes (ELMs). Their description and classification is given in the section 3.5.2. NBI heating affects ELMs by an increase of the stored plasma energy and a consequent enlargement of the power passing through the separatrix P_{sep}, which is one of the parameter playing role in the ELMs classification. On the other hand ELMs affect the fast ions distribution inside the plasma. Experimental campaigns dedicated to the NBI impact studies were done only in the L-modes and there is a lack of dedicated H-mode discharges. However, there were thousands of the NBI-assisted H-mode discharges performed on the COMPASS. The impact of the NBI heating on the pedestal, the steep gradient region of the electron temperature and

the plasma density typical for the H-modes, was studied in [77] for the COMPASS discharges.

Here two similar NBI-assisted H-modes are discussed, one with the thermal NPA measurements providing information about the ion temperature T_i and second with the NPA fast ions measurements, to explore the total energy distribution of the plasma ions during the H-modes on the COMPASS tokamak. The time traces of the discharges parameters and the NPA measured fluxes are shown in the figure 7.6 and the figure 7.7, respectively.

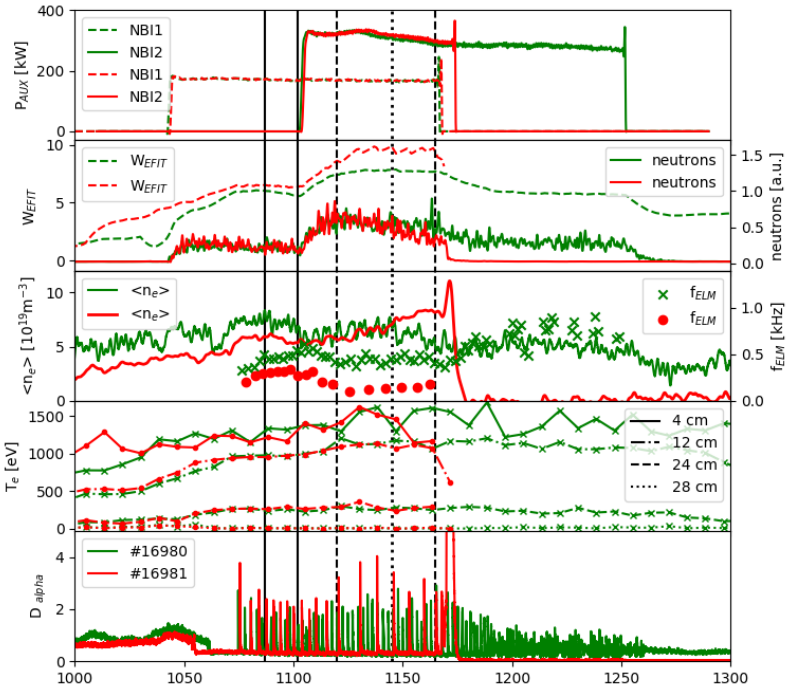

Figure 7.6: Two similar H-modes with $B_\mathrm{t} = 1.5$ T and $I_\mathrm{P} = 240$ kA. Time traces of the discharges #16980 and #16981 are depicted by a green and by a red color, respectively. The discharge #16981 ends in a disruption in time 1171 ms. They differ slightly in the plasma line-averaged density $\langle n_\mathrm{e} \rangle$ and ELMs frequency f_ELM. Due to the higher plasma line-averaged density $\langle n_\mathrm{e} \rangle$ and the lower ELMs frequency, there is the higher stored plasma energy W_EFIT in case of the discharge #16981. When the NBI1 is switched off, there are only short H-modes in case of the discharge #16980. Two time periods are analyzed, one with NBI1 only in between solid vertical lines and second with both beams NBI1+NBI2 in between dashed lines. The second analyzed time period is shorter for #16981 and it ends already, as shown by the dotted line.

Both discharges include an ELMy H-mode stage with NBI1 only and with both beams (NBI1+NBI2). H-modes are characterised by a formation of steep gradients of the electron temperature T_e and the plasma density n_e close to the separatrix, so-called pedestal, introduced in the section 3.5.2. Measured profiles of the electron temperature T_e and the plasma density n_e during both selected phases, NBI1 only and NBI1+NBI2, in respect to the ELM crash are depicted in the figure 7.8 for #16980 and in the figure 7.9 for #16981.

The pedestal height of the electron density n_e is ~ 2.5–3×10^{19} m^{-3} for #16980 and ~ 4–5×10^{19} m^{-3} for #16981 and of the electron temperature T_e is $\sim$ 200–

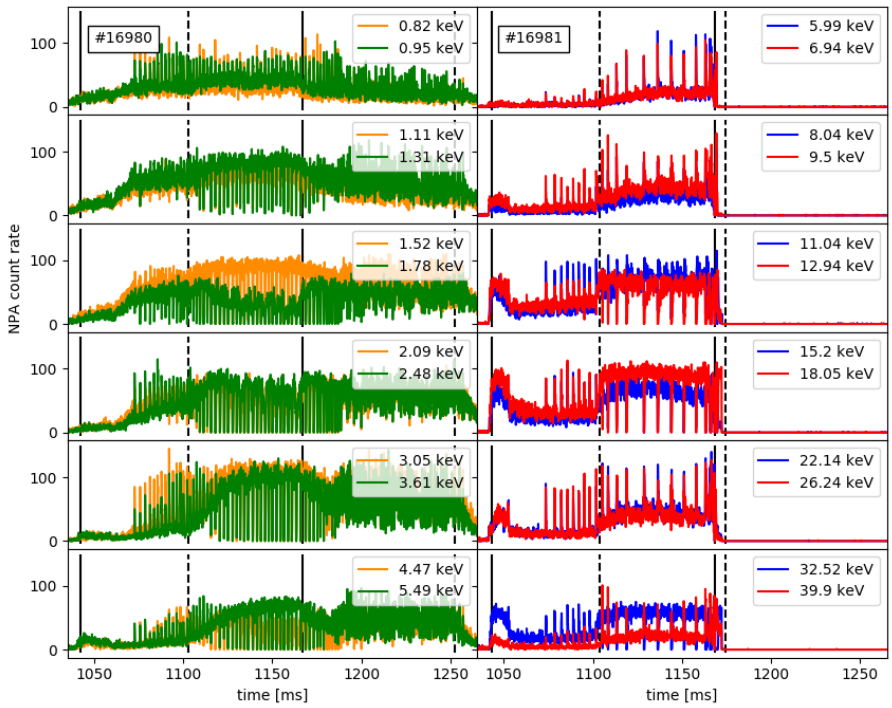

Figure 7.7: The count rates measured by NPA during the discharge #16980 (left), with the measurements of thermal energies, and the discharge #16981 (right), with the high-energy tail measurements. The solid and dashed vertical lines represent start and stop position of the NBI1 and NBI2 respectively. The sudden increases or drops are a consequence of the ELMs. A signal drop due to the ELMs is only apparent, as it is actually channeltron saturation. If the signal is too high, the channeltron recovery is longer and can lead to the permanently signal degradation, as it is in the case of #16980, channels 1.78, 2.09, 2.48 and 4.47 keV while both NBIs are ongoing.

300 eV for both discharges, which are comparable values as observed in [77]. The pedestal is at the lowest values after the ELM crash and than it recovers. Despite the fact, that NBI heating is less effective for electrons as it is concluded in the section 6.3, the core electron temperature enhances from 1.25 keV to 1.5 keV while both NBIs are switched on. On the other hand, the pedestal values do not change dramatically, which shows that the NBI heating is localized mostly in the plasma core.

Usually as the pedestal recovers, the core values should also reach their previous higher values. However, there is an opposite trend in the figure 7.8 for NBI1+NBI2 phase. The blue and black values are the latest from the ELM crash, but the core electron temperatures are significantly lower than shortly after the ELM. This is an effect of the sawtooth crash. The time traces of the sawtooth and ELM crashes and Thomson measurements with the corresponding colors to the Thomson measurements in the figures 7.8, 7.9 are in the figures 7.10 and 7.11.

Part of the NPA energy channels are becoming saturated, as seen in the figure 7.7, while one or both NBIs are ongoing. Therefore, it is impossible to study the NPA energy spectra for the ELM crash during the NBI1+NBI2 discharge stage

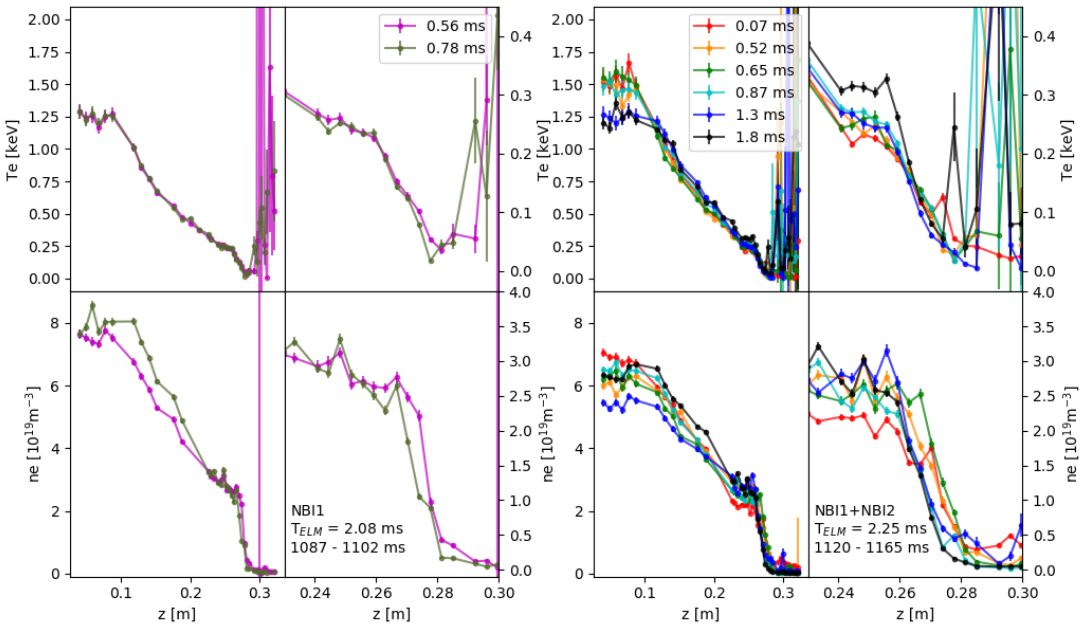

Figure 7.8: The electron temperature T_e and density n_e profiles for #16980. The NBI1 only phase is on the left (olive and magenta) and NBI1+NBI2 phase is on the right (red, orange, green, cian, blue and black). The electron temperature T_e profiles are on the top and the electron density n_e profiles are in the bottom. The left part of the graphs are full profiles and the right parts are only close-ups on the pedestal region.

and it is even complicated for the other NBI-heated discharge stages. Three of the discharge/ELM stages are presented:

- NBI1+NBI2, inter-ELM
- NBI1 only, inter-ELM
- NBI1 only, ELM crash

The NPA energy spectra are shown for the thermal energies range in the figure 7.12, which were measured during the discharge #16980, and for the high-energy tail in the figure 7.13, which were measured during the discharge #16981.

The inter-ELM ion temperature determined from the NPA measurements T_{CX} is 567 eV while only NBI1 is ongoing and increases to 850 eV when NBI2 is also switched on. If we apply the density correction from the figure 6.23, the core ion temperature T_{i0} is 800,eV for NBI1 only phase and 1147 eV when both NBIs are applied. However, this correction was derived for the parabolic shapes of the plasma profiles, which is not exactly a case of the H-mode discharges on the COMPASS, so the derived ion temperatures are only approximate.

The ELM crash causes the increase of background neutral density, as it is concluded in [50, 48, 25], which leads to the NPA signal enhancement. Simultaneously, a part of the hot particles confined inside the pedestal region are ejected out of the plasma. The ejected particles are passing through the outer more region, where the background neutral density is naturally higher, which also leads to the NPA signal increase.

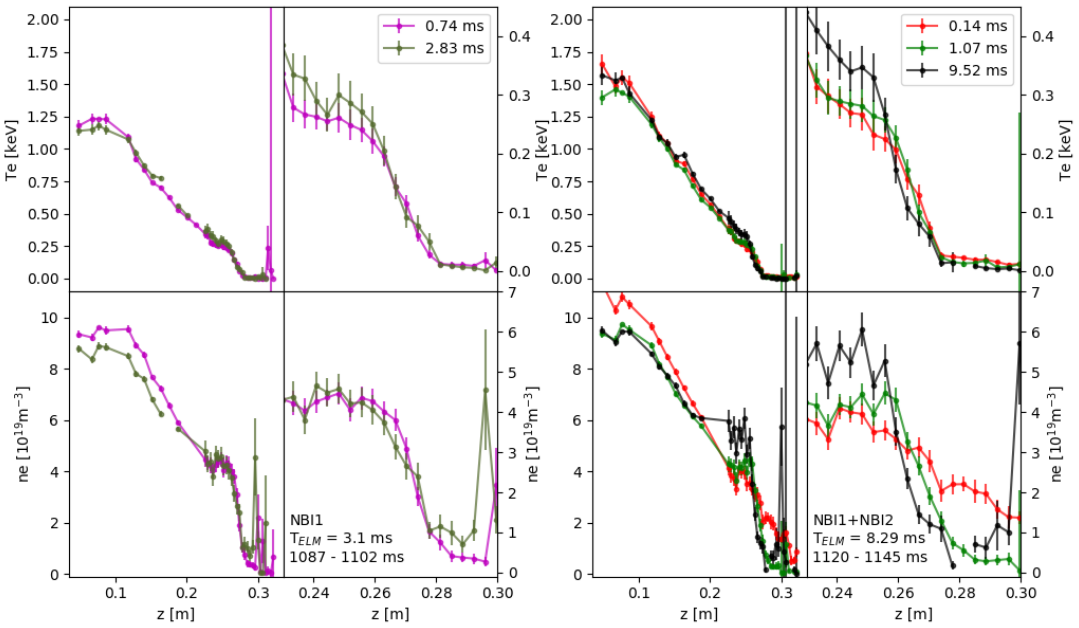

Figure 7.9: The electron temperature T_e and density n_e profiles for #16981. The NBI1 only phase is on the left (olive and magenta) and NBI1+NBI2 phase is on the right (red, green and black). The electron temperature T_e profiles are on the top, the full profiles and corresponding close-ups on the pedestal region, and the electron density n_e profiles are in the bottom, the full profiles and their close-ups on the pedestal region.

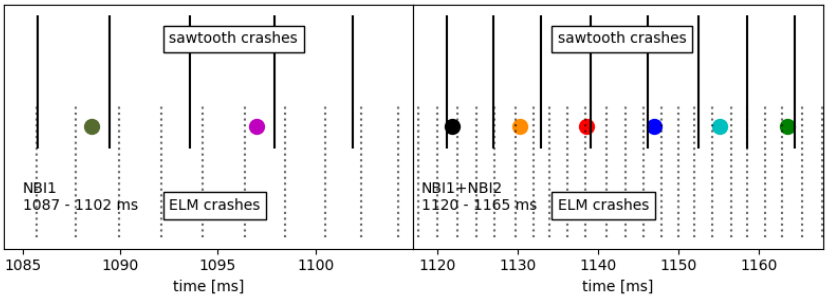

Figure 7.10: Time trace of the sawtooth crashes (dotted lines), ELM crashes (solid lines) and Thomson measurements (dots) with corresponding colors in the figures 7.8 for #16980 NBI1 only stage (left) and NBI1+NBI2 stage (right). The blue and black measurements are shortly after the sawtooth crashes and therefore the core electron temperatures are the lowest in the figure 7.8.

The high-energy tail of the neutral flux, depicted in the figure 7.13, has a *stair shape*, where each stair starts at one of the NBI characteristic energy E_b, $E_b/2$, $E_b/3$. This shape is given by the distribution function of the three mono-energetic sources of the fast ions and the partially slowed down fast ions. The energy component $E_b/10$ is not well visible, as it partially overlapping with the thermal part of the neutral fluxes and moreover it is low populated as shown in section 4.2.2. The stair shape is well visible on the inter ELM NBI1 only phase (green). When both NBIs are switched on, the high-energy tail neutral flux is $\sim 3\times$ higher, which corresponds to the ratio of the total applied NBI

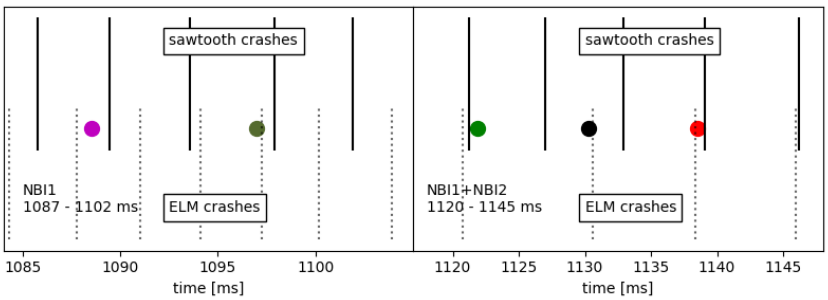

Figure 7.11: Time trace of the sawtooth crashes (dotted lines), ELM crashes (solid lines) and Thomson measurements (dots) with corresponding colors in the figure 7.9 for #16981 NBI1 only stage (left) and NBI1+NBI2 stage (right).

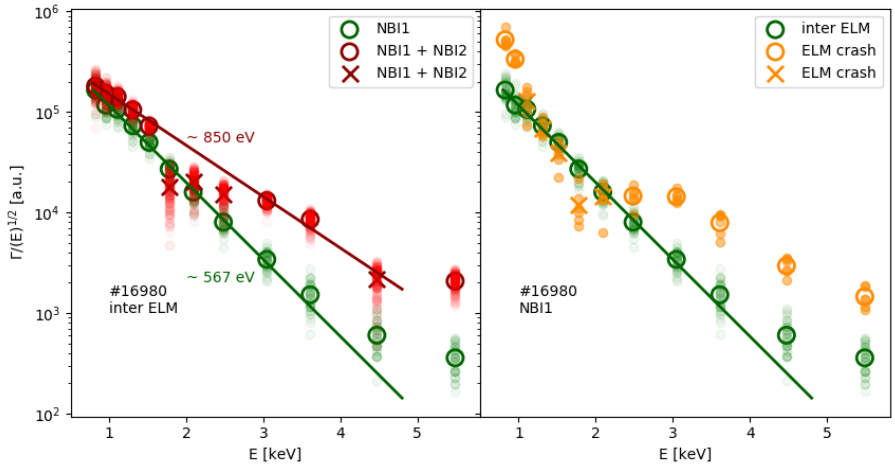

Figure 7.12: The thermal neutral flux energy spectra in the inter-ELM (left) for NBI1 only (green) and NBI1+NBI2 (red) phases and in the inter-ELM (green) and ELM crash (orange) during NBI1 phase (right) measured by NPA. The crosses represents saturated channels. The partially transparent dots are raw NPA measurements and the circles connected with the solid lines are corresponding averaged values.

auxiliary heating power in different discharge stages. The flux of the transition part between the thermal part and the high energy tail of the neutral flux energy spectra ($\sim$ 5) keV is at low level for the NBI1 only phase and increases for NBI1+NBI2 as the ion temperature is higher.

The ELMs frequencies are reduced when NBI2 is switched on and the total NBI auxiliary heating power increases in the case of the presented H-mode discharges. The change of the ELM frequency with the power through the separatrix normed by the separatrix surface $P_{\mathrm{sep\,norm}}$ serves for the ELMs classification. It should have a U-shape. While the ELM frequency drops with the normed power through separatrix $P_{\mathrm{sep\,norm}}$, the ELMs are considered to be type III. Since the ELMs are becoming more frequent with the increasing normed power through the separatrix $P_{\mathrm{sep\,norm}}$, the ELMs are considered to be type I.

The dependence of the ELMs frequency on the normed power through the separatrix $P_{\mathrm{sep\,norm}}$ for the COMPASS ohmic H-mode discharges was firstly presented in [78] and it was concluded that the normed power through the separatrix

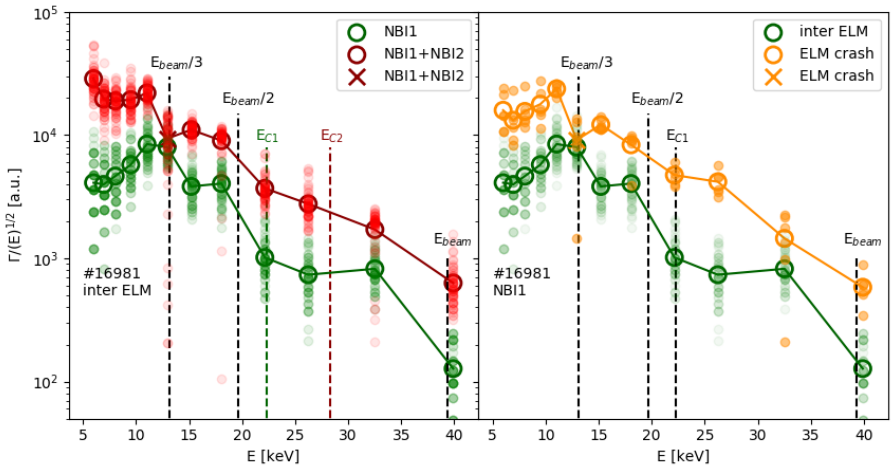

Figure 7.13: The high-energy tail neutral flux energy spectra in the inter-ELM (left) for NBI1 only (green) and NBI1+NBI2 (red) phases and in the inter-ELM (green) and ELM crash (orange) during NBI1 phase (right) measured by NPA. Black dashed lines represents NBI neutrals energies, E_{beam}, $E_{\mathrm{beam}}/2$, $E_{\mathrm{beam}}/3$. Green and red dashed lines represents critical energies, as defined in the equation (3.5), for corresponding energy spectra. The crosses represents saturated channels. The partially transparent dots are raw NPA measurements and the circles connected with the solid lines are corresponding averaged values.

~ 30 kW/m^2 is a border between the ELMs type III and I. The figure 7.14 shows originally presented data extended by the NBI-assisted and a few new ohmic H-modes data. Each data point represents one inter-ELM period in the case of the old data-set and the averaged ELM frequency in respect to the averaged normed power through the separatrix $P_{\mathrm{sep\,norm}}$ in the long-term flat-top discharge stage, in respect to the ELMs period, for the new data.

The expected U-shape of the ELM frequency dependence on the normed power through the separatrix $P_{\mathrm{sep\ norm}}$ is not clearly visible. The most visible dependence for the NBI heated discharges is on the plasma density $\langle n_{\mathrm{e}} \rangle$, which is shown in the figure 7.15.

To conclude, the neutral beam injection improves both plasma temperatures. It is possible to reach the core ion temperature above 1 keV if both NBIs are applied. The knowledge of the NBI auxiliary power allows to determine the normed power through the separatrix $P_{\mathrm{sep\,norm}}$, which is required for the ELMs type classification.

However, the dependence of the ELMs frequency f_{ELM} on the normed power through the separatrix $P_{\mathrm{sep\,norm}}$ is not clear but it nicely varies with the plasma density $\langle n_{\mathrm{e}} \rangle$. Therefore a more detailed study of the ELMs classification of the NBI heated discharges on the COMPASS is desirable.

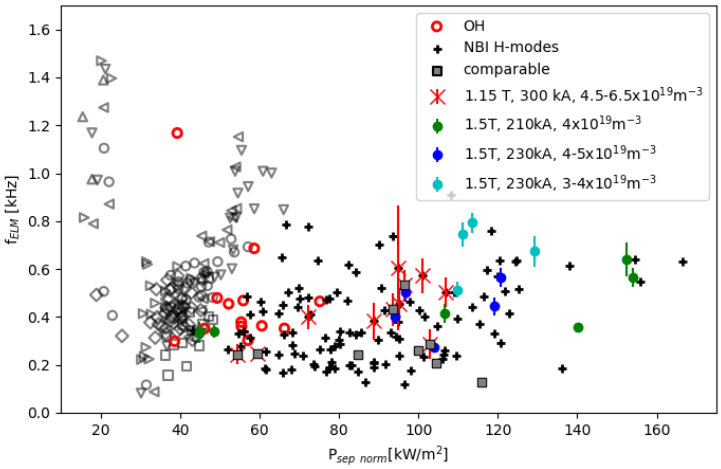

Figure 7.14: Dependence of the ELM frequency on the normed power through separatrix $P_{\mathrm{sep\,norm}}$. The original data presented in [78] are represented by a empty grey symbols. The NBI heated discharges with comparable plasma parameters are depicted by the grey squares. The black crosses are NBI-heated discharges with a wide range of the plasma parameters. A few similar sets of the discharges are highlighted by various colours and shapes.

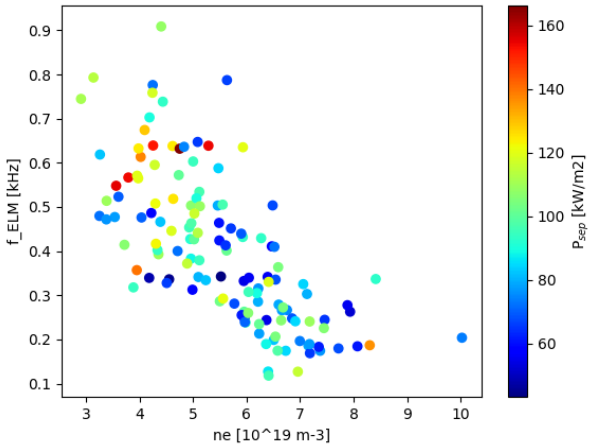

Figure 7.15: The ELM frequency in respect to the plasma density $\langle n_{\mathrm{e}} \rangle$ (horizontal axis) and normed power through the separatrix $P_{\mathrm{sep\,norm}}$ (color scale).

8. Role of the background neutrals

As it is mentioned in the description of the fast ions diagnostics in the subsection 3.6, two out of three are based on the CX-reaction with the neutrals presented in the tokamak. There are usually two kinds of the neutrals in the plasma volume: halo and background. The halo neutrals are usually well simulated as the NBI incoming flux is well defined. The background neutrals are a result of several processes as shown in the figure 4.2. The background neutrals can be derived from the UV or visible radiation [79, 80]. During my internship on the ASDEX-Upgrade, I have developed a novel method, which is based on the thermal passive measurements of the neutral particle analyzer (NPA). This newly developed method is described in the paper, which is an attachment of this thesis. Derived background neutral density can be used as the input for the fast ions synthetic diagnostics, as was shown in [25].

The second role of the background neutrals in respect to the fast ions, is a sink of the fast ions, as they undergo change-exchange collisions. A use of pre-defined background neutrals profiles in the fast-ions tracing code was shown for the first time in [81].

Conclusion

The COMPASS tokamak operates for a decade with two identical neutral beam injectors (NBI). This thesis gives an overview of the additional plasma heating effects on the plasma parameters on the COMPASS tokamak.

The most important parameter for given studies is the delivered NBI auxiliary heating power P_{AUX} into the tokamak chamber. The neutral beam injectors are connected with the COMPASS tokamak vacuum chamber by the narrow beam ducts (figure 4.4). The NBI geometry was optimized by the producer to fit the beam into the narrow duct, however, part of the delivered power is still scraped. The geometry of the extracted beam of the fast neutrals varies with the requested NBI acceleration voltage U_{beam} and NBI current I_{beam}.

The geometry of the neutral beam is given by the NBI ion optical system geometry, grids size, the grids geometrical focus and the divergence of beamlets, which are the beams extracted by a single NBI grid hole. The beamlet divergence for each separate NBI energy component is calculated from the measured broadened Doppler shifted D_α lines (figure 4.11). Simultaneously, the power and the ratios of the various extracted NBI energetic components, E_{b}, $E_{\mathrm{b}}/2$, $E_{\mathrm{b}}/3$ and $E_{\mathrm{b}}/10$, are derived (figures 4.10 and 4.12). A model is based on summing Gaussian beamlets and measured beamlet divergences where used then to predict the passing fraction through the beam duct. The passing fraction of each beam energy component and the measured beam composition are used to derive the total power entering the tokamak chamber, the auxiliary heating power P_{AUX}, dependence on the extracted NBI power(figure 4.16). NBIs on the COMPASS tokamak were optimized for the maximum delivered power, where the scraping losses are negligible and power up 400 kW is injected into the plasma by each NBI. However, if the required power is lower, the scraped power can reach up to $\sim 50\,\%$.

The passing power, the real NBI auxiliary heating power P_{AUX}, is confirmed by the power balance analysis done in the section 6.1. It was shown that the most of the delivered power into the plasma P_{NBI} carried by the NBI fast ions goes into the increase of the plasma energy W_{EFIT}. The crucial result of the power balance analysis is the fact, that the NBI1 injector delivers systematically less power into the plasma than the NBI2 injector. It is lower by 17 %. This is probably caused by additional NBI1 scraping in the beam duct, as the additional power losses of the NBI1 injector does not depend on the plasma parameters. Therefore, the auxiliary power P_{AUX} delivered by NBI2 is based on equation (4.11) and the passing fraction is lowered by an additional 17 % in the case of the NBI1.

Once the auxiliary power P_{AUX} of both NBIs is available, it is possible to determine the energy confinement times τ_{E} for NBI heated discharges on the COMPASS and compare them with the various scalings, as it is shown in the section 6.2. The energy confinement times for the L-mode discharges and H-mode discharges vary in the range 5 ms–14 ms and 10 ms–20 ms respectively.

A few systematic experimental campaigns were performed for the basic NBI impact studies on the COMPASS and are introduced in the chapter 5. The initial basic campaign considered L-mode discharges with the NBI2 co-current injection. The campaign focused on the NBI impact dependencies on the plasma density,

the plasma shape and the plasma current. Similar discharges with varied toroidal magnetic field were also realized.

The ratio of the additional NBI heating power P_{NBI} and the NBI auxiliary heating power P_{AUX} determined from the power balance seems pretty constant for all studied parameters in case of the co-injection L-modes. The core ion $T_{\mathrm{i}}(0)$ and electron temperatures $T_{\mathrm{e}}(0)$ and the plasma line-averaged density $\langle n_{\mathrm{e}} \rangle$ increases due to the NBI heating depends on the plasma line-averaged density $\langle n_{\mathrm{e}} \rangle$ and the NBI auxiliary heating power P_{AUX} (figures 6.27, 6.28). The ratio of the additional heating power absorbed by the bulk plasma electrons P_{e} and the bulk plasma ions P_{i} depends on the critical energy E_{C}, which is directly proportional to the electron temperature T_{e}. For ohmic heated flat-top stage of the discharges the observed core electron temperature $T_{\mathrm{e}}(0)$ is inversely proportional to the line-averaged plasma density $\langle n_{\mathrm{e}} \rangle$ (6.24) and consequently the ratio of the transferred NBI power into the bulk plasma ions and electrons $P_{\mathrm{i}}/P_{\mathrm{e}}$ changes. The observed core ion temperature $T_{\mathrm{i}}(0)$ increase, when NBI2 injector full power heating is applied, ranges from doubling, on the lowest densities to only a $\sim 20\,\%$ increase for the highest plasma densities. On the other hand the electron temperature remains almost unaffected by NBI at the lowest densities and it increase by $\sim 40\,\%$ at the highest densities. Plasma density increases during active NBI was observed only at the lowest densities by $\sim 20\,\%$–$40\,\%$ where the density control feedback runs out of control authority headroom.

The observed neutron yield linearly increases with the auxiliary heating power P_{AUX} (figure 6.36). It slightly increases with the higher magnetic fields B_{t} (figure 6.37). The expected dependence of the neutron yield on the plasma density, based on the equation (3.8), is balanced by shortening of the fast ion slowing down time τ_{s}, equations (3.6) and (3.7), and a consequent decrease of the fast ion density n_{fi} in the equation (3.8).

The second set of experiments was dedicated to the counter-current injection. The experimental conditions were realized by the reversing the plasma current I_{P} direction, not by the NBI relocation. Generally, the counter-injection exhibits higher NBI power losses inside the plasma, as the formed fast ions are guided to the more outer regions of the plasma, where they are more likely to be lost to wall collisions. Regarding power balance, the registered power inside the plasma P_{NBI} is lower by $\sim 40\,\%$ in comparison with the co-current injection. However, it seems there is an optimal line-averaged density $\langle n_{\mathrm{e}} \rangle = 4$–$5 \times 10^{19}$ m^{-3} (figure 6.16). At this line-averaged density $\langle n_{\mathrm{e}} \rangle$ range the delivered NBI power P_{NBI} of the counter-injected NBI into the plasma is comparable with the co-injection. Despite that, the increase of the core ion temperature $T_{\mathrm{i}}(0)$ is slightly lower than for the co-injection even for densities 4–5×10^{19} m^{-3}. The impact on the core electron temperature $T_{\mathrm{e}}(0)$ is probably lower that in case of the co-injection, but the differences are obscured by the noise (figure 6.29). The neutron yield is reduced to $\sim 60\,\%$–$40\,\%$ of the values for the co-injection case (figure 6.37).

During the design phase of the NBI for COMPASS and early phase of the operation, simulations were done using different codes (table 5.3). The best match of the heating fraction of the auxiliary heating power $P_{\mathrm{heat}}/P_{\mathrm{AUX}}$ with the fraction of the delivered NBI power P_{NBI}, derived by the power balance, carried by fast ions and the total NBI auxiliary heating power entering the tokamak chamber P_{AUX} is with the METIS simulations (figure 6.14). The FAFNER simulations

well match both, co- and counter-injection portion of the absorbed power by the plasma (figure 6.16).

The chapter 7 briefly discusses observed impacts of NBI on the sawtooth instability, high confinement modes (H-modes) and edge localized modes (ELMs). The sawtooth crashes are causing oscillations of the core electron temperature $T_e(0) \sim 200\,\mathrm{eV}$ (figure 7.1), which manifests as the additional error of the core electron temperature $T_e(0)$ changes in the section 6.3. In the studied range of the NBI power settings, the sawtooth period T_{saw} increased on the COMPASS from 2 ms up to 4 ms when NBI is injected in the co-current direction. The NBI counter-injection shortens the sawtooth period down to 1 ms (figure 7.5). However the counter-injection experiments have generally less stable sawtooth period T_{saw} and therefore only three usable data points were obtained. Usually, the U-shape dependencies of the sawtooth period T_{saw} on the NBI auxiliary heating power P_{AUX} are observed on the other tokamaks with a minimum in the counter-injection part (figure 7.4). Probably, the minimum of the counter-injection part was not reached during experiments that are presented herein.

On the contrary to the L-mode campaigns dedicated to the NBI impact studies, there were no dedicated H-mode campaigns with the same purpose. But there is still a plenty of NBI H-mode discharges in the COMPASS database. Two nearly identical consequent discharges at high magnetic field $B_t = 1.5$ T with both NBIs (figure 7.6) have been selected to illustrate the impact of the NBI heating on the H-mode discharges. The reached core electron temperature $T_e(0)$ with NBI1-only is 1.25 keV and 1.5 keV while both NBIs are operating (figures 7.8 and 7.9). The inter-ELM NPA ion temperature T_{CX} is $\sim 570\,\mathrm{eV}$ and $\sim 850\,\mathrm{eV}$ while NBI1 and both NBIs are operating respectively. When the correction to the core ion temperature $T_i(0)$ is applied, the inter-ELM NPA ion temperatures corresponds to the core ion temperatures $T_{i0} \sim 850\,\mathrm{eV}$ and $\sim 1150\,\mathrm{eV}$. However, these numbers are only an approximate value as some of the NPA channels were saturated during these measurements and the correction factor was derived for the parabolic profiles of the temperatures and density.

The derived formulas for the auxiliary power P_{AUX} for both NBIs allowed for the first time to determine the normed power through the separatrix $P_{sep\,norm}$ for NBI heated discharges. Therefore the dependence of the ELM frequency f_{ELM} on the normed power through the separatrix $P_{sep\,norm}$ is presented, which serves for the ELM type classification (figure 7.14). Unfortunately, this dependence is not clear and does not have a typical U-shape, which is expected. The most significant dependence of the ELMs frequency f_{ELM} of the set of standard plasma parameters is on the plasma line-averaged density $\langle n_e \rangle$ (figure 7.15). The calculated normalized power through the separatrix $P_{sep\,norm}$ including NBI auxiliary heating will allow further studies of the ELMs classification on the COMPASS for the NBI heated discharges.

The last chapter comments on an article considering the background neutral density determination on the ASDEX Upgrade tokamak exploiting NPA data, which is a newly developed unique method. It provides information about the background neutrals profile, even deeper inside the plasma. This work was done during the authors internship on the ASDEX Upgrade tokamak. The background neutral density causes charge-exchange losses of the fast ions and simultaneously the charge-exchange collisions are exploited by the fast ion diagnostics. These

reasons were a motivation to start with the background neutral density studies. Besides the introduction of the method and its validation, the temporal evolution of the background neutral density during the ELM cycle is discussed. The ELM crash causes an increase of the background neutral density, even deeper inside the plasma. That generally leads to the enhancement of the NPA signals during the ELM crash and simultaneously charge-exchange fast ions losses.

Bibliography

[1] International Energy Agency. *Key World Energy Statistics*. 2017.

[2] J.P. Freidberg. *Plasma Physics and Fusion Energy*. Cambridge University Press, 2008.

[3] J. Wesson and D.J. Campbell. *Tokamaks*. International Series of Monogr. OUP Oxford, 2011.

[4] International Atomic Energy Agency. *Fusion Physics*. Publication. International Atomic Energy Agency, Vienna, 2012.

[5] K. Miyamoto. *Plasma physics and controlled nuclear fusion*, volume 38. Springer Science & Business Media, 2005.

[6] A.G. Peeters. The bootstrap current and its consequences. *Plasma Physics and Controlled Fusion*, 42(12B):B231, 2000.

[7] P. Helander and D.J. Sigmar. *Collisional transport in magnetized plasmas*, volume 4. Cambridge University Press, 2005.

[8] J. Datlov, K. Jakubka, V. Kopecky, et al. Rf heating of plasma at $\omega = \omega_{LH}$ in tokamak tw-1-mh. In *9th ECCFPP*, page 539, 1979.

[9] W. Helou, M. Goniche, J. Hillairet, et al. Radio-frequency design of a lower hybrid slotted waveguide antenna. *Fusion Engineering and Design*, 123:223–227, 2017. Proceedings of the 29th Symposium on Fusion Technology (SOFT-29) Prague, Czech Republic, September 5-9, 2016.

[10] Heating ITER Physics Expert Group on Energetic Particles, Current Drive, and ITER Physics Basis Editors. Chapter 6: Plasma auxiliary heating and current drive. *Nuclear Fusion*, 39(12):2495, 1999.

[11] A.A. Ivanov, P.P. Deichuli, A. Kreter, et al. Characterization of ion species mix of the textor diagnostic hydrogen beam injector with a rf and arc-discharge plasma box. *Review of scientific instruments*, 75(5):1822–1825, 2004.

[12] K. Mitosinkova, J. Stöckel, J. Varju, et al. Energy composition of high-energy neutral beams on the compass tokamak. *Nukleonika*, 61(4):419–423, 2016.

[13] M.G. von Hellermann, E. Delabie, R.J.E. Jaspers, et al. Active beam spectroscopy. In *AIP Conference Proceedings*, volume 988, pages 165–176. AIP, 2008.

[14] B. Geiger, M. Garcia-Munoz, W.W. Heidbrink, et al. Fast-ion d-alpha measurements at asdex upgrade. *Plasma Physics and Controlled Fusion*, 53(6):065010, 2011.

[15] S.L. Davis, D. Mueller, and C.J. Keane. Mass resolving charge-exchange system on the poloidal divertor experiment. *Review of Scientific Instruments*, 54(3):315–327, 1983.

[16] K. Huebner, R. Bätzner, H. Hinsch, et al. Plasma rotation effects on neutron production and measurement on asdex. In *Europhysics Conference Abstracts*, volume 13, 1989.

[17] M. Bitter, V. Arunasalam, M.G. Bell, et al. High power neutral beam heating experiments on tftr with balanced and unbalanced momemtum input. *Plasma Physics and Controlled Fusion*, 29(10A):1235, 1987.

[18] H. Zohm. *Magnetohydrodynamic stability of tokamaks*. John Wiley & Sons, 2014.

[19] I.P. Chapman. Controlling sawtooth oscillations in tokamak plasmas. *Plasma Physics and Controlled Fusion*, 53(1):013001, 2010.

[20] I.T. Chapman, S.D. Pinches, J.P. Graves, et al. The physics of sawtooth stabilization. *Plasma Physics and Controlled Fusion*, 49(12B):B385, 2007.

[21] I.T. Chapman, I. Jenkins, R.V. Budny, et al. Sawtooth control using off-axis nbi. *Plasma Physics and Controlled Fusion*, 50(4):045006, 2008.

[22] I.T. Chapman, S.D. Pinches, J.P. Graves, et al. The effect of energetic particles on sawteeth. In *3rd IAEA Technical Committee Meeting on Theory of Plasma Instabilities, University of York, UK*, 2007.

[23] A.W. Leonard. Edge-localized-modes in tokamaks. *Physics of Plasmas*, 21(9):090501, 2014.

[24] H. Zohm. Edge localized modes (elms). *Plasma Physics and Controlled Fusion*, 38(2):105, 1996.

[25] A.J. van Vuuren, B. Geiger, P.A. Schneider, et al. Experimental study of elm induced fast-ion transport using passive fida spectroscopy at the asdex upgrade tokamak. *Nuclear Fusion*, 61(4):046001, 2021.

[26] J. Galdon-Quiroga, M. Garcia-Munoz, K.G. McClements, et al. Observation of accelerated beam ion population during edge localized modes in the asdex upgrade tokamak. *Nuclear Fusion*, 59(6):066016, 2019.

[27] M. Garcia-Munoz, H.U. Fahrbach, H. Zohm, et al. Scintillator based detector for fast-ion losses induced by magnetohydrodynamic instabilities in the asdex upgrade tokamak. *Review of Scientific Instruments*, 80(5):053503, 2009.

[28] R. Pánek et al. Reinstallation of the compass-d tokamak in ipp ascr. *Czechoslovak Journal of Physics*, 56(2):B125–B137, 2006.

[29] Comapss tokamak web page. http://www.ipp.cas.cz/. Accesed: 2019.

[30] V. Weinzettl et al. Progress in diagnostics of the compass tokamak. *Journal of Instrumentation*, 12:C12015, 2017.

[31] J. Havlicek, O. Kudláček, F. Janky, et al. Status of magnetic diagnostics on compass. *WDS'10 Proceedings of Contributed Papers: Part II–Physics of Plasmas and Ionized Media*, pages 12–17, 2010.

[32] J. Havlíček. Study of equilibrium magnetic configuration in tokamak type devices. 2015.

[33] N.N. Gorelenkov and L.E. Zakharov. Plasma equilibrium with fast ion orbit width, pressure anisotropy, and toroidal flow effects. *Nuclear Fusion*, 58(8):082031, jul 2018.

[34] M. Imrisek, V. Weinzettl, J. Mlynar, et al. Use of soft x-ray diagnostic on the compass tokamak for investigations of sawteeth crash neighborhood and of plasma position using fast inversion methods. *Review of Scientific Instruments*, 85(11):11E433, 2014.

[35] P. Bohm, M. Aftanas, P. Bilkova, et al. Edge thomson scattering diagnostic on compass tokamak: Installation, calibration, operation, improvements. *Review of Scientific Instruments*, 85(11):11E431, 2014.

[36] P. Bilkova, P. Bohm, M. Aftanas, et al. High resolution thomson scattering on the compass tokamak—extending edge plasma view and increasing repetition rate. *Journal of Instrumentation*, 13(01):C01024, 2018.

[37] M. Varavin, J. Zajac, F. Zacek, et al. New design of microwave interferometer for tokamak compass. *Telecommunications and Radio Engineering*, 73(10), 2014.

[38] J. Zajac, J. Preinhaelter, J. Urban, et al. Electron cyclotron-electron bernstein wave emission diagnostics for the compass tokamak. *Review of Scientific Instruments*, 81(10):10D911, 2010.

[39] J. Preinhaelter, J. Zajac, J. Urban, et al. New results from ebw emission experiment on compass. *39th EPS Conference on Plasma Physics*, 2012.

[40] O. Bogár, K. Mitosinkova, J. Urban, et al. Ebw emission measurement during nbi heated discharge in the compass tokamak. In *Poster presented at 43th EPS Conference on Plasma Physics 2016*, 2016.

[41] J. Mlynar, O. Ficker, E. Macusova, et al. Runaway electron experiments at compass in support of the eurofusion iter physics research. *Plasma Physics and Controlled Fusion*, 61(1):014010, 2018.

[42] Npa ioffe web page. http://www.ioffe.ru/ACPL/npd/npa01.htm. Accesed: 2021.

[43] K. Mitosinkova, A. Melnik, M. Tomes, et al. First results from the neutral particle analyzer on the compass tokamak. In *1st EPS conference on Plasma Diagnostics*, volume 240, page 074. SISSA Medialab, 2016.

[44] Ioffe Physical-Technical Institute of the Russian Academy of Sciences. *Multichannel Neutral Particle Analyzer ACORD-24, Instructions and Operating Manual*. Budker Institute of Nuclear Physics.

[45] Yu.N. Dnestrovskij, S.E. Lysenko, and A.I. Kislyakov. Recombination-induced neutral particle flux in tokamaks. *Nuclear Fusion*, 19(3):293, 1979.

[46] I.U.S. Gordeev, A.N. Zinovev, and M.P. Petrov. Recombination of hydrogen in a quasi-stationary thermonuclear plasma. *JETP Letters*, 25:204–207, 1977.

[47] J. Cerovsky, O. Ficker, J. Mlynar, et al. First pellet injection experiment in support of runawayelectron investigation at the compass tokamak. In *Poster presented at 47th EPS Conference on Plasma Physics 2021*, 2021.

[48] K. Bogar, Benedikt B. Geiger, P.A. Schneider, et al. Direct determination of midplane background neutral density profiles from neutral particle analyzers. *Nuclear Fusion*, 61(3):036001, 2021.

[49] K. Mitosinkova, M. Tomes, J. Stockel, et al. Double code simulations of emissivities of fast neutrals for different plasma observation view-lines of neutral particle analyzers on the compass tokamak. In *Journal of Physics: Conference Series*, volume 992, page 012009. IOP Publishing, 2018.

[50] K. Mitosinkova, B. Geiger, P.A. Schneider, et al. Direct determination of background neutral density profiles from neutral particle analyzers. In *45th EPS Conference on Plasma Physics*. European Physical Society, 2018.

[51] V.I. Afanasyev, A. Gondhalekar, and A.I. Kislyakov. *On the possibility of determining the radial profile of hydrogen isotope composition of jet plasmas, and of deducing radial transport of the isotope ions*. JET Joint Undertaking, 2000.

[52] W.W. Heidbrink, D. Liu, Y. Luo, et al. A code that simulates fast-ion d α and neutral particle measurements. *Communications in Computational Physics*, 10(3):716–741, 2011.

[53] P. Deichuli, V. Davydenko, V. Belov, et al. Commissioning of heating neutral beams for compass-d tokamak. *Review of Scientific Instruments*, 83(2):02B114, 2012.

[54] Budker Institute of Nuclear Physics. *Neutral Beam Injector NBI-CMP for the COMPASS-D Tokamak*. Budker Institute of Nuclear Physics.

[55] K. Mitosinkova. Dodatečný ohřev plazmatu v tokamaku compass pomocí vstřiku svazku neutrálních atomů [online], 2012 [cit. 2021-05-31].

[56] K. Mitosinkova. Dodatečný ohřev tokamakového plazmatu vstřikem výkonového svazku atomů vodíku/deuteria [online]. Diplomová práce, Masarykova univerzita, Přírodovědecká fakulta, Brno, 2014 [cit. 2021-05-31].

[57] R. Uhlemann, R.S. Hemsworth, G. Wang, et al. Hydrogen and deuterium ion species mix and injected neutral beam power fractions of the textor–pinis for 20–60 kv determined by doppler shift spectroscopy. *Review of scientific instruments*, 64(4):974–982, 1993.

[58] J. Kim and H.H. Haselton. Analysis of particle species evolution in neutral-beam injection lines. *Journal of Applied Physics*, 50(6):3802–3807, 1979.

[59] I.D. Williams, J. Geddes, and H.B. Gilbody. Balmer α emission in collisions of h, h+, h2+ and h3+ with h2. *Journal of Physics B: Atomic and Molecular Physics*, 15(9):1377, 1982.

[60] I.D. Williams, J. Geddes, and H.B. Gilbody. Balmer α emission in h2-h2 collisions. *Journal of Physics B: Atomic and Molecular Physics*, 16(24):L765, 1983.

[61] W. Ott and F.P. Penningsfeld. Spectroscopic determination of species and divergence of hydrogen beams in the w7as neutral beam injectors. 1993.

[62] J. Urban, V. Fuchs, R. Pánek, et al. Nbi system for reinstalled compass-d tokamak. *Czechoslovak Journal of Physics*, 56(2):B176–B181, 2006.

[63] A. Seman. Compass tokamak experiments supportby simulations. Diploma thesis, Czech technical university in Prague, Faculty of Nuclear Sciences and Physical Engineering, Prague, 2017.

[64] J. Havlíček. Study of equilibrium magnetic configuration in tokamak type devices. 2015.

[65] Butterworth filter. https://en.wikipedia.org/wiki/Butterworth_filter. Accesed: 2021.

[66] W.H. Press, S.A. Teukolsky, W.T. Vetterling, et al. *Numerical Recipes in C*. Cambridge University Press, 1992.

[67] K. Mitosinkova, J. Havlicek, J. Varju, et al. Global energy confinement time of nbi-heated plasma on the compass tokamak. In *44th EPS*, page P4.149, 2017.

[68] J.E. Rice, J. Citrin, N.M. Cao, et al. Understanding loc/soc phenomenology in tokamaks. *Nuclear Fusion*, 60(10):105001, 2020.

[69] P.G. Carolan, D.J. Fielding, S. Gerasimov, et al. Characteristics of ohmic h-modes in compass-d. *Plasma physics and controlled fusion*, 36(7A):A111, 1994.

[70] Ch. Schlatter, B.P. Duval, and A.N. Karpushov. Reconstruction of ion temperature profiles from single chord NPA measurements on the TCV tokamak. *Plasma Physics and Controlled Fusion*, 48(12):1765–1785, nov 2006.

[71] G. Sadler W.G.F. Core, P. van Belle. Beam-plasma fusion yield in rotating tokamak plasmaa. *Controlled Fusion and Plasma Physics*, 11D:49–52, 1987.

[72] A.N. Karpushov, R. Chavan, S. Coda, et al. Neutral beam heating on the tcv tokamak. *Fusion Engineering and Design*, 123:468–472, 2017.

[73] M.F.F. Nave, H.R. Koslowski, S. Coda, et al. Exploring a small sawtooth regime in joint european torus plasmas with counterinjected neutral beams. *Physics of plasmas*, 13(1):014503, 2006.

[74] Y. Chao, L. Xu, L. Hu, et al. Sawtooth activities in east neutral beam injection plasma. *AIP Advances*, 9(1):015226, 2019.

[75] I.T. Chapman, S.D. Pinches, H.R. Koslowski, et al. Sawtooth stability in neutral beam heated plasmas in textor. *Nuclear Fusion*, 48(3):035004, 2008.

[76] I.T. Chapman, T.C. Hender, S. Saarelma, et al. The effect of toroidal plasma rotation on sawteeth in mast. *Nuclear fusion*, 46(12):1009, 2006.

[77] M. Komm, P. Bílková, et al. Contribution to the multi-machine pedestal scaling from the COMPASS tokamak. *Nuclear Fusion*, 57(5):056041, apr 2017.

[78] R. Pánek et al. Status of the COMPASS tokamak and characterization of the first h-mode. *Plasma Physics and Controlled Fusion*, 58(1):014015, oct 2015.

[79] R.L. Boivin, J.W. Hughes, B. LaBombard, et al. High resolution measurements of neutral density and ionization rate in the alcator c-mod tokamak. *Review of Scientific Instruments*, 72(1):961–964, 2001.

[80] D.P. Stotler, F. Scotti, R.E. Bell, et al. Reconstruction of nstx midplane neutral density profiles from visible imaging data. *Journal of Nuclear Materials*, 463:897–901, 2015. PLASMA-SURFACE INTERACTIONS 21.

[81] F. Jaulmes, G. Zadvitskiy, K. Bogar, et al. Modelling of charge-exchange induced NBI losses in the COMPASS upgrade tokamak. *Nuclear Fusion*, 61(4):046012, mar 2021.

List of Figures

List of Tables

List of Abbreviations

ECCD	electron cyclotron current drive
ECE	electron cyclotron emission
ECRH	electron cyclotron resonance heating
EFIT	equilibrium fitting
H-mode/L-mode	high/low confinement mode
ICRH	ion cyclotron resonance heating
LHCD	lower hybrid current drive
LOC/SOC	linear/saturated ohmic confinement
MHD	magneto-hydrodynamic
NBI	neutral beam injector
NBI1/NBI2	neutral beam injector 1/2
NPA	neutral particle analyzer
RF	radio-frequency
SXR	soft X-ray
TS	Thomson scattering

List of publications

Impacted publications

- **K. Mitosinkova**, J. Stöckel, J. Varju, et al. Energy composition of high-energy neutral beams on the compass tokamak. *Nukleonika*, 61(4):419–423, 2016.
  DOI: 10.1515/nuka-2016-0069

- **K. Bogar**, Benedikt B. Geiger, P.A. Schneider, et al. Direct determination of midplane background neutral density profiles from neutral particle analyzers. *Nuclear Fusion*, 61(3):036001, 2021.
  DOI: 10.1088/1741-4326/abcd75

- R. Pánek, J. Adámek, M. Aftanas, P. Bílková, P. Böhm, F. Brochard, P. Cahyna, J. Cavalier, R. Dejarnac, M. Dimitrova, O. Grover, J. Harrison, P. Háček, J. Havlíček, A. Havránek, J. Horáček, M. Hron, M. Imríšek, F. Janky, A. Kirk, M. Komm, K. Kovařík, J. Krbec, L. Kripner, T. Markovič, **K. Mitošinková**, J. Mlynář, D. Naydenkova, M. Peterka, J. Seidl, J. Stöckel, E. Štefániková, M. Tomeš, J. Urban, P. Vondráček, M. Varavin, J. Varju, V. Weinzettl, J. Zajac and the COMPASS team, Status of the COMPASS tokamak and characterization of the first H-mode. *Plasma Phys. Control. Fusion*, 58:014015, 2016.
  DOI:10.1088/0741-3335/58/1/014015

- M. Komm, P. Bilkova, M. Aftanas, M. Berta, P. Böhm, O. Bogar, L. Frassinetti, O. Grover, P. Hacekek, J. Havlicek, M. Hron, M. Imrisek, J. Krbec, **K. Mitosinkova** et al., Contribution to the multi-machine pedestal scaling from the COMPASS tokamak. *Nuclear Fusion*, 51(5):056041, 2017.
  DOI: 10.1088/1741-4326/aa6659

- J. Seidl, J. Krbec, M. Hron, J. Adamek, C. Hidalgo, T. Markovic, A.V. Melnikov, J. Stockel, V. Weinzettl, M. Aftanas, P. Bilkova, O. Bogar, P. Bohm, L.G. Eliseev, P. Hacek, J. Havlicek, J. Horacek, M. Imrisek, K. Kovarik, **K. Mitosinkova**, et al. Electromagnetic characteristics of geodesic acoustic mode in the COMPASS tokamak. *Nuclear Fusion*, 57(12):126048, 2017.
  DOI: 10.1088/1741-4326/aa897e

- F. Camilo de Souza, A.G. Elfimov, R.M.O. Galvão, J. Krbec, J. Seidl, J. Stöckel, M. Hron, J. Havlicek, **K. Mitosinkova**. Geodesic mode instability driven by electron and ion fluxes during neutral beam injection in tokamaks. *Physics Letters A*, 381(36):3066-3070, 2017.
  DOI: 10.1016/j.physleta.2017.07.033

- J. Adamek, J. Seidl, J. Horacek, M. Komm, T. Eich, R. Panek, J. Cavalier, A. Devitre, M. Peterka, P. Vondracek, J. Stöckel, D. Sestak, O. Grover, P. Bilkova, P. Böhm, J. Varju, A. Havranek, V. Weinzettl, J. Lovell, M. Dimitrova, **K. Mitosinkova**, et al. Electron temperature and heat load

measurements in the COMPASS divertor using the new system of probes. *Nuclear Fusion*, 57(11):116017, 2017.
DOI: 10.1088/1741-4326/aa7e09

- V. Weinzettl, J. Adamek, M. Berta, P. Bilkova, O. Bogar, P. Bohm, J. Cavalier, R. Dejarnac, M. Dimitrova, O. Ficker, D. Fridrich, O. Grover, P. Hacek, J. Havlicek, A. Havranek, J. Horacek, M. Hron, M. Imrisek, M. Komm, K. Kovarik, J. Krbec, T. Markovic, E. Matveeva, **K. Mitosinkova**, J. Mlynar, et al. Progress in diagnostics of the COMPASS tokamak. *Journal of Instrumentation*, 12(12):C12015–C12015, 2017.
DOI: 10.1088/1748-0221/12/12/c12015

- A. Jansen van Vuuren, B. Geiger, P.A. Schneider, **K. Bogar**, P.Zs. Poloskei, et al. Modelling of charge-exchange induced NBI losses in the COMPASS upgrade tokamak. *Nuclear Fusion*, 61(4):046001, 2021.
DOI: 10.1088/1741-4326/abd41b

- F. Jaulmes, G. Zadvitskiy, **K. Bogar**, et al. Modelling of charge-exchange induced NBI losses in the COMPASS upgrade tokamak. *Nuclear Fusion*, 61(4):046012, 2021.
DOI: 10.1088/1741-4326/abd41b

- P. Vondracek, R. Panek, M. Hron, J. Havlicek, V. Weinzettl, T. Todd, D. Tskhakaya, G. Cunningham, P. Hacek, J. Hromadka, P. Junek, J. Krbec, N. Patel, D. Sestak, J. Varju, J. Adamek, M. Balazsova, V. Balner, P. Barton, J. Bielecki, P. Bilkova, J. Błocki, D. Bocian, **K. Bogar**, O. Bogar, et al. Preliminary design of the COMPASS upgrade tokamak. *Fusion Engineering and Design*, 169:112490, 2021.
DOI: 10.1016/j.fusengdes.2021.112490

- M. Tomes, M. Carr, A. Meakins, M. Imrisek, F. Jaulmes, V. Balner, **K. Bogar**, et al. Feasibility study and CXRS synthetic diagnostic model for COMPASS upgrade based on Cherab and Raysect framework. *Fusion Engineering and Design*, 170:112498, 2021.
DOI: 10.1016/j.fusengdes.2021.112498

Conference publications

- **K. Mitosinkova**, A. Melnik, M. Tomes, et al. First results from the neutral particle analyzer on the compass tokamak. In *1st EPS conference on Plasma Diagnostics*, volume 240, page 074. SISSA Medialab, 2016.
  DOI: 10.22323/1.240.0074

- **K. Mitosinkova**, J. Havlicek, J. Varju, et al. Global energy confinement time of NBI-heated plasma on the COMPASS tokamak. *44thEPS Conference on Plasma Physics*. European Physical Society, 2017.
  URL: http://ocs.ciemat.es/EPS2017PAP/pdf/P4.149.pdf

- **K. Mitosinkova**, M. Tomes, J. Stockel, et al. Double code simulations of emissivities of fast neutrals for different plasma observation view-lines of neutral particle analyzers on the compass tokamak. *Journal of Physics: Conference Series*, volume 992, page 012009. IOP Publishing, 2018.
  DOI: 10.1088/1742-6596/992/1/012009

- **K. Mitosinkova**, B. Geiger, P.A. Schneider, et al. Direct determination of background neutral density profiles from neutral particle analyzers. *45thEPS Conference on Plasma Physics*. European Physical Society, 2018.
  URL: http://ocs.ciemat.es/EPS2018PAP/pdf/P4.1100.pdf

Attachments

Article: **Direct determination of midplane background neutral density profiles from neutral particle analyzers**